Oxidation behavior of Ferritic Alloys as Interconnect of Solid Oxide Fuel Cell (SOFC)

by

Yu Zhao

A dissertation submitted to the Graduate Faculty of
Auburn University
in partial fulfillment of the
requirements for the Degree of
Doctor of Philosophy

Auburn, Alabama
May 6, 2012

Key words: ferritic alloy, SOFC interconnect, high temperature oxidation, dual atmosphere, grain size, $(Mn,Co)_3O_4$ coating

Approved by

Jeffrey W. Fergus, Chair, Professor of Materials engineering
Zhongyang Cheng, Professor of Materials engineering
Dong-Joo Kim, Associate Professor of Materials engineering
Curtis Shannon, Professor of Chemistry and biochemistry

Abstract

In planar solid oxide fuel cell SOFCs, interconnects separate adjacent single cells, and Cr-containing ferritic stainless steel alloys can be used for interconnects. Oxidation resistance under the SOFC high temperature environment is one of the critical issues for the application of ferritic alloys as the interconnect materials. In SOFCs, there is a H_2 concentration difference between the two sides of the interconnect materials, so hydrogen may diffuse through the alloy and aggravate the oxidation of the alloy on the air side.

In this work, the oxidation behaviors of alloys 430 and 441 in air with different concentrations of water vapor were studied. The effects of water vapor were different between 430 and 441, which may be attributed to both differences in the alloy composition and alloy grain size.

The effects of flow rate on the oxidation behavior of alloys 430 and 441 in dual atmospheres at 800 ℃ were also investigated. All the oxide scales were composed mainly of a surface $(Mn,Cr,Fe)_3O_4$ spinel layer and a Cr_2O_3 sublayer. For 441, the higher flow rate of Ar-5vol%H_2 resulted in the formation of Fe-rich nodules on the air side of sample.

To study the effects of alloy grain boundaries on the oxidation behaviors, alloys 430 and 441 with large grains were investigated in dual atmospheres oxidation. Initially, the scale formed on 430 air side contained many Fe-rich nodules along the alloy grain boundaries. Continuous oxidation led to the formation of three different microstructures, including $(Fe,Cr)_2O_3$, spinel phase and Cr-rich areas. For 441, only some isolated areas contained Fe-rich

nodules on the air side of the sample. Trapping of hydrogen by Fe_2Nb at the alloy grain boundaries area might contribute to the lower amount of Fe-rich nodules on 441 oxide scale.

To avoid cathode Cr poisoning in SOFCs, ceramic coatings are applied on the Cr-containing ferritic alloys used as interconnect. In this case, ferritic alloys with low Cr concentration could possibly be used. The samples with 13-18% Cr were evaluated by dual atmosphere oxidation experiments. With higher Cr concentration of the uncoated sample, quantities of Fe-rich nodules were reduced.

$(Mn,Co)_3O_4$-coated ferritic alloys with different Cr levels were studied by long-term oxidation in air at 800℃. The coated samples with relatively low Cr concentration have more scale spallation. The scale spallation is possibly related with the formation of $CoFe_2O_4$, which has a large mismatch of the thermal expansion coefficient with Cr_2O_3 and $(Mn,Co)_3O_4$.

Acknowledgments

I am grateful to my advisor Dr. Jeffrey Fergus for his expert guidance and help during my graduate studies at Auburn University. Without his persistent help, it is impossible for me to finish this dissertation. From Dr. Fergus, I not only acquired scientific knowledge but also the strict attitude for my future work.

I would like to express my appreciation to my committee members, Dr. Zhongyang Cheng, Dr. Dong-Joo Kim, Dr. Curtis Shannon for their helpful discussion and insightful suggestions. My grateful thanks also go to Mr. Steven Moore, Mr. L. C. Mathison and Mr. Roy Howard for the technical support. Financial support from the National Science Foundation (NSF-DMR-0551896) is gratefully acknowledged. Thanks also go to Energy materials group at Pacific Northwest National labs for their helpful suggestion and supply of spinel coated alloy samples. I am also grateful to James Rackowski and Dr. Matthew Bender of Allegheny Ludlum for providing samples of alloy 441 and the alloys with different Cr levels. I would specially give thanks to Matt Montgomery and Wendell Sandlin for their direction of the glass dual atmosphere experiment setup.

Thanks also go to my colleagues and friends, Dr. Kangli Wang, Yingjia Liu, Dr. Dileep Kumar, Honglong Wang, Adam, Dr. Zhongwu Zhang, Dr. Kewei Zhang, Lin Zhang, Dr. Peixuan Wu, Dr. Dan Liu, Zijie Cai, Dr. Wen Shen, Zhizhi Sheng and Wei Wang for all their generous help. A special thank is given to Adam for his excellent sample polishing work, which save me a lot of time.

I would like to give my most special thanks to my family: my wife Qi Xing, my father Shengcun Zhao, my mother Yumei Zheng, my two old brothers Bin Zhao and Wei Zhao for their everlasting love and unconditioned support. I could not find proper words to express the deepest appreciation for my parents. Without their support, it is impossible for me to finish graduate studies at Auburn University. I am really grateful for my brothers Bin Zhao and Wei Zhao, who take good care of parents for me. Special thanks also give to my wife for her accompany during my graduate life at Auburn University.

Table of Contents

List of Tables

List of Figures

List of Abbreviations

SOFC	Solid oxide fuel cell
PEMFC	Polymeric electrolyte membrane fuel cell
CTE	Coefficient of thermal expansion
ODS	oxide-dispersion-strengthened
SIMS	Secondary ion mass spectrometry
SEM	Scanning electron microscopy
EDS	Energy-dispersive X-ray spectroscopy
RE	Reactive elements
MOCVD	Metal organic chemical vapor deposition
LSC	$(La,Sr)CoO_3$
LSCF	$(La,Sr)(Co,Fe)O_3$
LNF	$La(Ni,Fe)O_3$
MCO	$(Mn,Co)_3O_4$
LSCF	$(La,Sr)(Co,Fe)O_3$
LNF	$La(Ni,Fe)O_3$
GNC	Glycine nitrate combustion
XRD	X-ray diffraction
EDM	Electrical discharge machining
ANOVA	Analysis of variance

CHAPTER 1

INTRODUCTION

The solid oxide fuel cell (SOFC) is a promising technology for clean power generation. Comparing to a polymeric electrolyte membrane fuel cell (PEMFC), a SOFC is operated at high temperature and has higher efficiency [1]. However, the high temperature creates some challenges for the materials used in the fuel cell. Development of interconnect materials is one of the challenges for the fuel cell components. As shown in **Fig. 1.1**, interconnects separate adjacent single cells in a planar SOFC. As the interconnect materials, the materials must satisfy the following requirement [2-5]:

- High electronic conductivities;
- Similar coefficient of thermal expansion (CTE) with other components;
- Low cost;
- Good machinability;
- Gas-tight;
- Chemical stability under SOFC oxidation environment.

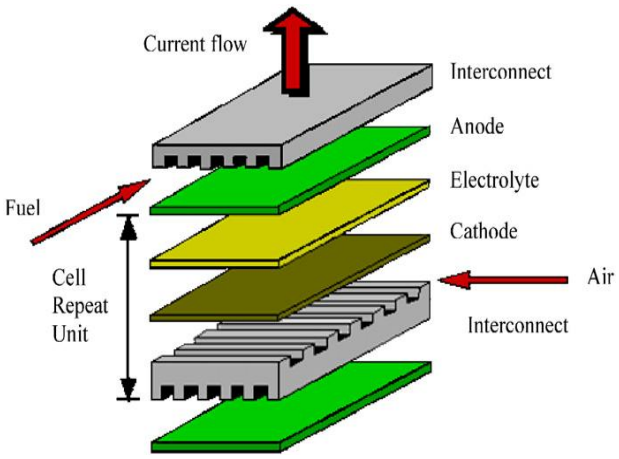

Fig. 1.1 Structure of SOFC[6]

Recent developments have allowed the SOFC operation temperature decrease to 800℃, so metallic materials can be used as the interconnect. Most studies have been focused on ferritic stainless steels and Cr-based oxide-dispersion-strengthened (ODS) alloys. Although Cr-based ODS alloy showed good performance, Cr-based ODS alloys are more expensive than ferritic stainless steels, so ferritic stainless steels are the most promising candidate for the interconnect materials.

Many ferritic stainless steels have been studied for the interconnect application. Due to its low cost and good conductivity, alloy 441 is one of the promising candidates. However, the application of 441 faces some problems, including relatively high oxidation rate and weak adherence of oxide scale. Another critical problem for 441 as the interconnect materials is the dual oxidation environment in SOFC. In SOFC, there is a hydrogen gradient between the two sides of the interconnect. Hydrogen may diffuse through the alloy and have a effect on oxidation behavior of $(Mn,Co)_3O_4$-coated 441. Although much work has been done, the oxidation mechanism of 441 has not been clarified yet, especially for the SOFC dual exposure (One side: wet H_2, the other side: air).

This work will examine the effects of water, hydrogen gas or air flow rate and alloy grain boundaries to the dual oxidation behavior.

Another problem with 441 is the volatility of Cr, which leads to the degradation of fuel cell. A protective coating is necessary for 441 applied in SOFC. Many coatings have been developed and their oxidation behaviors have been studied. One of the promising coating materials is $(Mn,Co)_3O_4$. With the protection of a $(Mn,Co)_3O_4$ coating, the Cr concentration in 441 may possibly be decreased. This would reduce the manufacture cost and less Cr may mitigate the Cr volatility from the alloy. This work will examine the oxidation behavior of $(Mn,Co)_3O_4$-coated ferritic alloy with different Cr levels.

1.1 Oxidation of Chromia-forming alloys

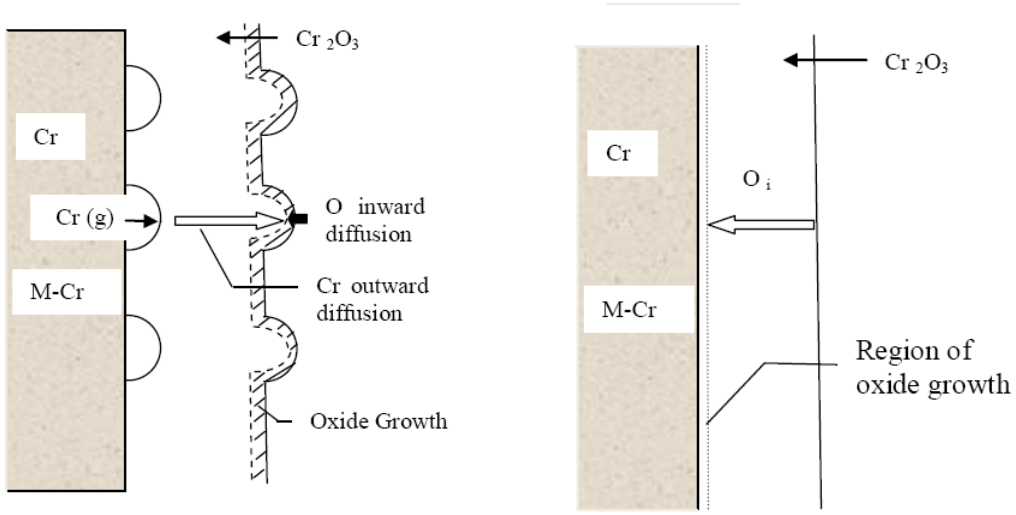

Fig. 1.2 Schematic presentation of the growth of Cr_2O_3 scales by: (a) Cr outward diffusion; (b) O inward diffusion.

The scales formed by oxidation of ferritic candidates for SOFC interconnect contain Cr_2O_3. **Fig. 1.2** shows the two mechanisms for the alloys containing Cr. Cr outward diffusion is the most common one (**Fig. 2a**) [7-9]. Cr vacancies in alloy are formed near the interface between the alloy and the oxide scale. Cr vacancies are formed at the surface of the oxide scale by **reaction 1.1**.

$$[4V_{Cr}^{'''} + 6V_O^{\bullet\bullet}]_{surface} + 3O_2 = 6O_O^x + 4V_{Cr}^{'''} + 12h^{\bullet} \qquad (1.1)$$

Then Cr in the alloy diffuses outward to fill the Cr vacancies formed by **reaction 1.1**. The outward diffusion may create vacancies at the interface between the alloy and the oxide scale. This may decrease the adherence of the oxide scale.

The other mechanism is the inward diffusion, as shown in **fig. 1.2b**. This often happens along a fast path, such as alloy grain boundaries. Oxygen interstitials are formed at the surface of the oxide scale and then diffuse through the oxide scale. The oxygen interstitials and Cr from the alloy react at the interface of the alloy and oxide scale by **reaction 1.2**.

$$[4V_{Cr}^{'''} + 6V_O^{\bullet\bullet}]_{surface} + 4Cr_{metal} + 6O_i^{''} = 6O_O^x + 4Cr_{Cr}^x \qquad (1.2)$$

Generally, the addition of reactive element, such as La and Y, improves the inward diffusion of oxygen and thus, the oxide scale reduced the porosities at the interface [2]. Oxide scale formed by inward diffusion has a higher adherence than that by outward diffusion.

For most ferritic alloys, the oxide scale growth rate follows a parabolic law [10], in which, an oxide scale is formed and limits both the cation outward diffusion and oxygen inward diffusion. So, for long term oxidation, the growth rate becomes slower.

1.2 Effect of water

1.2.1 Mechanism of Cr_2O_3 growth in water vapor

Water can promote the formation and adherence of Cr_2O_3 scales at high temperature oxidation [7, 11, 12]. Adhesion test of high speed steel (about 4-7.5% Cr) found that, the spallation of oxide scale in dry air was at the interface between the alloy and oxide scale, but the oxide scale spallation formed in wet air was within the oxide scale [12]. The adherence improvement with water is attributed to the inward growth of the scale by the diffusion of OH^- ions. In contrast, hydrogen dissolves in Cr_2O_3 and facilitates the metal cation outward transport, which reduces the adherence of the scale [11, 13, 14].

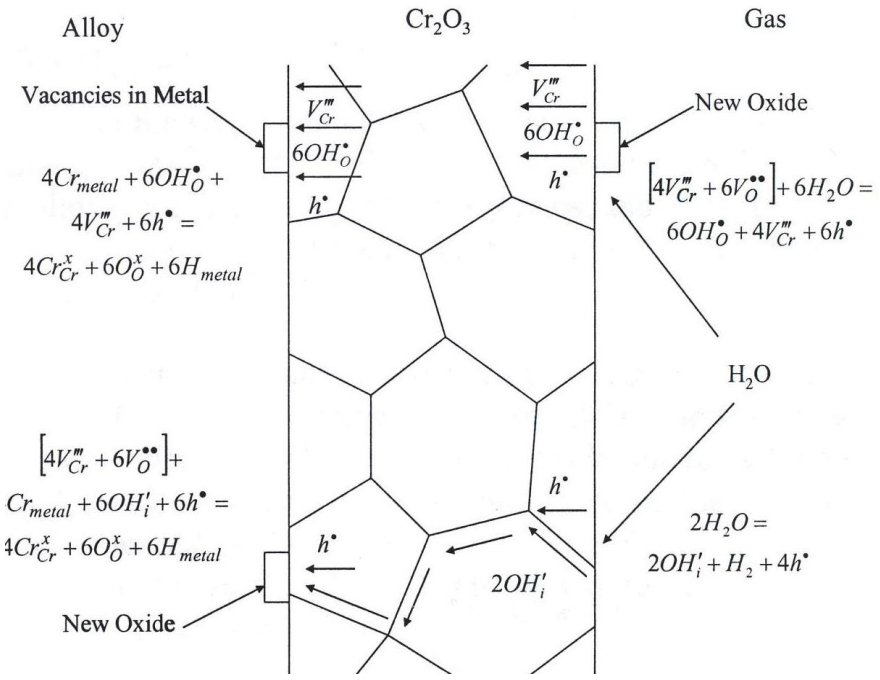

Fig.1.3 Mechanisms for Cr_2O_3 growth in presence of water vapor[9]

In the presence of water, there are two possible mechanisms for Cr_2O_3 growth. The first one is shown at the upper portion of **Fig. 1.3** and is similar to the **reaction 1.1** in the case of oxygen. Cr vacancies diffuse to the interface between alloy and oxide scale and then Cr from the alloy fills the vacancies. New oxides are formed at the surface of the oxide scale. The other mechanism is shown at the lower portion of **Fig. 1.3**. The OH^- defect and the electron holes diffuse into the scale by grain boundaries of oxide scale, such that the new oxides are formed at the alloy-scale interface [15]. Generally, the oxide scales formed by inward diffusion show a flat oxide scale and have a better adherence than those formed by cation outward diffusion [11, 15]. OH^- ions have relatively smaller size than oxide ion. This may lead to faster diffusion and most of the scale should formed by inward growth in the presence of water vapor [16]. The presence of water vapor increases the oxidation rate [11, 17-21].

1.2.2 Mechanism Cr poison at cathode in water vapor

In SOFCs, another critical problem is Cr poisoning of electrodes. When Cr-containing alloy is applied as the interconnect materials, Cr_2O_3 is formed in the oxide scale. The oxidation behaviors of Cr-containing alloys have been compared in dry and wet air. The oxide scale of ferritic Fe-25Cr steel showed a discontinuous $Mn_{1.5}Cr_{1.5}O_4$ spinel layer after 800℃ for 1150 hours in H_2-6 vol%H_2O, but the surface spinel layers formed in dry air was continuous after 800℃ for 1150 hours oxidation [22]. Crofer22 APU formed similar a discontinuous $MnCr_2O_4$ layer on the surface of oxide scale after oxidation at 900℃ for 2000 hours in air+10%H_2O [23]. Oxidation experiments with 304L also found that, at 600℃ for 672 hours in O_2-10%H_2O, the oxide surface contained

a higher concentration of Fe than that oxidized in dry air. A Cr deficient zone scale was formed at the interface of alloy and oxide [24]. In all cases these phenomena were attributed to the evaporation of Cr_2O_3.

Cr_2O_3 reacts with oxygen and volatile CrO_3 is formed following **equ. 1.3**. Under high humidity, predominant Cr_2O_3 evaporation products are volatile $CrO_2(OH)_2$ as shown in **equ.4** [23]**.** In the SOFC operation environment, $CrO_2(OH)_2$ is also the most dominant volatile component[25, 26].

$$Cr_2O_3(s) + 1.5O_2(g) = 2CrO_3(g) \quad (1.3)$$

$$Cr_2O_3 + 2H_2O(g) + 1.5O_2(g) = 2CrO_2(OH)_2(g) \quad (1.4)$$

As shown in **equ. 1.5** and **equ. 1.6**, CrO_3 and $CrO_2(OH)_2$ are reduced to Cr_2O_3 at the cathodes and degrade SOFC performances .

$$2CrO_3(g) + 6e^- = Cr_2O_3(s) + 2H_2O(g) + 3O^{2-} \quad (1.5)$$

$$2CrO_2(OH)_2(g) + 6e^- = Cr_2O_3(s) + 3O^{2-} \quad (1.6)$$

1.2.3 Mn function in steel alloys

In the oxidation of austenitic and ferritic alloys, Mn forms spinel phase with Cr, which may mitigate the oxidation rate and Cr evaporation in wet air [23, 27]. In ferritic alloys containing Cr and Mn, the oxide scale is composed of surface $(Mn,Cr)_3O_4$ spinel phase and inner Cr_2O_3. Generally, the diffusion rate of alloy elements in chromium oxide follows: Mn>Fe>Co>Ni>>Cr [28]. Thus, a Mn-rich spinel phase tends to form on the top of Cr_2O_3 for ferritic alloys containing Cr and Mn. A work compared the oxidation behavior of Crofer22 APU (22% Cr and 0.5% Mn) and Fe30Cr (30%Cr without Mn) [29].

Even with 30% Cr, Fe30Cr ($k_p=3.14\times10^{-13}g^2/cm^4\cdot s$) showed a higher weight gain than Crofer22 APU ($k_p=2.5\times10^{-14}g^2/cm^4\cdot s$) in air at 800 ℃ for 100 hours. Experiment in H_2-10%H_2O showed a similar trend. Cycle oxidation comparison of 304 and 430 at 900 ℃ found the similar results [30]. The oxide scale of 430 is composed of more protective $(Mn,Cr)_3O_4$ spinel and Cr_2O_3. Fe-rich oxide and $(Cr,Fe)_2O_3$ are formed on alloy 304. In a secondary ion mass spectrometry (SIMS) study, ferritic Fe-20Cr alloy (without Mn) were compared with 430 after oxidation in air-10% D_2O [31]. Higher intensity of D was found in the oxide scale of Fe-20Cr and less D was found in the oxide scale of 430. Oxidation behavior of ferritic alloy with different Mn concentration were compared at 750 ℃ in stagnant air [32]. With the increase of Mn concentration, the oxide scale growth faster. When Mn concentration is higher than 1%, Mn_2O_3 were formed in the oxide scale. Another work found that, after cyclical oxidation at 900 ℃ for 1000 hours in wet Ar-5 vol%H_2, MnO was formed at the surface of Crofer 22 APU (0.45% Mn) oxide scale [33]. Comparing the oxidation experiment results in dry and wet air, $(Mn,Cr)_3O_4$ spinel phase effectively reduced the oxidation rate in the wet air.

1.2.4 Mechanism of breakaway oxidation in wet environment

Breakaway type oxidation often occurs at Fe-Cr alloys in high temperature oxidation with high humidity [21, 27, 34]. Generally, Cr_2O_3 oxide scale forms to protect the Fe-Cr alloys from more severe oxidation. But, in air with high humidity, Fe-rich oxide scale is formed, which is called breakaway oxidation. Several mechanisms for breakaway oxidation behavior have been proposed. The first one is evaporation of volatile Cr species as described in **equ. 1.4** [26, 35-37]. 304L was tested in air-40%H_2O atmosphere

at 500-800^{o}C for 168 hours and Fe-rich breakaway oxide scales were formed [26]. This work found that the most rapid breakaway oxidation occurred at 800^{o}C and highest flow rate. Highest temperature and flow rate caused more severe Cr evaporation. At the environment of high temperature and flow rate, the Cr supply from the alloy is possibly not enough to make up the consumption of Cr by evaporation and caused the formation of non-protective Fe-rich oxide scale.

The second mechanism is that the breakaway type oxidation is caused by Cr internal oxidation [20]. A work tested isothermal oxidation of Fe-10%Cr and Fe-20%Cr binary alloys at 900℃ and 1050 ℃ for 72 hours. Three different environments were compared, including Ar-20%O_2, Ar-7%H_2O and Ar-4%H_2-7%H_2O. Hydrogen in Ar-4%H_2-7%H_2O reduced the dissociation of water and had slowest oxidation rate. The samples oxidized in environment containing water had Cr internal oxidation and Fe-rich phase was formed on the top of internal oxide. Another study summarized the ferritic alloys oxidation behaviors in steams [27]. For ferritic steels with low Cr concentration (such as 2.25%Cr), the oxide scale is composed of outer layer of surface columnar-grain magnetite and underlying equiaxed-grain Fe-Cr. The breakaway oxidation of high Cr ferritic alloys only occurred at some area and formed some Fe_2O_3 nodules with underlying Cr_2O_3 or $(Fe,Cr)_3O_4$ spinel phase. The interface between these two layers is expectedly the original metal surface.

The third possible mechanism is that the surface acidity causes the formation of hematite [38, 39]. **Fig. 1.4** shows the Raman spectroscopy image of oxide scale on Fe-15Cr-0.5Si-0.2Ti ferritic alloy after oxidation in water vapor (P_{H2O}=150mbar) at 900 ℃ for 8 hours. Fe_2O_3 nucleation site is located at the interface between the alloy and the

oxide scale. Fe_2O_3 nucleation tends to form at oxide scale cracks and internal interface decohesion area, where spalling of oxide scale occurs. At high temperature in water vapor atmosphere, acidity of oxide scale surface possibly controls the water decomposition, which controls the oxide growth rate. In acidic condition, Fe_2O_3 is more favored than Cr_2O_3. So, the growth rate of Fe_2O_3 is more rapid than that of Cr_2O_3 at crack and interface pores between the alloy and oxide scale [40].

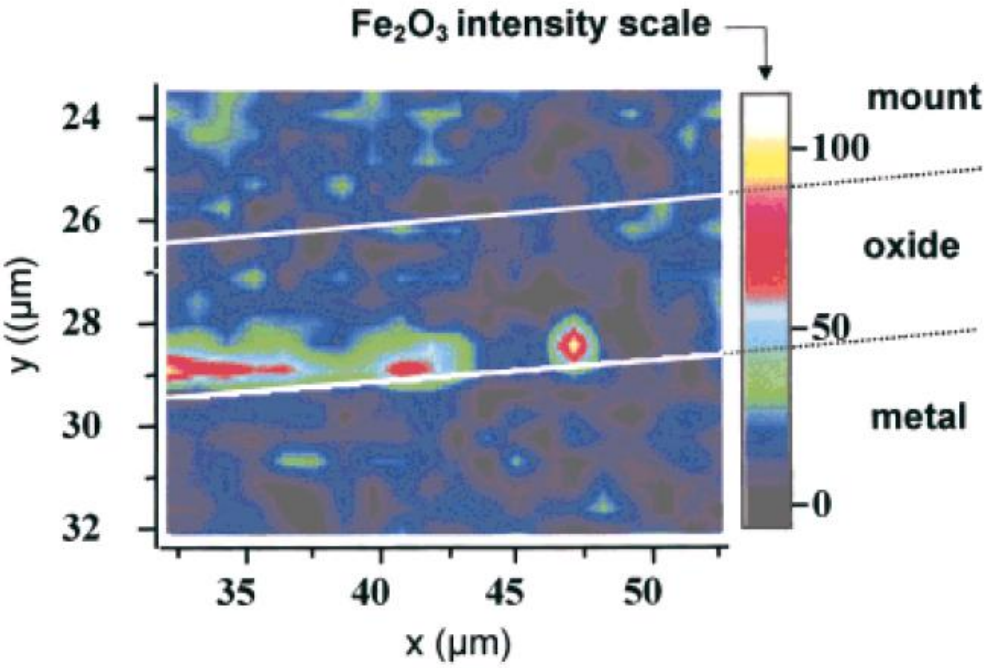

Fig. 1.4 Oxide scale of Raman spectroscopy image on a cross-section of on Fe-15Cr-0.5Si-0.2Ti stainless steel after oxidation at 900 ℃ for 8 hours in Ar-15%H_2O (Red spots: nucleation of Fe_2O_3.)[40]

1.3 Dual atmosphere oxidation

1.3.1 Introduction of dual atmosphere oxidation in SOFC

As shown in **Fig. 1.5**, in a SOFC, one side of interconnect is exposed to air and the other side is exposed to H_2. Due to the H_2 concentration difference between the two sides, H may diffuse through the alloy. The hydrogen in the alloy or oxide scale may affect the diffusion of other elements. A study on 430 found that, after dual exposure at 800 ℃ for 300 hours, the Fe concentration at the air-side surface of the oxide scale was higher than that exposed air on both sides [41]. In some areas, even the Fe_2O_3 nodules were found [41, 42]. This dual oxidation of metallic interconnects has been attracted much attention recently.

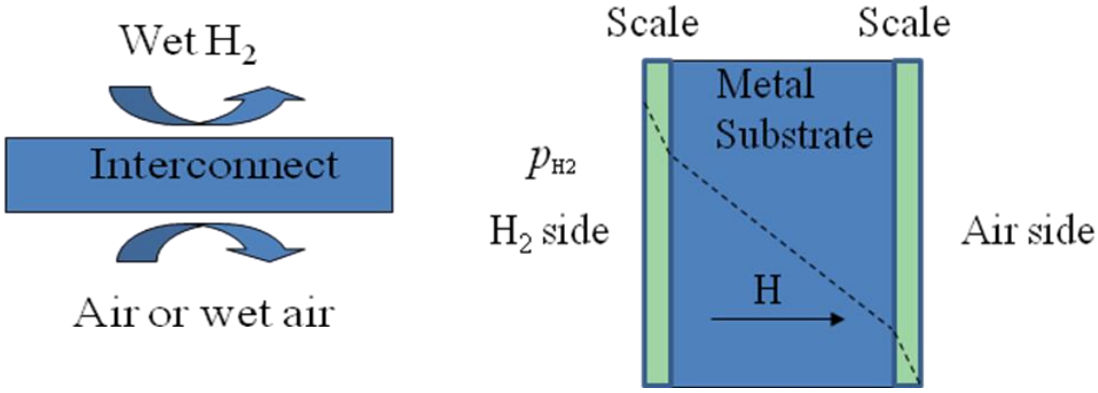

Fig. 1.5 Dual oxidation of interconnect in SOFC environment and H gradient distribution in interconnect.

Great efforts have been made to understand the oxidation mechanism. Most of the ferritic alloy candidates contain Cr and Mn. The oxide scales are mainly composed of a surface $(Mn, Cr, Fe)_3O_4$ spinel layer and a Cr_2O_3 sublayer. A 430 dual atmosphere

oxidation experiment was performed under the condition of 100 ml/min wet Ar-20vol%H_2 and100 ml/min dry air at 800℃ [43]. After 24-hour experiment, X-ray mapping found high concentration of Mn along the alloy grain boundaries. The oxide scale on the hydrogen side and the air-control samples both contained ridges along alloy grain boundaries. Alloy grain boundaries may act as the fast pathway for diffusion and play an important role for the high temperature oxidation of ferritic alloys. Although some work discussed the effects of alloy grain boundaries to the oxide scale growth, further systematic study is needed.

1.3.2 Function of reactive elements in alloy

Another important research direction for ferritic alloy interconnect is to improve the oxidation resistance in SOFC environment. During dual oxidation, the outward diffusion of cations is the dominate transport mechanism. During outward diffusion, voids are formed at the interface of alloy and oxide scale and reduce the adherence of oxide scale. For improving the adherence of the oxide scale, many new alloys were developed. The most common method is the addition of reactive elements (RE), such as Y, La Ce and Zr. A study compared stainless steels without RE (alloy 430) and with RE (ZMG232) [44]. After oxidation at 800℃ for various times, the interface between the oxide scale and alloys were observed. On the 430 interface, many cavities were found due to the segregation of impurities (Si, S, P and so on) at the interface, but ZMG232 did not show impurity segregation and spallation, which have been prevented by Zr and La RE in ZMG232. The effects of Y, Ce and La were compared by studying Fe-22Cr-0.5Mn alloys with these three RE elements [45]. Ce form dispersive segregation and has the

lowest resistance to cation outward diffusion. La is distributed in the oxide scale and may limit the cation outward diffusion along the oxide scale grain boundaries. Y is the most effective RE and Y segregations were found at the interface between the alloy and oxide scale. RE elements facilitate the formation of metallic form or oxide dispersion and suppress scale growth and segregation of impurities [8, 46, 47]. **Fig. 1.6** illustrates a dynamic-segregation model of the RE outward diffusion during high temperature oxidation [48]. The RE-rich oxide particles segregation at the metal-scale interface inhibits the formation of voids. RE-rich oxide particles diffusion along scale grain boundaries limits the outwards diffusion of cation ions.

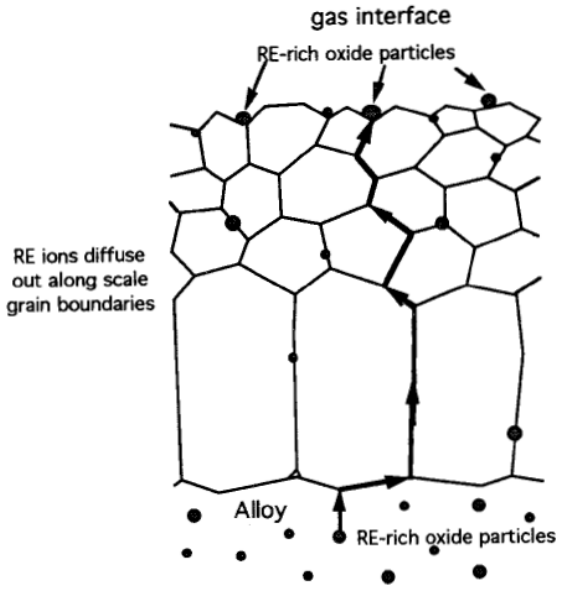

Fig. 1.6 Dynamic-segregation model for RE ions function during high temperature oxidation [48]

1.3.3 Hydrogen diffusion and absorption in steels

Hydrogen embrittlement has been intensively studied. Hydrogen gas can easily dissociate and diffuse into the steels and cause materials embrittlement. Hydrogen diffusivity in pure α ferritic iron followed the equation below [49]:

$$D_H = (5.12 \pm 0.6) \cdot 10^{-4} \exp\left(-(4.15 \pm 0.3)\text{kJ} \cdot \text{mol}/RT\right) \quad (1.7)$$

Based on **equ. 1.7**, the diffusivity of hydrogen in pure α ferritic iron at 800 ℃ is about $3\times10^{-4}cm^2/s$. The function of alloy elements has been studied. As shown in **Fig. 1.7a**, Addition of Cr alloy elements reduces the H diffusivity [50]. As alloy elements in α-Fe, Ti, V, and Nb were also found to strongly retard the hydrogen diffusion at temperatures below 200 ℃ **(Fig. 1.7b)** [49]. This study found that, with the reduction of hydrogen diffusivity, the hydrogen solubility increases. It is interesting that, at room temperature and 1 atm H_2, Fe-Nb-C (0.35%Nb and 0.066%C) had the highest hydrogen solubility ($3\times10^{-7}mol/cm^3$) comparing to the alloys with Ti, V, Zr, Nb and Mo. But the diffusivity is only $0.82\times10^{-6}cm^2/s$. This highest solubility of hydrogen in alloy containing Nb may caused by the deep-traps of hydrogen, which decreases the D_H.

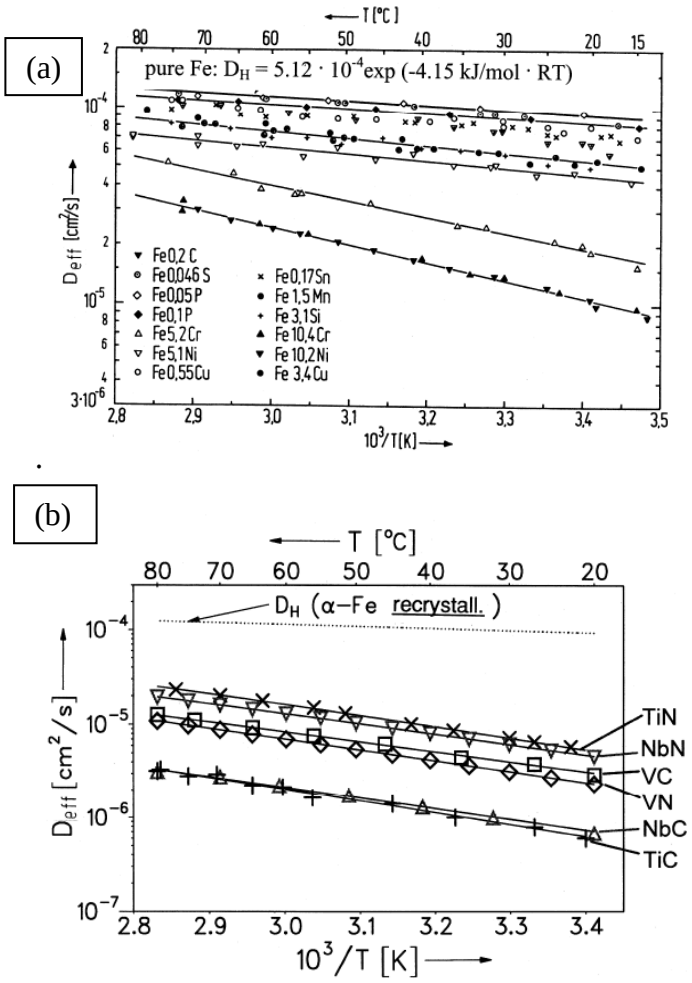

Fig. 1.7 Hydrogen diffusivity in α-Fe alloys at p_{H2}=1bar[49, 50]

Hydrogen trapping have been extensively studied in stainless steels. To reduce the hydrogen susceptibility of high strength steel, hydrogen trapping sites are introduced into steels to fix the hydrogen. This fixing can hinder the movement of hydrogen to the tip of a crack. The trapping sites can be classified reversible (<80kJ/mol) and irreversible (>80kJ/mol) trapping sites based on their binding energy with hydrogen. Reversible trapping sites include Fe-lattice, grain boundary, dislocation, microvoids and some substitution atoms [51-54]. For example, the activation energy for hydrogen diffuse in a iron lattice is only in the range of 5.69 to 7.12 from -40 to 550℃ [55]. Some second

phases are considered as irreversible sites, such as TiC or Ti(C,N) precipitation [54]. The irreversible TiC precipitations act as hydrogen sink, which reduce the hydrogen embrittlement. Besides of the TiC precipitations, the incoherent interface between TiC particles and the matrix create more hydrogen trapping sites [53]. The coherent and incoherent TiC precipitations have been compared [56]. In 0.42C-0.30Ti steel, the activation energy for hydrogen desorption from the incoherent TiC particles is 116kJ/mol at 650 ℃ and 700 ℃. When temperature is decreased to 500 ℃, the activation energy is 68kJ/mol. For the coherent TiC precipitates, the activation energy is only about 46 to 59kJ/mol in the temperature range of 500 ℃ and 700 ℃. Coherent interface shows a less activation energy than that of incoherent interface for hydrogen diffusion.

As shown in **Fig. 1.7b**, Nb had similar function as Ti, which forms a second phase as the irreversible site for hydrogen trapping. Another work compared the hydrogen trapping abilities of NbC and TiC [57]. Generally, NbC causes a higher lattice mismatch with the ferrite matrix than that caused by TiC, so the hydrogen trapping ability of NbC is possibly higher than that of TiC.

The dominant trapping sites are also determined by cold work. A thermodynamic analysis suggested that solid-solid interface, such as carbides, nitrides, and second-phase particles, is the dominant trapping sites for hydrogen for non-cold worked steel. With increased cold work, dislocations and microcrack become more critical for hydrogen trapping [58].

1.3.4 Nb

Hydrogen has a high solubility in alloys containing Nb. At 800℃, the hydrogen solubility in α-Fe is 2.4 cm^3 of gas at atmospheric pressure and 0℃ per 100g of metal. The solubility of hydrogen in Fe-20%Cr is similar to that in α-Fe. There is only data of hydrogen solubility in liquid Fe-Nb, which is 41.7 cm^3 at 1560 ℃ for sample containing Fe-15.12% Nb. The solubility of hydrogen in Fe-Nb also increases with increasing Nb concentration. The hydrogen solubility in liquid Fe is 25.5cm^3 at 1550 ℃. Hydrogen shows a higher solubility in liquid Fe-Nb than that in liquid Fe [59]. In solid state, the hydrogen solubility may have the same trend.

In steel containing Nb as an alloy element, Nb often forms Fe_2Nb phase, which has been applied to improve the high temperature strength [60-70]. The crystal structure of Fe_2Nb is AB_2 type C14 Laves phase, which have been extensively studied as hydrogen storage materials [71-74]. Most of the data about the C14 Laves phase are from room temperature experiments. Although high temperatures (800℃) are present in SOFC operation, the results of C14 Laves phase as hydrogen storage materials can still be used as instruction to understand the interaction between hydrogen and Fe_2Nb phase. Hydrides formed with Laves phase are very stable at room temperature, which limits the application of Laves phase as the hydrogen storage materials[72]. Generally, binary Laves phases have a mixture of metallic-covalent-ionic bond [74]. The hydrogen capacity of Laves phase decreases with 3d occupation number of B atoms [75]. **Fig. 1.8** shows the crystal structure of C-14 laves phase. As shown in **Fig. 1.8,** there are three possible tetrahedral interstice positions for hydrogen storage in C-14 Laves phase. The

interface between the Fe_2Nb Laves phase and the Fe matrix is incoherent and the coarsening rate of Fe2Nb is very faster [76].

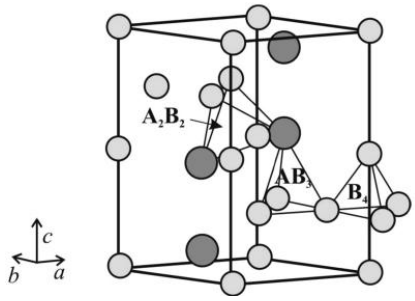

Fig. 1.8 The crystal structure of C-14 Laves phase with three tetrahedral interstices. [71]

Various alloys containing Nb have been developed as SOFC interconnects. During high temperature oxidation, Nb can quickly diffuse to the metal/oxide interface and may influence the oxidation behavior of alloys [77]. In another study, Nb, W and Si alloy elements were compared [78]. This work investigated the oxidation behaviors of several different alloys, including reference alloy (23.2 wt% Cr, 0.53%Mn, 0.16%La, 0.06%Ti , 0.03%Si) , and addition of 1%W, 2.7%W, 1%Nb, 1%Nb+0.25%Si, 1%Nb+0.42%Si, and 2%W+0.5%Nb+0.25%Si, respectively. Oxidation experiments were performed in laboratory air at 800℃ and 900℃. All the oxide scales were mainly composed of a top layer of $(Mn,Cr)_3O_4$ and a sublayer of Cr_2O_3. 1%Nb addition led to the highest growth rate of oxide scale. The others showed similar weight change. TEM results found that, after 1000 hours at 900℃ in air, 1%Nb addition leads to Nb-rich oxide at the metal/scale interface. Additions of 1%Nb+0.25%Si did not show this Nb-rich oxide area. Si and Nb can incorporate into the Laves phase precipitates, so the $(Fe,Cr)_2(Nb,Si)$ Laves phase has been attributed to the suppression of Nb oxide formation by 0.25% Si addition. Another Laves-phase forming alloy (Si: 0.11, Cr: 20.1, Mn: 0.50, Fe: 76.81, Nb: 0.36, Mo: 2.0, La:

0.08) was compared with alloy 430 in H_2-H_2O atmosphere ($p(H_2)$=1.8Kpa, $p(H_2O)$=11kpa) at 800 ℃ [79]. The oxide scales of the two alloys are both composed of Cr_2O_3 and $MnCr_2O_4$. After 72 hours oxidation, ridges along substrate grain boundaries were found in 430. The ridges have higher concentration of Mn and Fe. But for Laves-phase containing alloys, no distinct grain boundaries were found. The oxide scale growth rates of 430 and Laves-phase formed alloy are $4.5\times10^{-14}cm^2/s$ and $9.8\times10^{-15}cm^2/s$, respectively. The Laves phase (Fe_2Nb type) at the grain boundaries may contribute to the slower growth. This study also found a layer of inner Al_2O_3, which may improve the oxidation resistance. Additional ^{18}O diffusion studies [80] found lower diffusion coefficient ($7\times10^{-13}cm^2/s$) for Laves-phase formed alloy than 430 ($4.6\times10^{-12}cm^2/s$). As shown in **Fig. 1.9**, this study also proposed the mechanism for the oxide scale growth of 430 and Laves-phase forming alloy. The grain boundaries play an important role for the oxide scale growth. Laves phase precipitates may limited the outward diffusion of Fe, Mn and Cr.

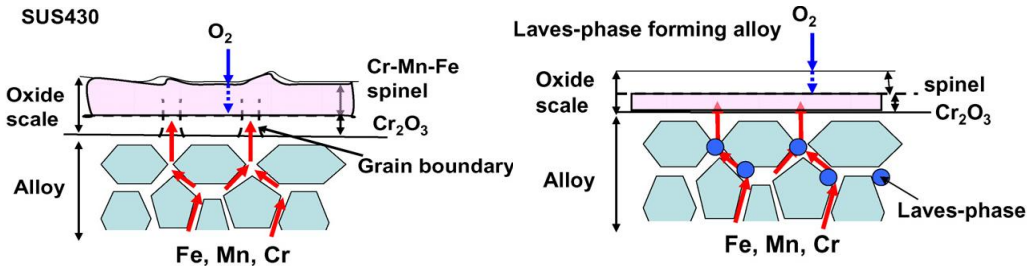

Fig. 1.9 The mechanism of oxide scale growth for 430 (left) and Laves-phase forming alloy (right). [80]

1.3.5 Alloy 441

Alloy 441 is a newly developed alloy as the interconnect materials. Nb and Ti are two very critical alloy elements for 441. Comparing to alloy 430, alloy 441 can alleviate the formation of SiO_2 layer, which reduce the conductivity of the SOFC [5, 81]. Furthermore, it is inexpensive. All these make alloy 441 one of the promising ferritic candidates as the interconnect materials. The most special feature for 441 is that Fe_2Nb Laves phase segregations are easily formed by annealing. At low temperature (600 ℃), the nucleation mainly occurs on dislocations. When the temperature increases to 750 ℃, grain boundaries nucleation becomes dominant [82]. Another study compared the adhesion of oxide scale for Fe-18Cr-TiNb (441) and Fe-18Cr-Ti (439) after oxidation in O_2/Ar atmosphere [83]. The study used water pressure to force spallation of the oxide scale from the alloy. As shown in **Fig. 1.10**, this study proposed an interface fracture mode for 441 and 439. For 441, the TiO_2 and Fe_2Nb Laves phase precipitated at the alloy grain boundaries. The fracture occurred between the TiO_2 and Fe_2Nb-type precipitation. Another work found the similar phenomena for 441 [84]. The Fe_2Nb-type precipitation may stabilize the grain boundaries and avoid the grain growth during high temperature oxidation. For alloy 439, the fracture of oxide scale mainly occurred at the interface of TiO_2 and chromia. In this work, alloy 439 showed higher adhesion energy than alloy 441. Thus, it seems that Ti is beneficial for the adhesion of oxide scale and Nb is harmful.

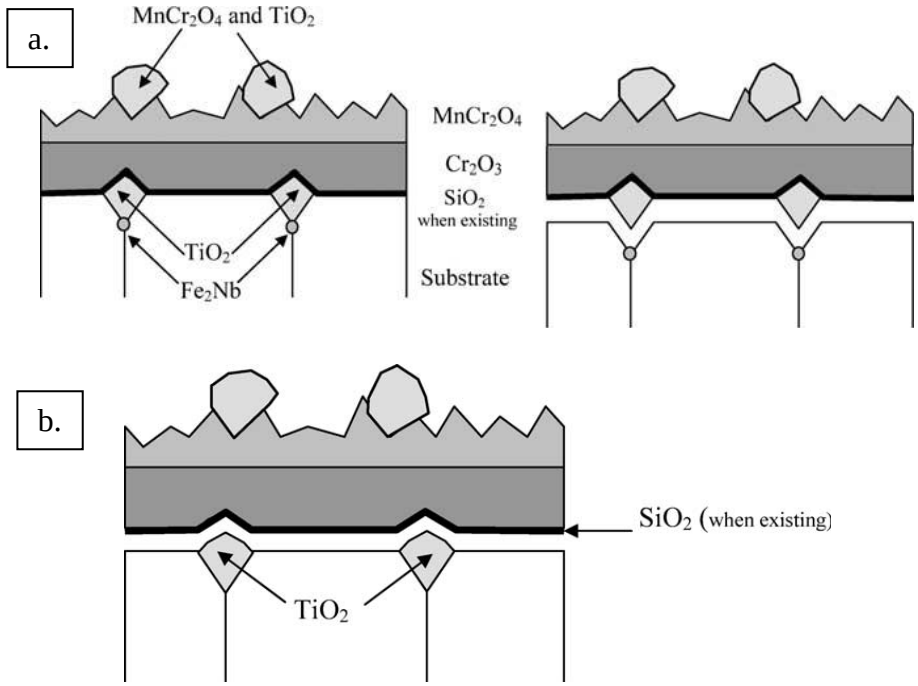

Fig. 1.10 Interface fracture mode for (a) 441 (Fe-18Cr-TiNb); (b) 439 (Fe-18Cr-Ti).[83]

A study developed a method to determine the critical interfacial shear strength between oxide scale and the alloy substrate by micro indentation test [85]. This work found that the interfacial strength between CROFER22 APU oxide scale and the substrate degraded with increased oxide scale thickness. The predicted interfacial shear strength of CROFER 22 is about 450MPa. This is consistent with that the growth of oxide scale caused stress at the interface, which leads to the buckling of the oxide scale. Interfacial flaws will also decrease the adherence between the oxide scale and substrate.

The interfacial shear strength of 441 oxide scale and substrate was also studied by indentation test [86]. The growth stress of the oxide scale and thermal stress after stack cooling between the oxide scale and the substrate leads to the buckling and spallation of the oxide scale. This work investigated the interfacial strength between the oxide scale

and the 441 substrate. Based on the indentation test results, the oxide scale is not stable when the oxide scale is over 2μm. This is consistent with the growth of the oxide scale generating stress at the interface. The indentation test results are scattered, which was attributed to the rough surface. Based on SEM image, interfacial defects were most found at the grain boundaries. Previous work found that the oxide scale fracture of 441 tend to happen at the grain boundaries [83]. Oxide scale fracture at grain boundaries played a critical role for the interfacial strength between the oxide scale and substrate. The interfacial shear strength of 441 is less than 325MPa, which is lower than CROFER 22 APU. In addition, the Cr_2O_3 reacts with H_2O to form $CrO_2(OH)_2$ phase, which are more easily evaporated.

The oxidation behavior of 441 as SOFC interconnect has been studied extensively. At initial stage, the oxidation products are Fe_2O_3/Cr_2O_3 at 650℃ in air and water vapor. When temperature increase to 850℃, the oxidation scale was composed of $(Fe,Cr)_2O_3/Cr_2O_3$. With longer oxidation, Cr concentration in the scale increase [87]. After the oxide scale becomes stable, the oxide scale of 441 are mainly composed of surface $(Mn,Cr)_3O_4$ spinel phase and underlying Cr_2O_3 scales at the SOFC operation temperature.

In dual atmosphere oxidation exposure at 800 ℃ for 300 hours (wet H_2 side: 35ml/min, wet air: 70ml/min), there was a much thicker oxide scale on the air side of 441 interconnect than on a sample in which both sides were exposed to air. Comparing with control sample, a Fe_2O_3 layer was formed on the top of oxide scale at air side [88]. In this work, 430 was also tested in the same dual oxidation and only some localized Fe_2O_3 nodules and a little high Fe concentration were found on the surface microstructure of 430. Dual oxidation of $(Mn,Cr)_3O_4$ coated 430 and 441 also found similar trend [89, 90].

The dual test parameter is 500cm^3/min 97%air+3%H_2O at air side and 100cm^3/min 97%H_2+3%H_2O at H_2 side. After 800℃ for 800 hours dual oxidation, the Cr_2O_3 thickness of 430 and 441 are about 1μm and 4 μm, respectively. Hydrogen has a very high diffusivity in Nb, which has been considered as one of the promising materials for hydrogen permeable membranes [91]. One work compared several different combination of Nb and Ta [92] and found that, in the range of -83℃ and 227℃, the hydrogen diffusivity increased with increase Nb concentration. The study of ternary Ni–Ti–Nb alloys found the similar trend [93]. Many studies have expected that the high H diffusion along the grain boundaries was the reason for this anomalous growth of 441 oxide scale in dual oxidation. However, another study found a conflicting result that laves phase distributes both in the grain and at the grain boundaries [81]. This contradiction may need further organized work to study with different grain size.

1.3.6 Cr

Cr_2O_3 oxide scale can reduce the hydrogen diffusion through the alloy. As shown in **Fig. 1.5**, the diffusion coefficient of hydrogen in alloy is different from that in Cr_2O_3 layer. Hydrogen diffusion experiment showed that the H diffusivity in Cr_2O_3 was four orders of magnitude lower than that in Fe in simulated SOFC atmosphere [94, 95]. At 1000℃, the defects caused by hydrogen diffusion are neutral hydrogen atoms at the oxygen site, which is proportional to $a_{H2}^{\ ½}$ and $a_{O2}^{-1/8}$[94]. In a work, the oxidation behaviors of Cr with and without hydrogen were compared at 900℃ in 20mbar isotopically labeled molecular oxygen [96]. It was found that hydrogen effectively improves the Cr outward diffusion and limited the oxygen inward diffusion in the Cr_2O_3

layer. This leads to less growth of oxide scale at the interface between the alloy and oxide scale, which cause less adherent oxide scale[96].

Cr is used in stainless steel to forms a dense Cr_2O_3 layer which limits the oxygen inward diffusion. A mathematic model has been created to calculate the minimum Cr concentration for forming continuous oxide scale [19, 20]. This model includes two criterions for the Fe-Cr alloys. Firstly, as shown in **equ. 1.8**, the Cr concentration in the alloy is high enough for outward diffusion to limit internal oxidation:

$$N_{Cr}^{(1)} > [\frac{\pi g^*}{3} N_O^{(S)} \frac{D_O V_m}{D_{Fe-Cr} V_{CrO_{1.5}}}]^{0.5} \quad (1.8)$$

Where, $N_{Cr}^{(1)}$: critical Cr concentration (1)

$N_O^{(S)}$: oxygen solubility in the alloy;

D_O : oxygen diffusivity in the alloy;

$D_{Fe\text{-}Cr}$: alloy interdiffusion coefficient;

V_m and $V_{CrO_{1.5}}$: molar volumes of the alloy and oxide;

g^* : factor.

If Cr is the element being internally oxidized, then g^* is about 0.3. In the case that Fe is also considered, the critical solute concentration based on **equ. 1.8** is higher. It is caused by the increase of transient oxide.

The second criterion is for that, after the formation of continuous external scale, the Cr supply from the alloy must supply enough Cr to make up the consumed Cr by scale growth. This criterion may be expressed by the following equation:

$$N_{Cr}^{(2)} = \frac{V_m}{32\nu}\left(\frac{\pi k_p}{D_{Fe-Cr}}\right)^{0.5} \quad (1.9)$$

Where, $N_{Cr}^{(2)}$: critical Cr concentration (2)

k_p : the parabolic rate constant for oxide scale growth.

Based on this model, 9-10wt%Cr is necessary to achieve a protective external oxide scale at temperature below 900 ℃.

The effects of alloys with different Cr concentrations were experimentally compared, [19, 42]. A work compared the Fe-Cr ferritic alloys with different Cr concentration [19] indicated that after oxidation in dry air for 96 hours at 650 ℃, the Fe-Cr alloys with Cr>13.5% formed a continuous Cr_2O_3. Due to the Fe transition oxidation, this value is a little higher than the predicted value based on the mathematic model. In another work, alloy 430 (17%Cr) and Crofer22 APU (22.8%Cr and 0.06%La) were compared after dual oxidation at 800 ℃ for 300 hours [42, 97]. Fe_2O_3 nodules were formed at the surface of the 430 air side. A layer of SiO2 was formed at the interface between the oxide scale and the alloy. However, only a little high concentration of Fe (8%) was found at the top spinel phase in Crofer22 APU. The oxide scale of Crofer22 APU with both side exposed to air contained only less than 1% Fe. This comparison indicates that higher Cr concentration can alleviate the formation of Fe-rich nodules.

The oxidation behavior of ferritic alloys with different Cr concentration (6,9,12,18,22%Cr) were compared after 2000hr oxidation at 800 ℃ in wet air (3vol% H_2O) [98]. Alloys with low Cr concentration (6, 9 and 12% Cr) formed a Fe-rich oxide scale. Alloys with higher Cr concentration formed a protective oxide scale with some Fe-rich nodules. Due to the long exposure time (2000hr) and H_2O in the air, Cr deficient

zone may have formed and the oxide scale had a little higher Fe concentration. Another work compared the Fe-10Cr and Fe-20Cr oxidation behavior[20]. After 72 hours at 900℃ oxidation in Ar-20%O_2, Fe-20Cr oxide scale was composed of protective Cr_2O_3. The oxide scale of Fe-10Cr is composed of Fe-Cr spinel and Fe_2O_3. Cycle oxidation of Fe-Cr alloys, including 9, 12, 17, 20, 25, 30% Cr, were systematically studied in temperature range of 600 to 950℃ in Ar-20vol% O_2 and Ar-20%O_2-5%H_2O[21]. This work found that, at temperature between 700 and 950℃, higher Cr concentration is required for protective oxide scale at higher temperature. Based on others' work, higher Cr concentration improves the oxidation resistance of ferritic stainless steels at the SOFC operation temperature range.

1.3.7 La, Y and Zr

Other important reactive elements include La, Y and Zr. A new alloy (16.5%Cr, 1.05%Mn, 0.005%La, 0.018%Y and 0.11%Zr) have been developed as the interconnect materials[99]. After 1000hr isothermal and cycle oxidations, this alloy show similar level of oxidation growth rate. The good adherence of the scale might have been contributed by the small amount addition of La, Y and Zr. La did not form intermetallic compound with iron and distributed in the substrate evenly [8]. This may prevent the outward diffusion of cations and improve the adherence of the oxide scale. Crofer 22 APU is one of the alloys specially developed as the interconnect material, which contains 0.06% La and 22.8%Cr. A dual oxidation experiment of Crofer22 APU (thickness: 0.5mm; wet H_2: 5ml/min; Air side: ambient air or wet air) was done for 300 hrs at 800℃ [34]. When exposed to wet air in dual oxidation, Fe_2O_3 –rich nodules were found at the air side, but

the air side exposed to ambient air showed no Fe_2O_3 at all. The authors suggested that iron transportation is accelerated by water vapor at air side, but the paper did not provide a clear explanation. Water vapor may increase this inward diffusion of O and increase the adherence of this oxide scale, so the Fe_2O_3 may be observed at the wet air side in dual oxidation. In drier air, the Fe_2O_3 may easily spall off. The Fe_2O_3 nodules at wet air side may not means accelerated oxidation behavior. The further study investigated the TEM microstructure of Crofer 22 APU after dual oxidation (800℃ for 300hrs, wet H_2: 5ml/min; Air side: ambient air) [42]. TEM observation found higher Fe concentration in the top spinel phase than that of air control. No hematite (α-Fe_2O_3) nodules were found, but at the air side of 430, hematite nodules were observed. Crofer 22 APU showed a better oxidation resistance than 430 in dual atmosphere. Crofer 22 APU is specially developed as interconnect materials and very expensive.

1.3.8 Effects of substrate grain size and boundaries

Grain boundaries are fast paths for Cr, Mn or Fe outward diffusion [26, 100, 101]. At 300-380 ℃, the diffusivity of Cr along the grain boundaries is 4-5 orders of magnitude higher than that in Fe lattice. At 840 ℃, it is even a 3 orders of difference[102, 103]. At 300-380ºC, the diffusivity of Cr in α-Fe with 10-25nm grain size is 7-9 orders higher than that in α-Fe lattice [104]. This work considered that the enhanced Cr diffusivity in nano-grain size α-Fe is attributed to a large volume of non-equilibrium grain boundaries with high concentration of dislocations and large quantities of triple junctions. Fe-15%Cr and Fe-18Cr alloys were oxidized in supercritical water with 25 μg/L oxygen at 500 ℃ for up to 1800 hours [105]. For both Fe-15Cr and Fe-18Cr, 15 μm and 1 μm grain sizes were

tested. Weight gain data show less weight change for alloys with smaller alloy grain size. Comparing the oxide scale surface, Fe-15Cr with 15 μm alloy grain size formed Fe-rich nodules and Fe-15Cr with 1 μm grain size formed a smooth Cr_2O_3. The smaller grain size reduced the Cr concentration needed to form a protective Cr_2O_3 oxide scale.

Other studies found similar trend. At 600-800 ℃ in water vapor/oxygen mixtures, 304L showed break down oxidation behavior. However, the break down oxidation was inhibited by the Cr diffusion along the grain boundaries area [26]. A work compared low-alloy ferritic steels (055-2.29%Cr) and one austenitic steel (TP347: 17.5%Cr, 1.84%Mn, and 10.7% Ni) [106, 107]. For low-alloy ferritic steels, the weight gains after 72 hours at 550 ℃ in air decease with increasing grain size. This is attributed by the fast O inward diffusion along the substrate grain boundaries. TP347 does not follow this trend after 750 ℃ for 120hr in lab air. For alloy 347 with 4 μm and 11 μm alloy grain size, the oxide scale is composed of Cr_2O_3 with localized $FeCr_2O_3$ nodules. For 347 with 65 μm grain size, the scale is composed of non-protective Fe oxide. Considering the Cr supply to the alloy/oxide interface, higher Cr concentration is necessary for coarse-grained materials to achieve a protective Cr_2O_3 layer on the entire surface than that for fine-grain materials.

Hydrogen embrittlement is an important topic in metal materials. Hydrogen has a strong tendency to segregate at microstructure defects. As shown in **Fig. 1.11**, it is found that, by tritium autoradiography, hydrogen tends to segregate at the grain boundaries area. At grain boundary area, the hydrogen trapping is reversible or irreversible, depending on the trapping energy. In stainless steels, second phase tends to segregate at the grain boundaries area. The hydrogen diffusivity in two austenitic stainless steels Fe-25Ni-15Cr

(containing Ti) and Fe-25Cr-20Ni (no Ti) with different grain size was compared at room temperature [108]. Generally, smaller grain sizes lead to higher hydrogen diffusivity due to more short-circuit diffusion along grain boundaries. In these two alloys, η-Ni3Ti formed in Fe-25Ni-15Cr and σ-FeCr precipitations were formed in Fe-25Cr-20Ni by annealing. The relationship between the reciprocal grain size and hydrogen diffusivity is linear for Fe-25Cr-20Ni (no Ti). But the Fe-25Ni-15Cr with η-Ni3Ti showed a much less hydrogen diffusivity than that without η-Ni3Ti. The difference should be attributed by the hydrogen trapping inη-Ni3Ti. σ-FeCr does not limit the diffusion of hydrogen.

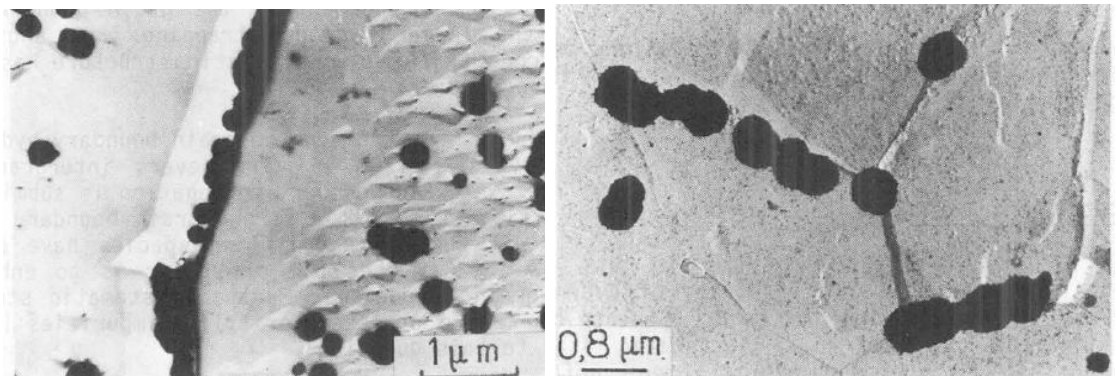

Fig. 1.11 Hydrogen segregation at alloy grain boundaries (top: Armco iron[109]; Bottom: maraging steel [110]).

The effects of grain size to the Fe_2Nb Laves phase nucleation in 441 are studied in another work [82]. The Fe_2Nb nucleation is controlled by the diffusion of Nb. Large grains increase the diffusion distance for Nb to the alloy grain boundaries, so large grain size lowers the Laves phase formation at grain boundaries.

1.4 Coating development for SOFC stainless interconnect application

Based on current oxidation results, it is difficult for ferritic stainless steel to be used directly as SOFC interconnect. For improving the oxidation resistance and reducing the Cr poisoning, various coatings were developed as the protection layer of metallic interconnects, including reactive element oxide, rare earth perovskite, spinel and MAlCrYO coatings [111].

1.4.1 RE oxide coatings

As discussed before, addition of RE in stainless steels improves the adherence of oxide scale and effectively reduces the high temperature oxidation rate. A study investigated the thin coating of La_2O_3, Nd_2O_3 and Y_2O_3 on Crofer 22 APU [2, 29]. The coating was added by metal organic chemical vapor deposition (MOCVD). The effects of the coatings were studied by comparing the oxidation behavior of uncoated and coated at 800℃ for 100hr. Comparing the oxidation weight change, the three coating showed about 35% improvement than uncoated Crofer 22 APU. The coatings formed barrier to limit the Cr outwards diffusion. During oxidation, Cr reacted with La_2O_3 and formed perovskite $LaCrO_3$. Nd_2O_3 coating had the similar reaction and formed perovskite $NdCrO_3$ phase. During oxidation experiments, homogenous cracks were found at the surface of oxide scale on the Y_2O_3 coated sample. Oxygen has a higher permeability in Y_2O_3. Chromia grew between the alloy and the Y_2O_3 coating, which generated stresses and created cracks. In this study, La_2O_3-coated Crofer 22 APU showed the best conductivity. In H_2-10% H_2O environment, the oxidation weight change of Y_2O_3-coated Crofer 22 APU is higher than the La_2O_3 and Nd_2O_3-coated Crofer 22 APU. In air

oxidation, La distributed between the chromia layer and top spinel phase. In H_2-10% H_2O, high concentrations of La and Mn were found at the surface of oxide scale. The oxide scale of Nd_2O_3-coated Crofer 22 APU showed similar trend. A study of Nd_2O_3 coated Fe-30%Cr alloy find that the coated samples have small and equiaxed oxide grain[112]. Comparing to the coarse and columnar oxide grains for uncoated samples, the small and equiaxed oxide grains on the Nd_2O_3 coated Fe-30%Cr alloy effectively increase the resistance to cycle oxidation. 200nm thickness Ce/Co and Y/Co coatings were also studied in another work [113]. The coatings were applied by sol-gel method. After 1000 hours oxidation at 750℃ in air, both Ce/Co and Y/Co coated 430 show less thick oxide scale than that uncoated 430. CeO_2 was found at Cr_2O_3/spinel interface. Y dissolved into Cr_2O_3, especially through the oxide grain boundaries. Although the RE oxide coating showed improvement to reduce Cr diffusion, the coating is very thin and porous, that make them not suitable as Cr barriers for long term.

1.4.2 Rare earth perovskite coatings

Conductive perovskite compositions are often used as the cathode and interconnect of SOFCs. It is promising for perovskite coatings as the coating materials of interconnect. The formula of rare earth perovskite coatings is ABO_3, where A is trivalent rare earth cation (e.g., La and Y) and B is trivalent metal cations (e.g., Cr, Ni, Fe, Co, Cu and Mn)[111]. Firstly, the rare earth elements diffuse into the oxide scale and improve the high temperature oxidation resistance. Secondly, the coatings can be doped with other elements (e.g., Sr, Ca, Ni, Fe, and Cu) to increase conductivity and modify the CTE of the rare earth perovskite coatings [5].

4-5 μm $La_{0.8}Sr_{0.2}CrO_3$ and $La_{0.8}Sr_{0.2}FeO_3$ coatings on ferritic alloys were compared at 800 ℃ for up to 1200 hours [114]. The coatings were applied by radio frequency-sputtering. $La_{0.8}Sr_{0.2}CrO_3$ coated samples showed a slower oxide scale growth rate than $La_{0.8}Sr_{0.}2FeO_3$. $La_{0.8}Sr_{0.2}FeO_3$ is not very effective to prevent Cr outward diffusion. $La_{0.8}Sr_{0.2}CrO_3$ contains Cr, which may diffuse outwards and leads to the Cr poison of cathode. In another work, 150nm $La_{0.8}Sr_{0.2}CrO_3$ and $LaCr_{0.9}Zn_{0.1}O_3$ thin coating on Ebrite, which contained 26.3%Cr and 1.01%Mo, were developed by spin-coating method [115]. The oxide scale development of coated sample is closely related with the temperature. At 850 ℃, Cr_2O_3 grew through the coating. At 750 ℃, Cr_2O_3 grew under the coating. This may also be related with the thin thickness of the coating. The coating is also effective to prevent the Cr evaporation by about 70%.

$(La,Sr)CoO_3$ (LSC), $(La,Sr)(Co,Fe)O_3$ (LSCF), and $La(Ni,Fe)O_3$ (LNF) coated ferritic alloys (Crofer22 APU, E-Brite and 430) were studied [116]. The coatings were applied by electron-gun PVD process and the coating thickness is about 1000nm. After 1000 ℃ for 3 hours and 850 ℃ for 168 hours heat treatment in the air, all the films are composed of target perovskite film, and a spinel intermediate layer. There is trace of $SrCrO_4$ phases in coating containing Sr. Another study of LSC coated Fe-25Cr alloy also find this $SrCrO_4$ interface between the LSC coating and fine Cr_2O_3 layer (100nm) after oxidation at 800 ℃ for 1150 hours [22]. At high temperature, perovskite B-site cations (Ni, Fe, Co) diffuse inward and form stable spinel with transition metals from the metals. The outer perovskite coating and spinel phases can limit the outward diffusion of Cr.

The effects of electrodeposited Co (matrix)/$LaCrO_3$ coating on 430 were developed [117]. Comparing the Co-coated with Co/$LaCrO_3$ coated alloy 430, $LaCrO_3$ improved the adherence of the oxide scale. The authors consider that it is the function of reactive elements. After 800℃ for 2040 hours, the oxide scale is composed of surface Co_3O_4, mid-layer of Co-Fe spinel and inner Chromia. Due to the larger CTE of Co_3O_4 than that of Co containing spinel phase, detachment of oxide scales were found between the surface Co_3O_4 and Co-Fe spinel phase. Other studies of Co coating also find the CTE mismatches between the Co coating and the oxide scale just after oxidation at 800℃ [89, 118].

$LaMnO_3$, Sr-doped $LaMnO_3$ and Ti-doped $LaMnO_3$ were also developed as the coating materials of interconnect [119]. The three coatings were applied at the surface of Haynes 230 by sputtering and the thickness was 1μm. The properties of coatings were compared by oxidation in air at 800℃ for up to 1080 hours. Ti suppressed the oxygen vacancy concentration and Ti-doped $LaMnO_3$ coating showed best oxide resistance. Contrarily, Sr increased the oxygen vacancy concentration and Sr-doped $LaMnO_3$ had thickest oxide scale in this three candidate coatings.

Comparing to uncoated samples, perovskite coatings reduced the oxide scale growth. But their applications as the interconnect coating face some other problems. Firstly, due to the ionically conducting nature, the rare earth perovskite coatings do not effectively prevent Cr migration or absorb Cr, which cause Cr poisoning. Secondly, perovskite films are oxygen diffusers and it is difficult to get very dense coating microstructure. [111]

1.4.3 Spinel coatings

For reducing the chromium poison, the most common element used is Mn. Mn can form a $MnCr_2O_4$ spinel layer at the top of oxide scale, which limits the Cr volatilization. This leads to the development of spinel coatings for interconnect application. The spinel phase has the formula of AB_2O_4 (A and B: divalent, trivalent and quadrivalent cations at octahedral and tetrahedral sites. O: face center of face-center cubic lattice) [111]. Spinel phase also have a good CTE match with the ferritic substrate and other cell parts.

$NiMn_2O_4$ spinel coating were evaluated as the coating of 430 [120]. Due to the low cost of Ni, $NiMn_2O_4$ has the cost advantage comparing to $MnCO_2O_4$. After 10 cyclic oxidations at 750℃ for 1000 hours, the oxide scale is composed of inner layer of Cr_2O_3 and an out layer of $NiMn_2O_4$ and Mn_2O_3. The formation of $MnCr_2O_4$ was depressed. Comparing to $MnCo_2O_4$ coated 430, $NiMn_2O_4$ coating decreased the weight gain a little. But EDS scanning found that high concentration of Cr in the coating, which limited the applications of $NiMn_2O_4$ as the coating of ferritic interconnect.

$(Mn,Co)_3O_4$ (MCO) is one of promising spinel coatings. MCO has very close thermal expansion coefficient (11.4×10^{-6}/℃ for $Mn_{1.5}Co_{1.5}O_4$ and 12 to 13×10^{-6}/℃ for ferritic stainless steel) to LSM and good electronic conductivity [84, 97, 121-124]. The interfacial strength of the oxide scale and MCO coating is much higher than that of the oxide scale and alloy substrate [125]. Comparing to perovskite coating, such as $La_{0.6}Sr_{0.4}CrO_3$ and $La_{0.6}Sr_{0.4}CoO_3$, MCO coating also showed a higher resistance to Cr vaporization [22]. An on-cell test was performed to evaluate the oxidation, Cr evaporation and electrical properties of electroplated MCO coating 441 [90]. The on-cell test flow rate is $500cm^3$/min 97%air-3%H_2O at air side and $100cm^3$/min 97%H_2-3%H_2O

at H_2 side with a constant electrical load of 0.7V. After 800℃ for 850 hours test, Fe and Cr were not found in the MCO coating. The MCO coated 441 also showed a higher and more stable power density than that of bare 441 and 800℃-500hour preoxidized 441. MCO coating effectively blocks Cr outward diffusion and improves electrical properties as the interconnect materials.

In another work, isotope oxygen exchange method ($^{16}O/^{18}O$ exchange) was used to study the O diffusion in the oxide scale of ZMG232-M0 (Mn: 0.48, Ni: 0.26, Cr: 21.99, Al: 0.14, La: 0.04, Zr: 0.22, Fe: 76.49 in mass%) [126]. The samples without and with MCO were examined by isotope oxygen exchange method. The oxygen can diffuse deep inside the Mn–Co spinel coating layer. A two-stage step decrease of ^{18}O concentration was found. First step was near the surface spinel coating. High diffusion may have been caused by grain boundaries or nano-micro meter sized pores. With increase depth, the spinel coating became denser and O inward diffusion became more difficult. Second step was caused by less diffusivity of O in Cr_2O_3.

The performance of the MCO coating is determined by the coating process. A study compared the MCO coating by glycine nitrate combustion (GNC) synthesis+dip and co-precipitation +spray [127]. The coating by GNC synthesis reduced the chromium vaporization by factors of only 2–3 due to the high porosity of coating layers. Another study found the similar porous coating. But an 70MP compression prior to the heating achieved a more dense MCO coating than as-deposited MCO coating [121]. The MCO coating by Co-precipitation method reduced the chromium vaporization by a factor of ~40. The smaller particle size may contribute to the better performance of MCO coating by Co-precipitation.

The MCO coating can also be added by thermal-growth approach or RF-sputtering [128]. The thermal growth method included an 800 ℃ for 24 hours in a 2.75% H_2-bal. atmosphere and subsequent oxidation at 800 ℃ in air for 100 hours. The pre-oxidation formed a layer of Cr_2O_3 at the interface between the coating and alloy, which limited the Fe outward diffusion and oxide scale growth [129]. For RF-sputtering method, the sample was firstly sputtered and then oxidized at 800 ℃ in air for 100 hours. Thermal growth approach showed a better result than RF-sputtering. This is due to the finer spinel surface by thermal growth approach.

MCO coating by Magnetron sputtering were also studied [130]. A $MnCoCrO_4$ reaction layer was formed between the oxide scale and the coating. After 1000 hours oxidation in air at 750 ℃, the thickness of oxide scale is about 5 μm, which is a little thick for MCO coated samples. The coating looks still porous even after 1000 hours oxidation at 750 ℃. The reason for this porous coating may have been caused by the missing of condensation steps during the coating process.

Electrodeposition method for MCO coating was developed [131]. Comparing to other method, electrodeposited method can achieve uniform films, easily reproduced and low operation temperature, but it is tricky to find the right solution composition and experimental parameters, especially for Mn deposition [111]. To reduce the complexity of MCO electrodepositing method, a co-deposition method of Co matrix with Mn oxide particles was developed [132]. This electrodeposition can finish in one step and desired dopants are easily added. The thickness of the coating is easily controlled. This study found that the MCO coating by this method had a fair electrical conductivity. The challenge for this method is that Mn concentration is not easily controlled as GNC and

solid mixture methods. The MCO coating only contains 5-10 at% Mn. As-deposited Mn–Co oxide coatings were treated in different atmosphere, including 800 ℃ in air for 10 hours and 5% H_2–95%N_2 at 800 ℃ for 10 hours. The following oxidation in air for 500 hours at 800 ℃ found that the sample pretreated in air is less adherent to alloy than the sample pretreated in 5% H_2–95% N_2. In both samples, Cr diffusion into the Mn-Co-O coating was found. But the one pretreated in 5% H_2–95% N_2 showed a little better due to the lower porosity of the oxide scale.

CHAPTER 2

OXIDATION OF ALLOYS 430 AND 441 WITH DIFFERENT HUMIDITY LEVEL

2.1 Introduction

As described in the first chapter, the effects of humidity to high temperature oxidation are still in dispute. In one aspect, water improves the inward diffusion of OH^- and forms new oxide at the interface between the alloy and oxide scale. This oxide scales have a better adherence than that formed by cation outward diffusion. Better adherence reduces the spallation of oxide scale and thus improves the oxidation resistance, especially for the samples applied in thermal cycle oxidation. In another aspect, water increases the growth rate of the oxide scale and, in some cases can even cause breakaway oxidation. Based on other literature, formation of a protective or non-protective oxide scale is affected by the humidity level. One purpose of the studies presented in this chapter is to find the necessary humidity level for the occurrence of aggravated oxidation behavior.

The hydrogen diffusing through the alloy in a dual oxidation exposure can oxidized to form water at air side. Another work found high concentration of hydrogen dissolved in Fe-10%Cr ferritic samples after steam oxidation at 650℃ [133]. Adding water to air may have the same effects as the dual oxidation. If it is this case, air oxidation with high

humidity can replace the dual oxidation experiment. So, it is necessary to systemically study the effects of different humidity at air side in single and dual oxidation.

2.2 Experimental

The 430 and 441 alloys in this study were each from the same lots and **Table 2.1** lists the specifications of 430 and composition of 441. The effects of humidity on the oxidation behavior of alloys 430 and 441 in air were investigated. **Fig. 2.1** shows the oxidation experiment setup for varying the humidity level by controlling the water bath temperature. Heating tape was wound along the glass tube between the flask and furnace to avoid the condensation of water. The relative humidity levels were measured at the top of the flask by Honeywell® HIH-4602-A/C humidity sensor. The measured relative humidity and temperature were used to calculate absolute concentration of H_2O. In this study, three different water-bath temperatures were applied, including 40, 50 and 60 ℃, which resulted in water volume concentrations of 7 vol%, 10% and 15%, respectively. 430 and 441 plate samples were tested in dry and wet air at 800 ℃ for 200 hours with a flow rate 70ml/min. After 200 hours, the furnace was turned off and the experimental atmosphere was maintained while cooling to room temperature.

Table 2.1 Composition of alloy 430 and 441

Element (wt%)	C	Cr	Mn	Ni	Si	Nb	Ti	Fe
430	≤0.12	16 - 18	≤1.0	≤0.75	≤1.0	---	---	balance
441	0.009	18	0.35	0.3	0.34	0.5	0.22	balance

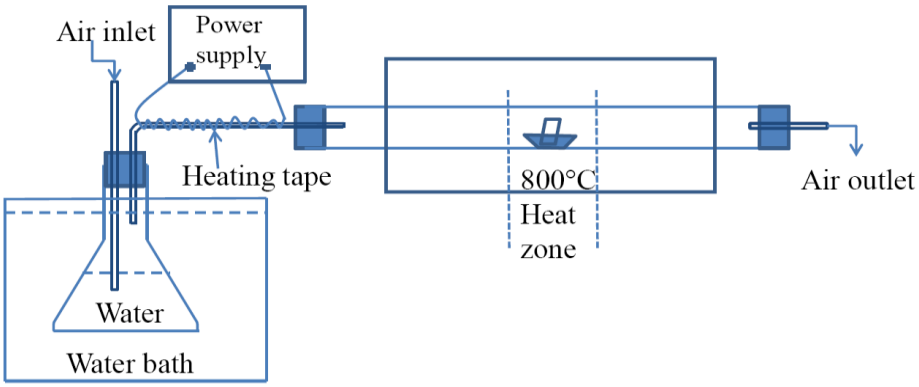

Fig. 2.1 Setup for alloys 430 and 441 oxidation in air with different humidity levels

After the oxidation experiments, the sample weights were measured. Then, the oxide scale microstructure was studied by x-ray diffraction (XRD) and scanning electron microscopy (SEM). After the test, the oxide scale surfaces of samples were analyzed by XRD and a JEOL JSM-7000F SEM. After surface observation, the samples were electroplated with Ni and a cross-section sample was prepared using an Accutom-5 cut-off machine. The samples were epoxy-mounted, polished and characterized using the SEM. The thicknesses of the oxide scales were estimated by measuring 5 thicknesses in micrographs from 10 random positions (i.e. 50 measurements).

2.3 Result and discussion

Fig. 2.2 shows the weight change of 430 and 441 after 200hr oxidation in 70ml/min dry and wet air at 800℃. The weight change for alloy 430 increases at high humidity levels, but alloy 441 does not show this trend. As shown in **Fig. 2.2**, at 7% H_2O the oxidation behaviors of 430 and 441 were similar, but at higher water vapor concentrations, the weight gain for 430 was higher. **Fig. 2.3** shows the surface and cross section microstructures of 430 and 441 after 200 hours oxidation in air with 15% H_2O.

On the surface microstructure of 430 oxide scale, some Fe-rich nodules were found as in **Fig. 2.3a**. Generally, the appearance of Fe-rich nodules revealed more severe oxidation, which is consistent with the weight change results of 430 (**Fig. 2.2**). The cross section microstructure of 430 (**Fig. 2.3b**) shows a relatively smooth oxide scale, which is composed of Cr_2O_3 and surface $(Mn,Cr,Fe)_3O_4$ spinel phase. The cross section microstructure of the 441 oxide scale shows an irregular oxide scale (**Fig. 2.3d**). The surface microstructure of 441 (**Fig. 2.3c**) also showed a ragged surface.

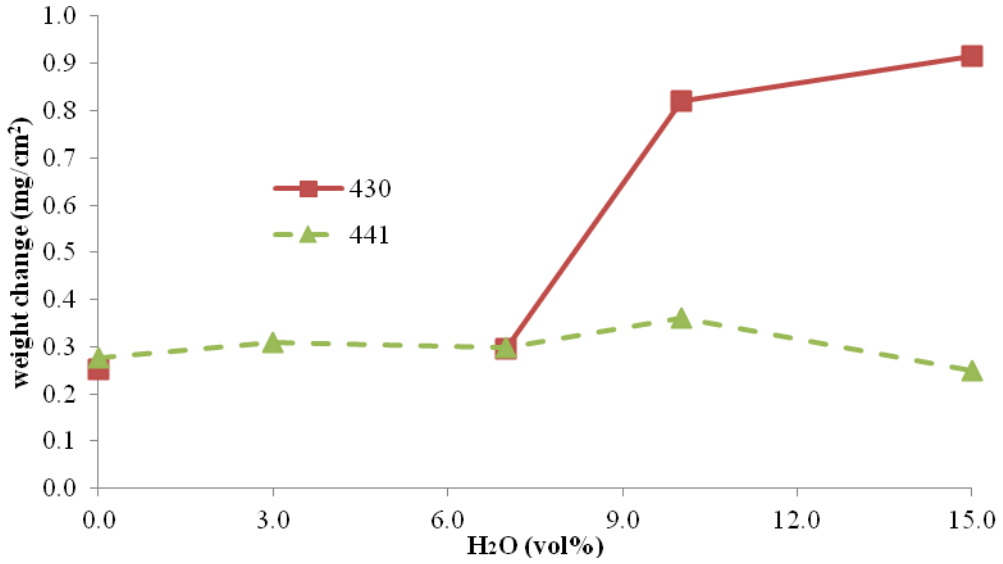

Fig. 2.2 Alloy 430 and 441 weight change after 800 ℃-200hr in 70ml/min air flow with different water concentration.

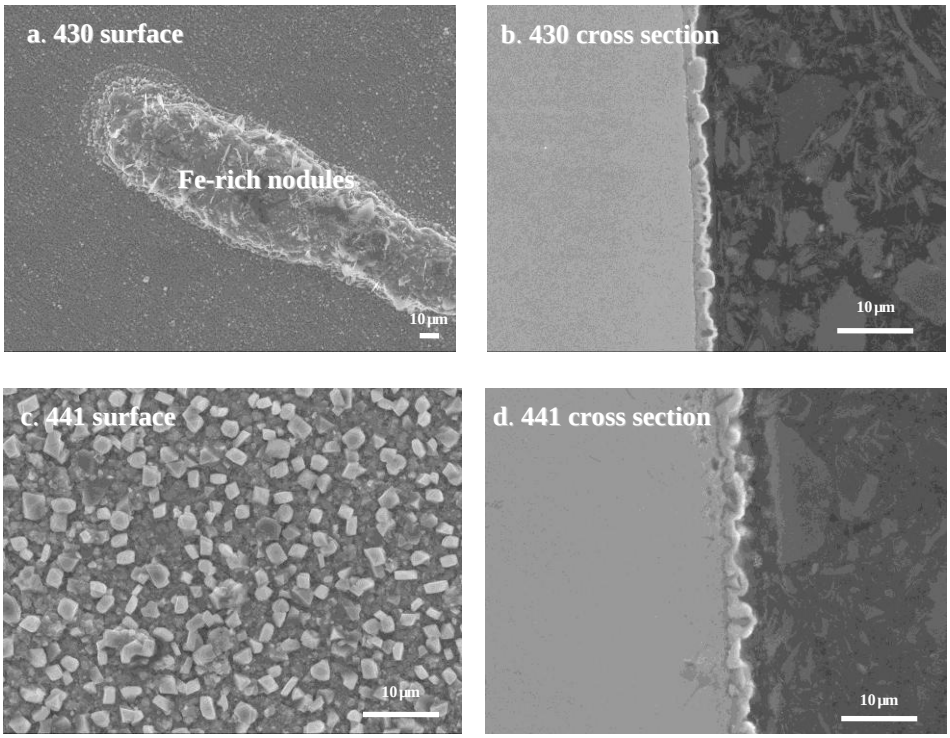

Fig. 2.3 Alloy 430 and 441 surface and cross section oxide scale microstructure after 200 hours oxidation in air with 15% H_2O.

The results of the current work indicate that the presence of water vapor increases the oxidation rate of 430, which is in agreement with other studies [11, 17, 18]. Water can promote the inward growth of oxide scale [11] due to the formation of OH^- ions which diffuse through the oxide scale to form new oxide at the interface between alloy and oxide scale [15]. Generally, the oxide scales formed by inward diffusion show a flat oxide scale and have a better adherence than those formed by cation outward diffusion [11, 15].

There larger weight gain at high humidity levels was not observed for 441. One reason may be that the more severe spallation of 441 oxide scale may result in a lower measured weight gain. Comparing **Fig. 2.3b** and **2.3d**, alloy 441 shows a more irregular oxide scale than alloy 430. The spalling of 441 oxide scale has been attributed to the

weak bond between TiO_2 and Fe_2Nb-type precipitates at the grain boundaries [83]. Current work finds the Fe_2Nb precipitates at alloy grain boundaries as shown in **Fig.2.4a**. Near the alloy surface (**Fig. 2.4b**), a Nb deficient zone at grain boundaries was found and the area at the bottom of the oxide scale had a slightly enhanced Nb and Ti concentration. Secondly, the different grain sizes of 430 and 441 may have contributed to the different oxide scale morphology (**Fig.9b** and **Fig.9d**). . The grain sizes of 430 and 441 are 16 and 50 μm, respectively. Grain boundaries are fast path for Cr or Mn outward diffusion [100]. A study found that the diffusivity of Cr along the grain boundaries is 4-5 orders of magnitude higher than that in Fe lattice [104]. For small grain size, the fast outward diffusion of Cr along grain boundaries may easily supply Cr to make up for the Cr consumed by scale growth and volatilization, which can increase in the presence of with water due to the formation of $CrO_2(OH)_2$ [24, 26, 134]. In some extreme cases, when the Cr supply from the alloy is insufficient, some Cr depletion area may form under the oxide scale, in which case non-protective Fe-rich nodules may form in the oxide scale as discussed above. In the current work, some iron-rich nodules were found on the surface of 430 oxide scale in air-15%H_2O (**Fig. 2.2a**). The formation of these nodules is possibly caused by the depletion of Cr in some areas. In another work, a nanocrystalline coating with same composition was applied on the alloy 304 to increase the grain boundaries for Cr outward diffusion [135].

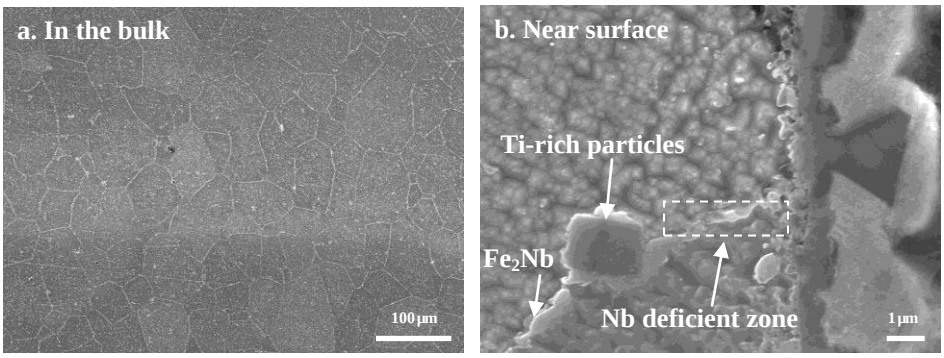

Fig. 2.4 Cross section of 441 after oxidation in air with 15%H_2O

2.4 Conclusions

The presence of water vapor in the air appears to improve the adherence of the oxide scale. 430 showed a higher growth rate with higher humidity level, but the weight change of 441 did not follow this trend. Both spallation of oxide scale and Cr depletion are possible reasons for this difference between 430 and 441. In air-15%H_2O, the different grain size may have contributed to the oxide scale microstructure difference.

CHAPTER 3

DUAL ATMOSPHERE OXIDATION OF ALLOYS 430 AND 441: EFFECT OF GAS FLOW RATE

3.1 Introduction

SOFC is a promising technology for clean energy conversion. In planar SOFCs, interconnects separate adjacent single cells, and as the operation temperature is decreased to 800℃, metallic alloys can be used for interconnects. However, oxidation resistance under the SOFC high temperature environment is one of the critical issues for the application of metallic alloys as the interconnect [2, 4]. In a SOFC, one side of interconnect is exposed to air and the other side is exposed to H_2 or another fuel. Due to the H_2 concentration difference between the two sides, hydrogen may diffuse through the alloy and affect the oxidation behavior of the alloy on the air side. For example, after dual exposure at 800℃ for 300 hours, the Fe concentration at the air-side surface of the oxide scale formed on alloy 430 was higher than that exposed both side to air [41]. In some areas, even Fe_2O_3 nodules were found [41, 42].

This effect of dual atmosphere exposure has been observed on other alloys including 441, which is similar in composition to 430, but contains Nb and Ti. The alloying additions in 441 can prevent the formation of a continuous SiO_2 layer, which dramatically increases the electronic resistance of the SOFC [136]. This makes 441 one of the promising ferritic candidates for use as the interconnect material. However, the oxide

scale formed on the air side of alloy 441 during a dual exposure oxidation test at 800℃ for 300 hours contained a Fe_2O_3 outer layer and was much thicker than the scale formed on a control sample exposed to air [88]. During high temperature oxidation, Nb and Ti can segregate to the grain boundaries [83, 84], which may stabilize the grain boundaries and prevent the grain growth during the high temperature exposure. Spallation of the oxide scale formed on alloy 441 has been attributed to TiO_2 and Fe_2Nb-type precipitates at the grain boundaries[83]. Many other studies find the fast diffusion of alloy elements along grain boundaries during the oxidation of ferritic alloys [43]. In alloys containing Nb, a Laves phase may form at the grain boundaries, which could limit the outward diffusion of alloy elements along the grain boundaries during the oxidation in single atmosphere [78-80]. Hydrogen has a very high diffusivity in Nb [91-93], so in dual atmosphere exposures high hydrogen diffusion along the grain boundaries may contribute to the anomalous growth of the oxide scale on 441. Although some work has been done to study the high temperature oxidation of 430 and 441 in dual atmospheres, the effects of H_2 or air flow rate at the air side have not been reported and are the focus of this chapter.

3.2 Experimental

The 430 and 441 circular disks (33 mm dia) were sectioned from plates (thickness of 1.20 mm for 430 and 1.45 mm for 441) by electrical discharge machining (EDM). For each dual-atmosphere test the circular disk was sealed to the end of an AISI304 stainless tubing (OD: 25.4 mm, ID: 19.3 mm) by Ni-based BNi-2 braze. The braze sealing was performed in a vacuum furnace (at least 1×10^{-3} torr) by heating from room temperature to 1050℃, holding for 30 min, and then cooling to room temperature. **Fig. 3.1** shows the

setup for the dual atmosphere exposures, which were carried out in a quartz tube. One side of the coupon was exposed to wet Ar-5 vol% H_2 (3vol% H_2O) and the other side was exposed to cylinder air (moisture ≤67.0PPM) or wet air (3% H_2O). The wet hydrogen and air were prepared by passing the gas through water bubblers at room temperature. In this work, 5ml/min and 35ml/min Ar-5 vol% H_2 flow rate were applied. Another plate sample was kept in the quartz tube as the control sample. The quartz tube was kept in a tube furnace. Before heating, the system was flushed with the experimental atmosphere for 24 hours. The samples were then heated and held at 800℃ for the required time. **Table 3.1** lists the different dual atmosphere exposure conditions used for studying the effects of H_2 flow rate and humidity at air side. After the dual exposure, the tube furnace was turned off and the experimental atmosphere was maintained while cooling to room temperature. After the test, the coupon was removed by cutting the end of the 304 tubing. The surface of the dual atmosphere and control samples were analyzed by XRD and a JEOL JSM-7000F SEM. After surface observation, the samples were electroplated with Ni and a cross-section sample was prepared using an Accutom-5 cut-off machine. The control and dual-atmosphere samples were epoxy-mounted, polished and characterized using the SEM. The thicknesses of the oxide scales were estimated by measuring 5 thicknesses in micrographs from 10 random positions (i.e. 50 measurements).

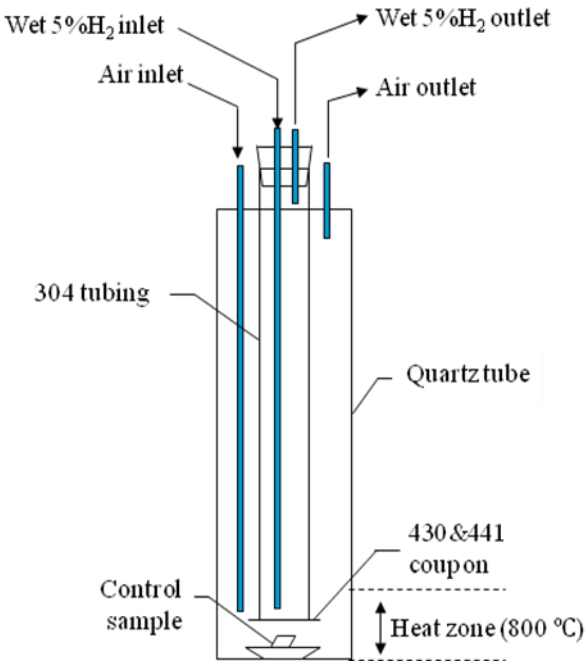

Fig. 3.1 Setup of dual atmosphere exposure.

Table 3.1 Dual oxidation conditions of alloy 430 and 441 at 800 ℃ for 200hrs

		Air side		Wet Ar-5% H_2 side
		Wet /dry	Flow rate	Flow rate
430	#1	Dry	5ml/min	5ml/min
	#2	Dry	5ml/min	35ml/min
441	#3	Dry	5ml/min	5ml/min
	#4	Wet	5 ml/min	5ml/min
	#5	Dry	5ml/min	100hr- 5ml/min→100hr -35ml/min
	#6	Dry	5ml/min	100hr- 35ml/min→100hr- 5ml/min
	#7	Dry	5 ml/min	35 ml/min
	#8	Wet	70 ml/min	35 ml/min

3.3 Results and Discussion

3.3.1 XRD results

The XRD spectra for all different dual atmosphere exposures were similar. As shown in **Fig. 3.2,** the oxide scales formed on the air control and air side all contained Cr_2O_3 and a spinel phase. The small peak at 27.3 ° is possibly the peak of rutile TiO_2, which has been observed to be dispersed on the surface of the oxide scale of 441. SEM analysis shows that the scale consisted of a Cr_2O_3 sublayer and $(Mn,Cr)_3O_4$ spinel phase outer layer. The oxide scale thickness measurement and oxide scale microstructure showed some difference between the samples exposed to different H_2 flow rate.

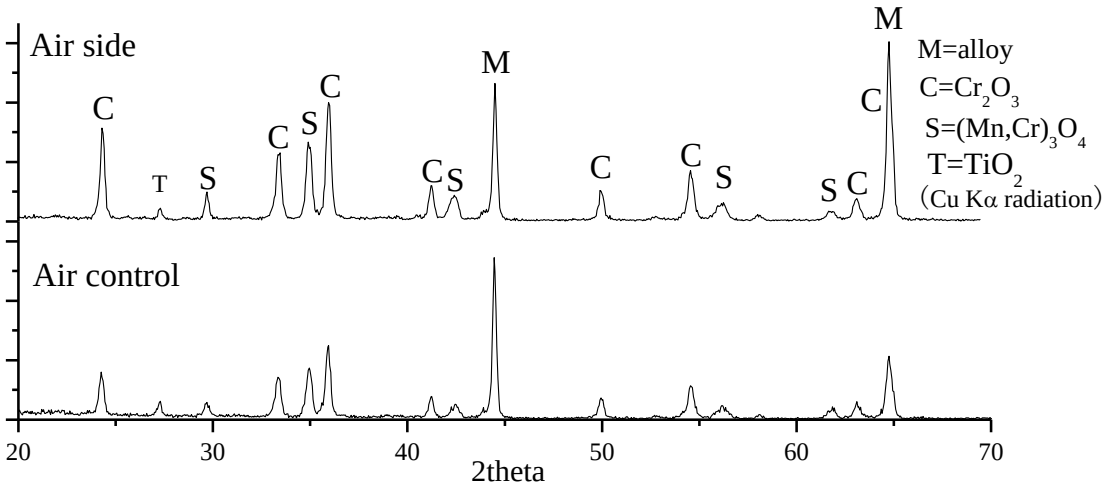

Fig. 3.2 The XRD spectra of alloy 441 (#4) after 200hr dual oxidation.

3.3.2 Oxide scale thickness

Fig. 3.3 shows the thickness measurement result from the SEM cross section observation. The thickness differences are compared by statistic ANOVA analysis with 95% probability. For alloy 430 at both low (#1) and high (#2) flow rates, the scale formed on the air side of the dual atmosphere exposure was thicker than that formed on the control samples. For alloy 441, samples treated with 5ml/min wet Ar-5% H_2 (#3: dry air and #4: wet air) showed similar oxide scale thicknesses at the air side and on air control. However, the oxide scales on the air side of samples treated with high Ar-5%H_2 flow rate (#5-8) were thicker than that at control sample. Within that group of samples, the air side of the sample treated with 200hrs high H_2 flow rate (#7) had a thicker oxide scale than the samples treated with 100hrs high H_2 flow rate (#5-6). Comparing the samples treated with different H_2 flow rate switch (#5 vs. #6), both air control and side showed similar oxide scale thicknesses.

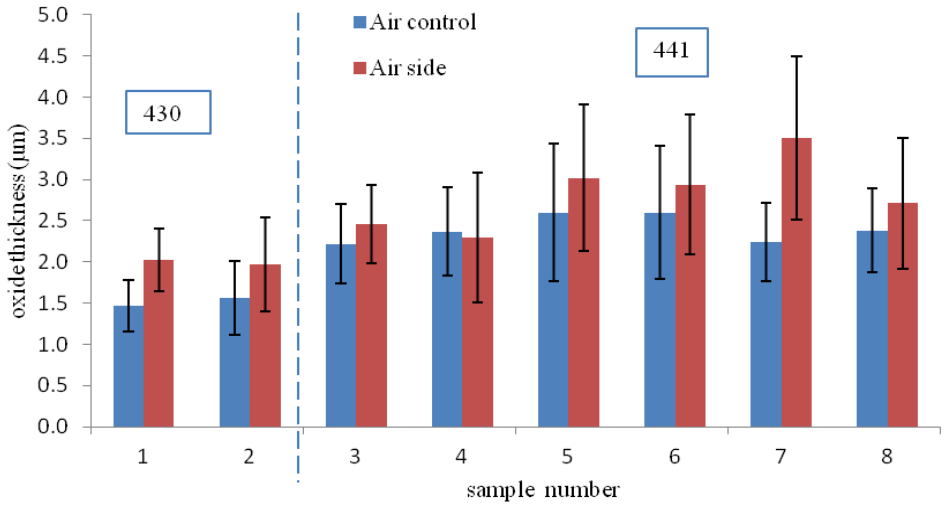

Fig. 3.3 Oxide scale thickness results by SEM cross section measurement. Error bars represent plus/minus standard deviations.

3.3.3 SEM images of oxide scale

Fig. 3.4 shows SEM images of the air side of 430 after the dual oxidation. The oxide scale is composed of surface $(Mn,Cr)_3O_4$ spinel phase and underlying Cr_2O_3. For samples treated with both low and high flow wet Ar-5% H_2 rates, Fe-rich nodules were found only in an area at the surface of the air side as shown in **Fig.3.4**. The difference is that the sample treated with high flow rate (#2) contained more Fe-rich nodules than the sample treated with low flow rate (#1). **Fig. 3.5** shows SEM images of the air control and air side of alloy 441 after a dual atmosphere oxidation (35 ml/min wet 5% H_2 | 70 ml/min wet air). The oxide scale formed on the control sample in 70 ml/min wet air had a similar composition as that formed on the control sample in 5 ml/min dry air. Both scales are composed of a Cr_2O_3 sublayer and a $(Mn,Cr)_3O_4$ spinel phase surface layer. At the air side, localized Fe-rich nodules were found as shown in **Fig. 3.5b**. In **Fig. 3.5d**, EDS elemental linescans show a sharp increase of Ti and Nb concentration at the bottom or surface of the Fe_2O_3 nodule.

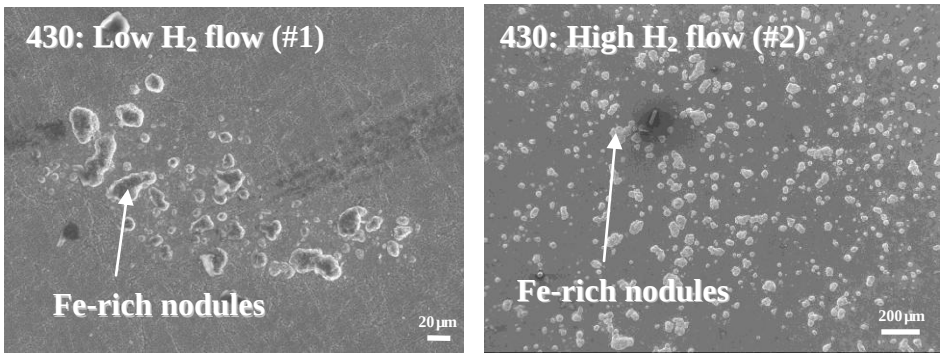

Fig. 3.4 430 air side surface microstructure after 800 ℃-200hr dual oxidation

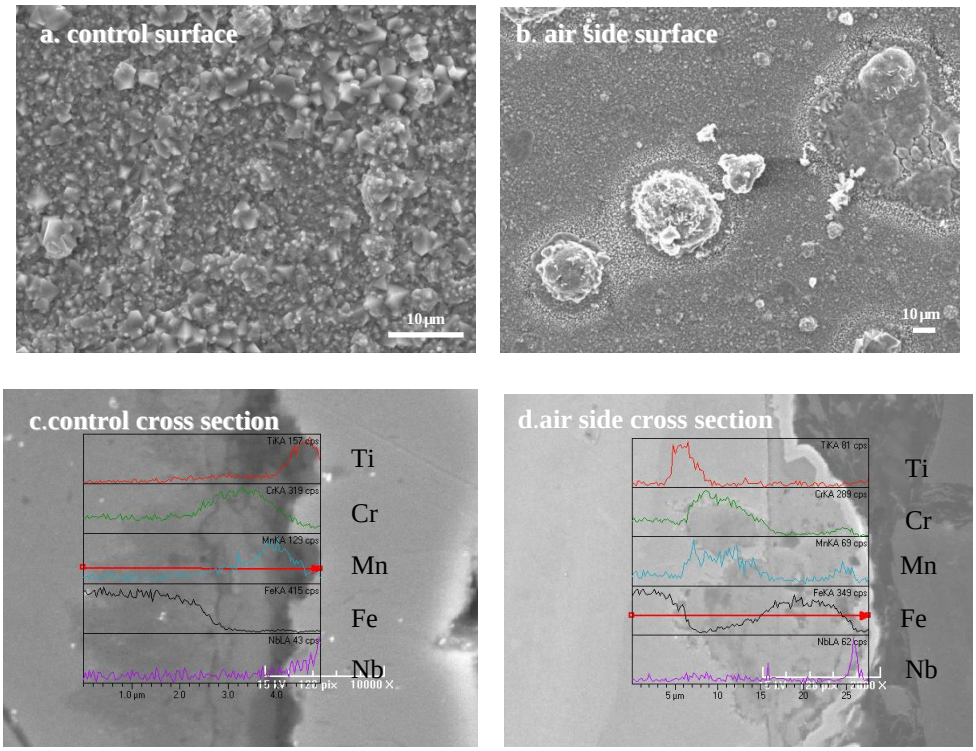

Fig. 3.5 441 SEM images of control and air side after 800℃-200hr dual atmosphere oxidation (#8: 35 ml/min wet 5%H_2 │70 ml/min wet air).

Fig. 3.6 shows an SEM image of the air side of alloy 441 after dual atmosphere oxidation (#5: 35ml/min wet 5% H_2│5ml/min dry air). On the air side, some Fe-rich nodules were found. Near the Fe-rich nodule residuals, there were some white particles, which contained high concentrations of Nb (14 at%) and Ti (18%). These white particles may have been the solid solution of TiO_2 and NbO_2.

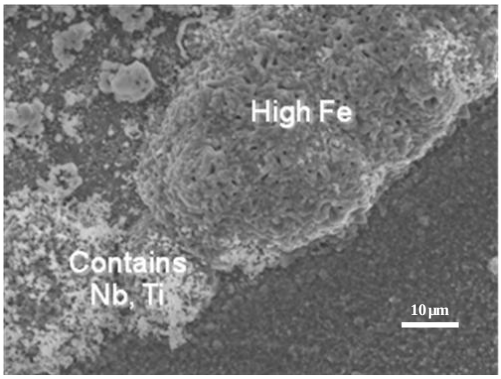

Fig. 3.6 441 SEM surface microstructure images of air side after dual oxidation (#7: 35ml/min wet 5% H_2 │5ml/min dry air).

Based on the oxide scale thickness measurements and the oxide scale microstructure from SEM analysis, the high flow Ar-5%H_2 flow rate (35 ml/min) resulted in more Fe-rich nodules and thicker scales as compared to the lower Ar-5%H_2 flow rate (5 ml/min). The higher flow rate may have supplied more hydrogen to diffuse through the alloy substrate to the air side of the sample exposed to the dual atmosphere. Another study investigated the effects of hydrogen on the oxidation behavior of chromium [96] and suggested that the formation of interstitial protons increased the concentration of metal vacancies in chromia, which increased the transportation of metal and thus facilitated the outward diffusion of Cr in the chromia scale [11, 96]. If these defects also increased the outward diffusion of Cr, Mn, Fe and other alloy elements through the oxide scale, they could increase the thickness of oxide scale and Fe outward diffusion may contribute to the formation of Fe-rich nodules. Another possible mechanism for Fe-rich nodule formation is that hydrogen may diffuse through the alloy and make the air side more acidic surface at some areas, which favors the hematite formation relative to chromia [38]. This would likely occur when the metal is exposed to the atmosphere, which could be in the early stages of oxidation or later if portions of the oxide spall off. Although hematite

may form due to rapid kinetics, if it is contact with the metal, chromium in the alloy would react with the hematite to form chromia. So, as shown in **Fig. 3.5d,** chromia and spinel phase are formed between the Fe-rich nodule and the alloy. In another study of the dual atmosphere corrosion of 441, with high flow rate (70 ml/min wet air │35 ml/min 3%H_2O- 97% H_2), a thick Fe_2O_3 layer was found on the air side of 441 oxide scale [88]. In the current work, only Fe-rich nodules were found, which may be due to the lower H_2 concentration (5%) used in this study.

In some samples, elemental linescans indicated a high concentration of Nb at the surface of Fe_2O_3 nodule. A critical issue in the application of 441 in SOFCs is the interaction between Nb and Ti. Earlier studies found that, during high temperature corrosion of 441, Nb-containing precipitates deposited close to alloy grain boundary and the spallation of oxidation layers occurred mainly between Fe_2Nb and TiO_2 at the grain boundaries [82-84]. In the current work, white precipitates with high concentration of Nb were present (see in **Fig. 3.6)**. The crystal structure of Fe_2Nb is C14 Laves phase, which has been extensively studied as a hydrogen storage material [71, 72]. Hydrogen should easily occupy the interstitial sites of Fe_2Nb and thus have a high solubility in Fe_2Nb.

For dual oxidation experiments in the current work, the oxidation behavior was similar in dry air and air with 3% H_2O. Another study found that high humidity at the air side could cause more severe oxidation at the air side after the dual oxidation [34]. In addition, steam/ air dual oxidation experiments with ferritic alloys have shown that high humidity at the steam side can cause severe oxidation at air side [137]. The difference from the dual oxidation results in current work may have been caused by lower H_2 (5%)

and water (3%) concentration on the air side. Based on current work, at least about 10% water is necessary to see the effects of water to the oxidation of 430 and 441.

3.4 Conclusions

The effects of H_2 flow rate and humidity at the air side of samples exposed to dual atmosphere were investigated. For both alloys 430 and 441, the high hydrogen flow rate appears to lead to localized Fe-rich nodules and accelerate growth of oxide scale at the air side. In the current dual atmosphere experiments, water vapor does not significantly affect the oxide scale growth rate of the control sample due to the low water vapor concentration.

CHAPTER 4

EFFECTS OF ALLOY GRAIN BOUNDARIES ON THE DUAL ATMOSPHERE OXIDATION BEHAVIOR OF ALLOYS 430 AND 441

4.1 Introduction

Alloy grain boundaries may have a great influence on the oxidation behavior of 430 and 441 [80, 83]. However, systemic studies on the effect of alloy grain boundaries on oxidation, especially dual-atmosphere oxidation, have not been reported. There is still some confusion about the details of the oxidation mechanism in SOFC environment. In previous chapter, no obvious alloy grain boundaries diffusion was observed for alloy 430. The small grain sizes of 430 make it difficult to observe the oxidation difference between the grain boundaries and bulk. Thus, 430 with large grains are necessary to compare the difference between grain boundaries and grain. For 441, ridges composed of spinel phase were found at the surface microstructure observation and the size of the ridge circles was similar as the grain size of 441. However, the grain sizes are not large enough to observe if the Fe prefers to diffuse along the grain boundaries to form the Fe_2O_3 nodules. Thus, systemic studies of the alloy grain boundaries are necessary for understanding the oxidation mechanism in SOFC environment, especially for dual oxidation condition. For studying the effects of grain boundaries to the interconnect oxidation in SOFC, it is necessary to study the grain size growth of 430 and 441 by annealing.

4.2 Experimental

4.2.1 Annealing of alloys 430 and 441

The 430 and 441 alloys in this study were each from the same lots and **Table 2.1** lists the compositions of these two alloys. Both alloys were cut into 12mm×10mm rectangular plates for annealing in Brew® vacuum furnace. Three different annealing temperatures were selected, including 1000, 1100 and 1200℃, for 1, 2, 4, 6 and 8 hours. After the annealing, the samples were cut by an Accutom-5 cut-off machine. The cross section near the center of the samples was selected as the observation area. The cut samples were epoxy-mounted, polished, and etched by aqua regia. After etching, the grain sizes were counted by optical microscopy and SEM images. For each sample, four cross-section areas were randomly selected to calculate the grain size. In each area, 20 lines were draw through the area to count the numbers of grain. When the line is across the grain, it was counted as 1. When the line is tangent to the grain or across half of the grain, it was count as 0.5.

4.2.2 Dual atmosphere oxidation of annealed 430 and 441

Circular disks (33 mm dia) were sectioned from plates (thickness of 1.20 mm for 430 and 1.45 mm for 441) by electrical discharge machining (EDM). After the cutting, the disk samples were rolled to 1.00mm and then annealed to achieve large grain sizes. The annealing was performed in Brew® vacuum furnace (1×10^{-5} torr). The annealing temperature and time were determined based on the previous annealing experiment. The grain size should be at least 50 μm. After the annealing, the samples were polished by an

Al_2O_3 suspension solution up to 0.05μm for a smooth and clean surface. For each dual-atmosphere test, the circular disk was sealed to the end of a 304 stainless tubing (OD: 25.4 mm, ID: 19.3 mm) by Ni-based BNi-2 braze. The braze sealing was performed in a Brew® vacuum furnace (1×10^{-5} torr) by heating from room temperature to 1050℃, holding for 30 min, and then cooling to room temperature.

The dual atmosphere oxidation experiments of annealed 430 and 441 use the same setup as **Fig. 3.1.** One side of the coupon was exposed to 35ml/min wet Ar-5 vol% H_2 and the other side was exposed to 5ml/min dry cylinder air. Two other plate samples (as-received and annealed samples) were kept in the quartz tube as the control samples. The quartz tube was kept in a tube furnace. Before heating, the system was flushed with the experimental atmosphere for 24 hours. The 430 and 441 samples were then heated and held at 800℃ for 100, 200 and 400 hours. After the dual atmosphere oxidation, the tube furnace was turned off and the experimental atmosphere was maintained while cooling to room temperature. After the test, the samples coupon was removed by cutting the end of the 304 tubing. The surface of the dual atmosphere and control samples were analyzed by Broker® D8 powder X-ray diffraction (XRD) and a JEOL JSM-7000F scanning electron microscope (SEM). The average composition of each sample's surface was estimated by measuring 5 random areas at 200X magnification. If the oxide scale surface show a clear morphology difference between grain and grain boundaries, the compositions of grain and grain boundaries were compared by measuring 5 points at 5 random areas (i.e., 25 points each). After surface observation, the samples were electroplated with Ni and a cross-section sample was prepared using an Accutom-5 cut-off machine. The control and dual samples were epoxy-mounted, polished and

characterized using the SEM. The thicknesses of oxide scales were estimated by measuring the thickness at 10 random positions and 5 measurements in each area (total: 50 measurements for each sample). Then the samples were etched by aqua regia to observe the oxide scale difference between the grain boundaries and bulk area.

4.3 Results and discussion

4.3.1 Annealing of alloys 430 and 441

Fig. 4.1 shows grain sizes of alloys 430 and 441 after annealing after 1000, 1100 and 1200 ℃. **Fig. 4.2** demonstrates the typical microstructure of 430 and 441 alloys before and after the annealing at 1100 ℃. For alloys 430 and 441, the grain size after 1000 ℃ annealing is similar to that of the as-received alloys. Annealing at 1000 ℃ does not cause a significant grain growth. For samples annealed at 1100 ℃ for less than 6 hours, the grain sizes of annealed samples are approximately doubled comparing to that of as-received samples. As shown in **Fig. 4.1,** 430 and 441 after 6 hours annealing at 1100 ℃ show**s** a larger standard deviation than those annealed for 1, 2 and 4 hours at 1100 ℃. In **Fig. 4.2c,** some large grains were formed near the surface of the samples in 430 after 1100 ℃-6 hours annealing. After 1100 ℃-8 hours annealing, very large grains were formed in alloy 430 (**Fig. 4.2d**). As shown in **Fig.4.2g** and **4.2h**, 441 did not have same large grain size as formed in f 430 after 6 and 8 hours annealing at 1100 ℃. The Fe_2Nb phase at alloy grain boundaries may have limited the alloy grain growth. After 1200 ℃ annealing, both 430 and 441 had very large grain size. The grain size of 430 and 441 are approximately 1000 μm and 210 μm, respectively. When the annealing is at

1100℃ for over 6 hours or at 1200℃, the alloy grain grow rapidly. For SEM observation of the Fe-rich nodules' distribution, the grain size should be over 50μm. Based on the alloy grain size data, 1100℃-8hour was selected as the annealing parameters to study the effects of grain boundaries.

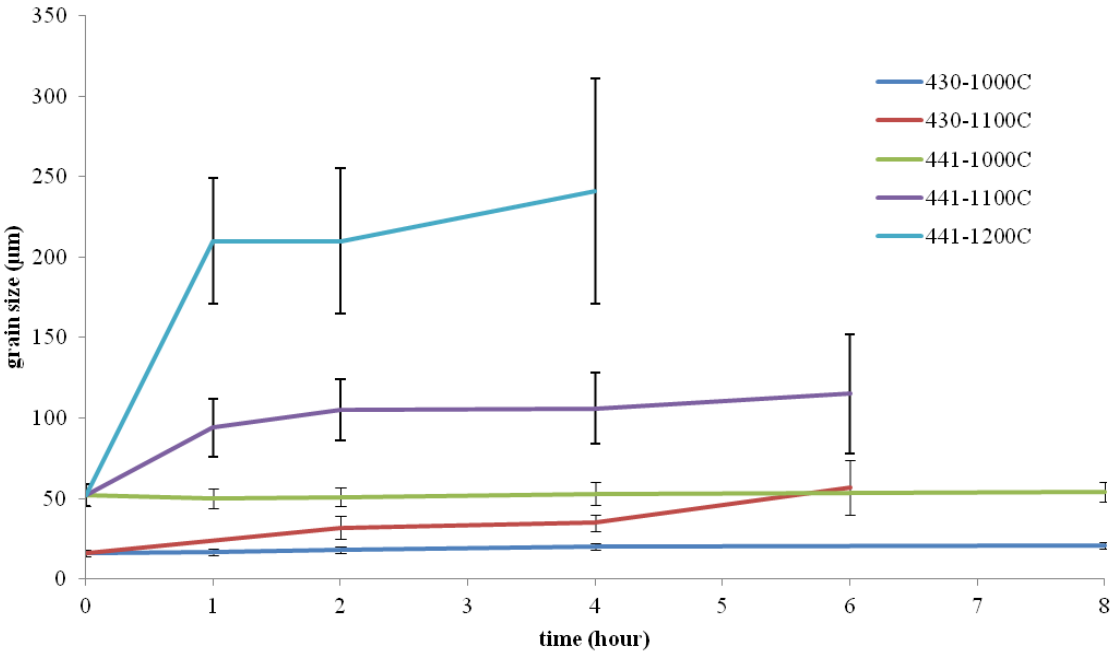

Fig. 4.1 Grain sizes with standard deviation of 430 and 441 after annealing

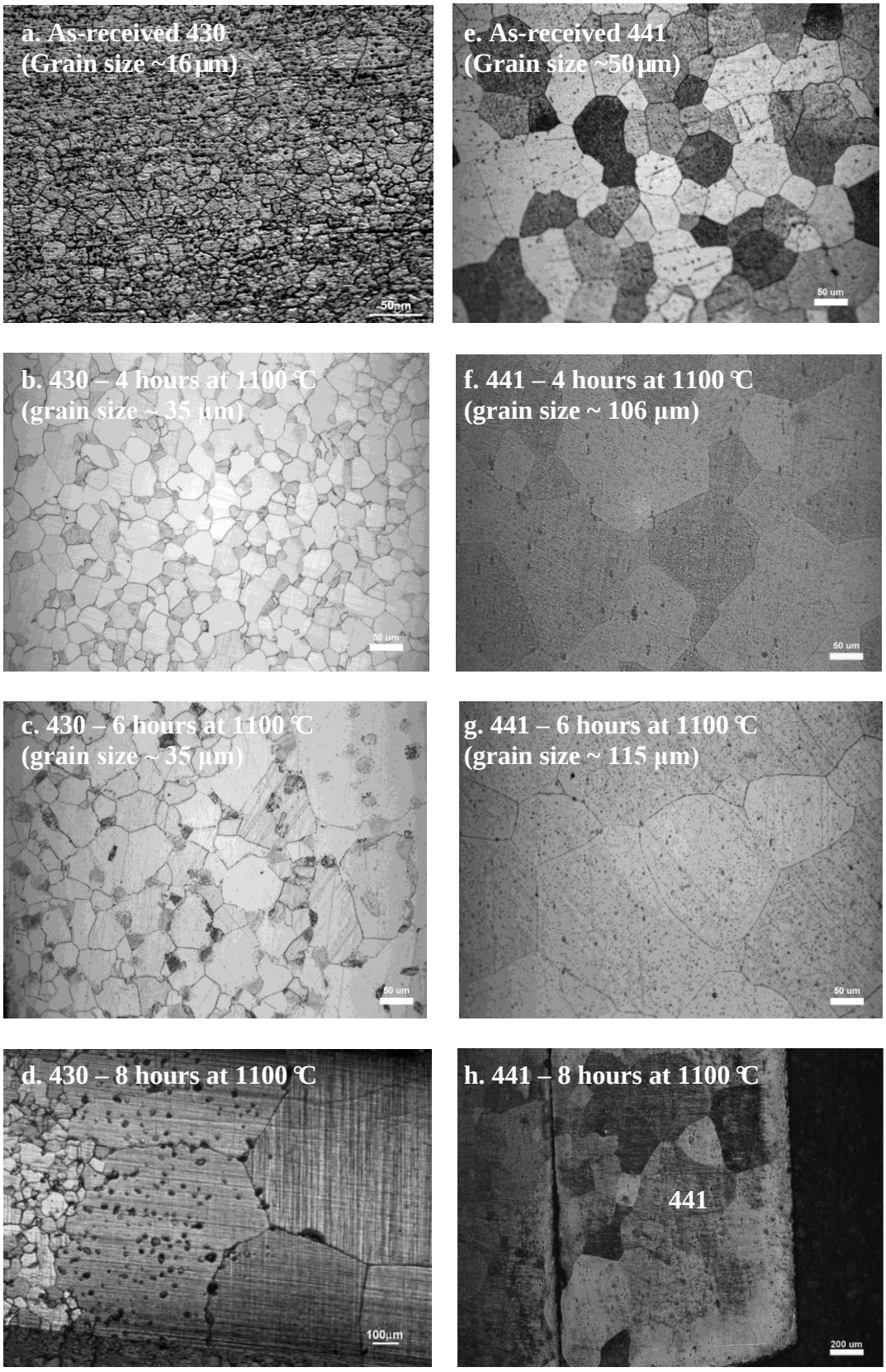

Fig. 4.2 Microstructure of alloys 430 and 441after 4, 6, and 8 hrs at 1100 ℃

Fig. 4.3 shows the alloy grain sizes of 430 and 441 for dual oxidation. The grain sizes of 430 dual samples for 100, 200 and 400 hours are similar and approximately 50 μm. **Fig. 4.4** shows the typical grain sizes for control and dual samples of 430 and 441. As shown in **Fig. 4.4a**, 430 control samples have very large grains, which is similar as the previous annealing results. The grain size difference between the control and dual samples of 430 may have been caused by different samples size. The size of control sample is 10×14 mm^2, which is same as that in previous annealing experiment. The size of dual sample is circular disk with a diameter of 33mm, which is larger than the control samples. The grain size observation area is close to the center of the samples. Previous annealing experiment also found that the grains grow larger at the edge area than that at the center area. The control and dual samples of 441 showed similar grain size in most samples. The grain sizes of 441 are more scattered than that of 430. The larger grain size of 441 is possible reason for this more scattered grain size.

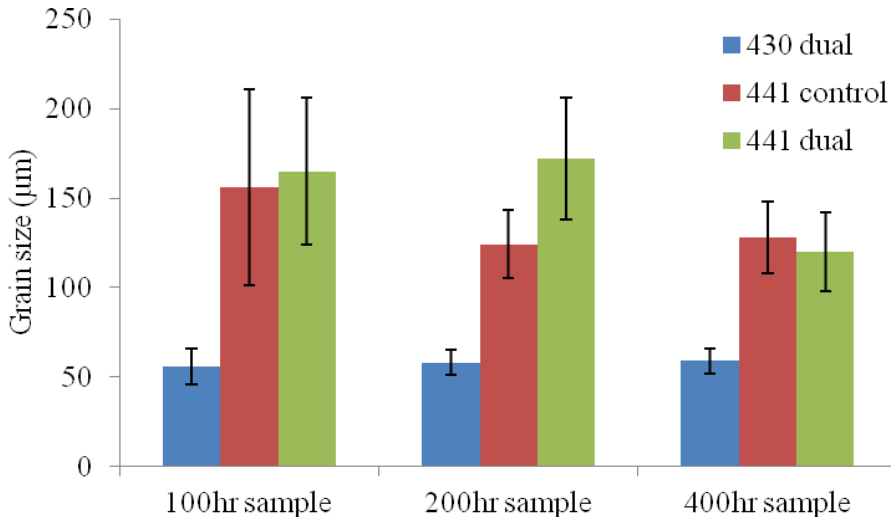

Fig. 4.3 Grain sizes of 1100℃-8hours annealing 430 and 441 for dual atmosphere oxidation experiment. Error bars represent standard deviation.

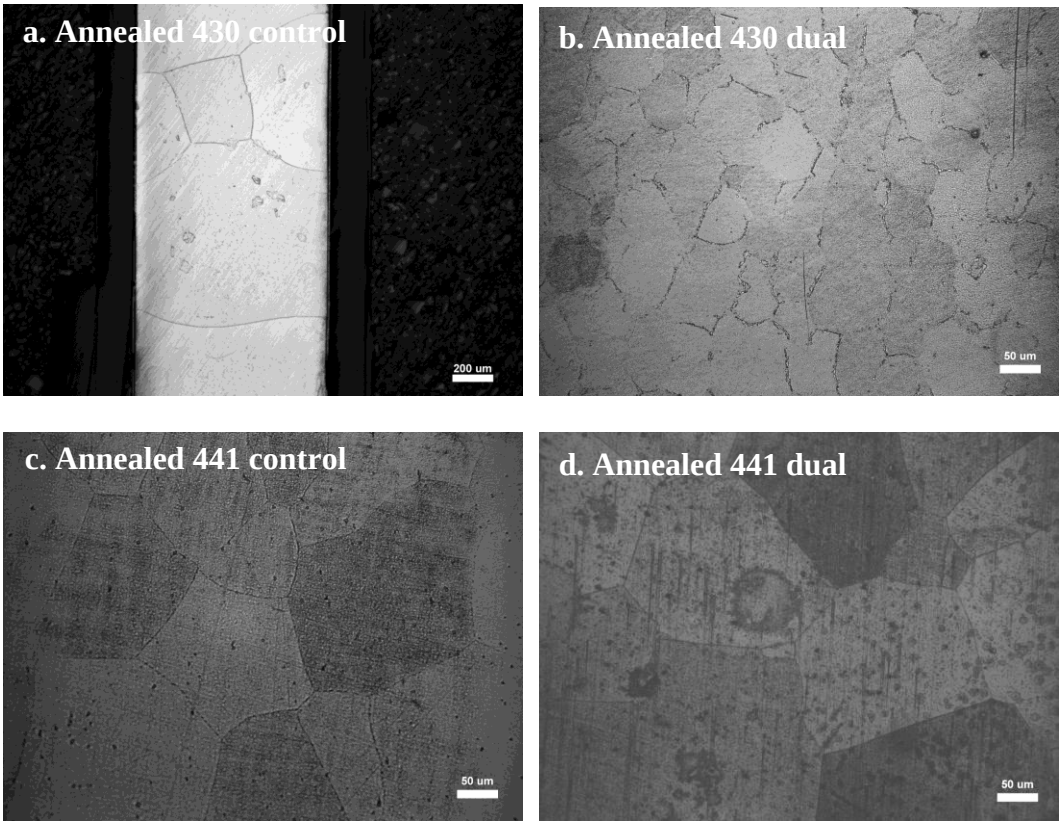

Fig. 4.4 Microstructure of alloys 430 and 441 for dual oxidation test

4.3.2 Control samples

Fig. 4.5 shows the weight gains of annealed and as-received control samples. For alloy 430, the weight gains of annealed and as-received samples are similar after 100 and 200 hours oxidation, but after 400 hours oxidation, the weight gain of as-received 430 is higher than that of annealed 430. For 441, the weight gains for the as-received samples are higher than those of annealed samples after 200 and 400 hours oxidation. As shown in **Fig. 4.6,** the surface microstructure of annealed 430 control sample after 400 hours oxidation indicates that spallation of the oxide scale occurred. The lower weight gain for the annealed samples is likely due to spallation of oxide scale.

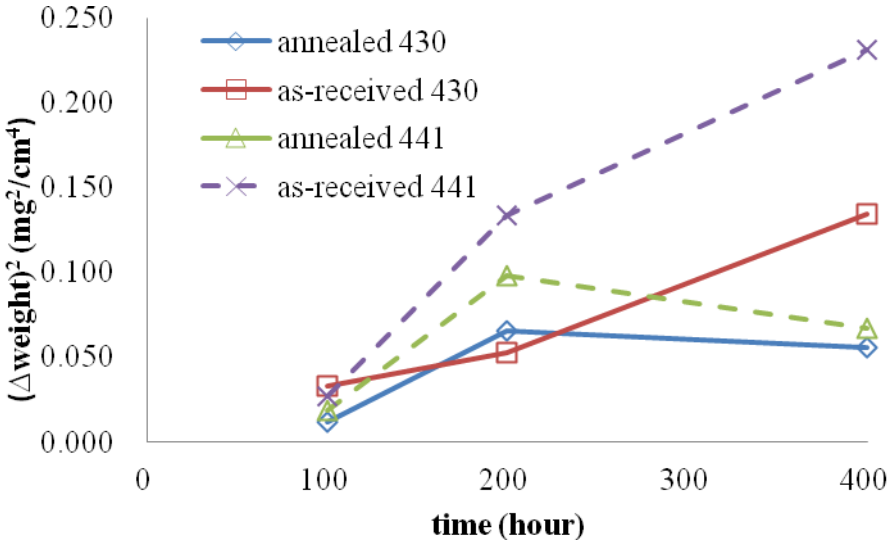

Fig. 4.5 Weight gains of annealed and as-received control sample

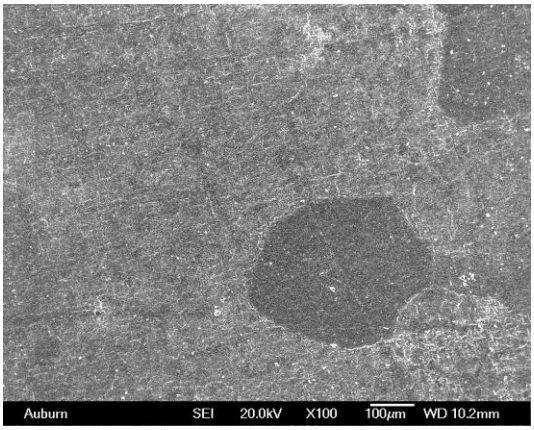

Fig. 4.6 Surface microstructure of annealed 430 control sample after 400 hours oxidation

Fig. 4.7 shows the cross section microstructure of annealed 441 control samples after 400 hours oxidation. **Fig. 4.7a** shows the microstructure in the center area of the cross section. Continuous Fe_2Nb particles were formed at the alloy grain boundaries area. As shown in **Fig. 4.7b**, thicker oxide scale is formed near the alloy grain boundaries. The

EDS results indicate that the white precipitate at the grain boundary contains Nb and is thus likely Fe_2Nb. Near the alloy surface, a Nb deficient zone at grain boundaries was found and the area at the bottom of the oxide scale had an enhanced Nb and Ti concentration. The spalling of 441 oxide scale has been mainly attributed to the weak bond between TiO_2 and Fe_2Nb-type precipitates at the grain boundaries[83], which may explain the more severe spallation for alloy 441 as compared to 430.

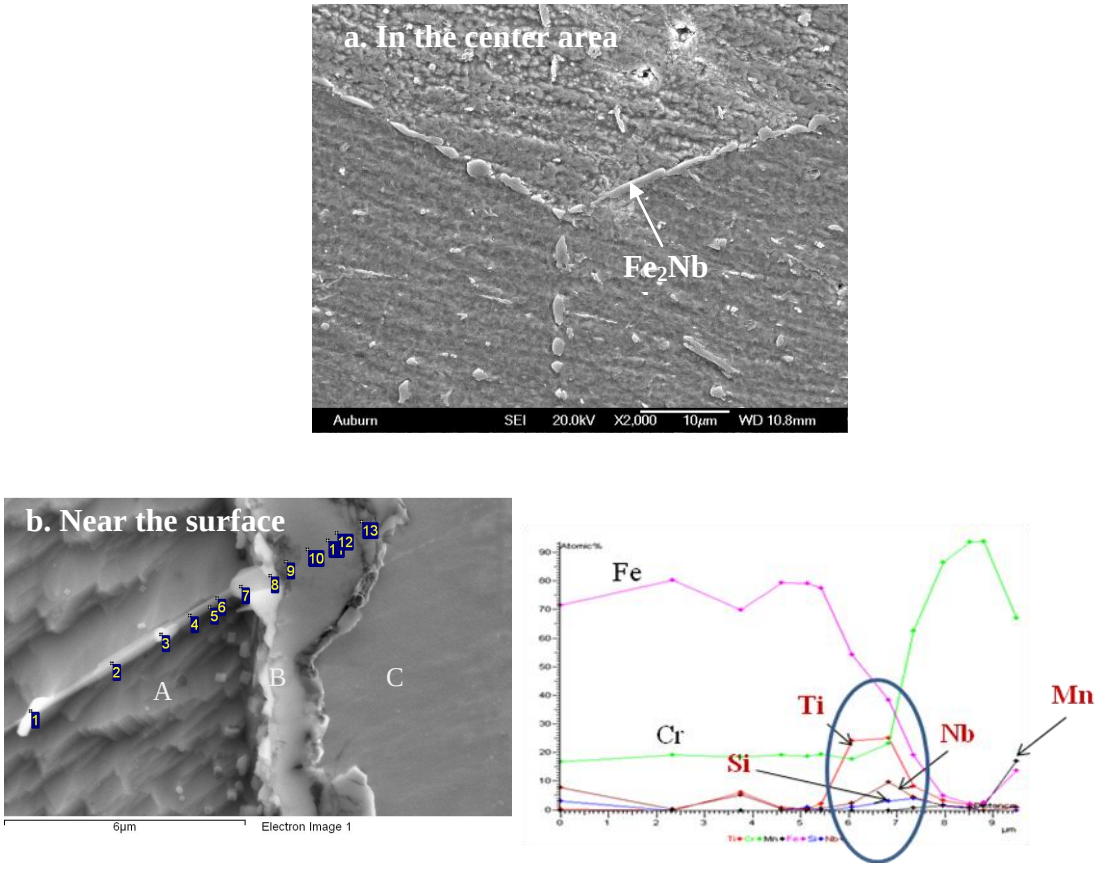

Fig. 4.7 Cross section microstructure and EDS results of annealed 441 control after 400 hours oxidation (A: alloy substrate; B: Oxide scale; C: Ni coating; etched by aqua regia).

4.3.3 Dual atmosphere oxidation results

Oxide scale thickness

Fig. 4.8 summarizes the oxide scale thickness of 430 and 441 dual atmosphere oxidation experiment for studying the effects of grain boundaries. Comparing **Fig. 4.8** with **Fig. 4.5**, the thickness data by SEM measurement shows a similar trend as the weight gain results of control samples. Except of the 430 samples after 800℃ for 200 hours, the as-received control samples have a thicker oxide scale than that of annealed control samples. Both as-received and annealed 441 control samples show a thicker oxide scale than that of 430 samples. The air side of annealed dual samples shows thicker oxide scale than that of annealed control samples. For annealed 430 dual samples, the oxide scale thickness data has a very large deviation. SEM observation found that large amounts of Fe-rich nodules were formed on the surface of annealed 430 dual samples. The Fe-rich oxide scale is very thick - close to 10μm. Some thickness data were taken from the Fe-rich oxide scale area, which make the thickness data more scattered.

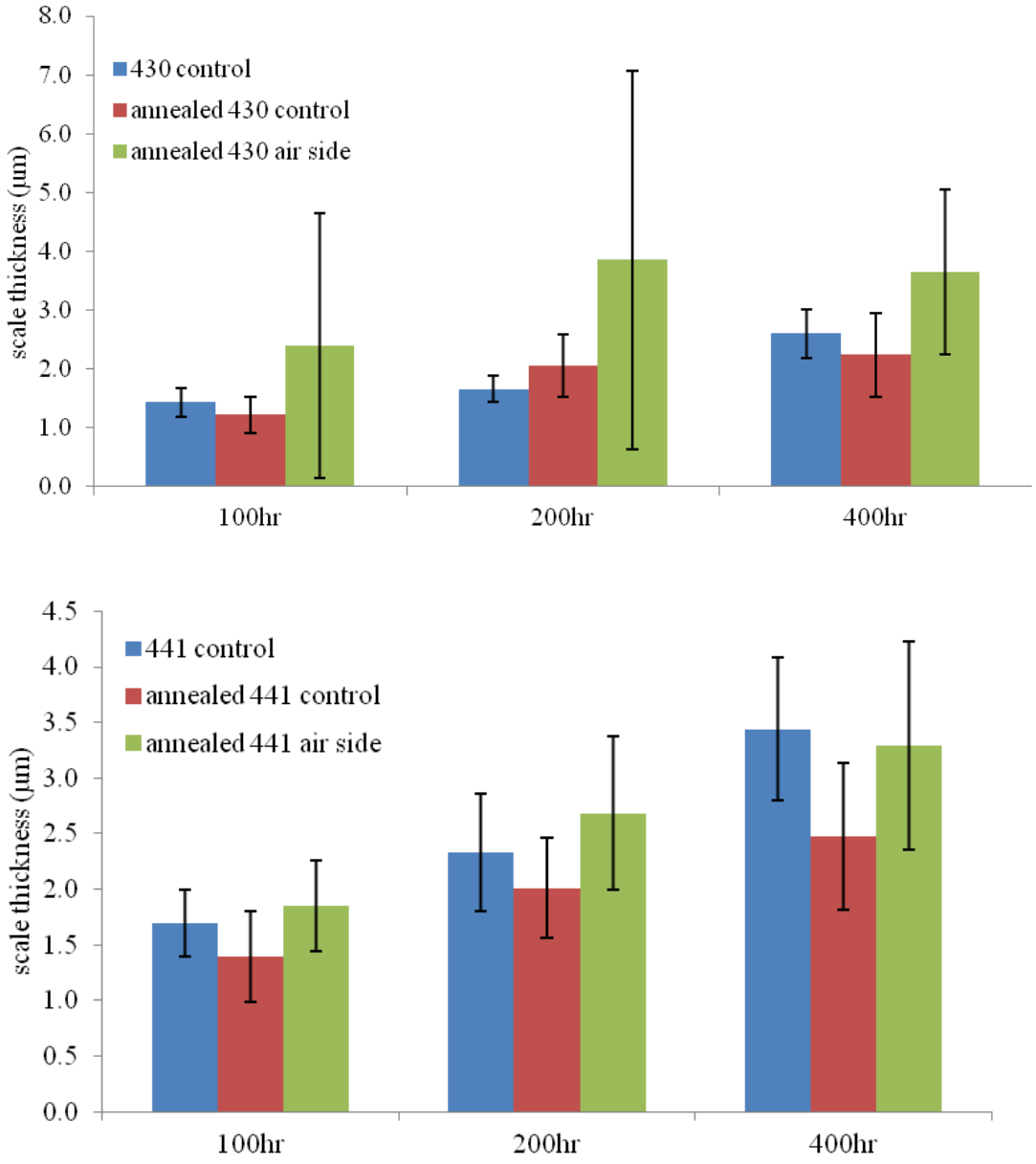

Fig. 4.8 Oxide scale thickness results of 1100℃-8hour annealed 430 and 441 after dual atmosphere oxidation as determined by SEM measurements. Error bars represent standard deviation.

Alloy 430

The XRD patterns for as-received 430 control samples, annealed 430 control samples and annealed 430 on the air side are different. **Fig. 4.9** shows the XRD patterns of alloy 430 after 100 hours dual oxidation. The XRD patterns of 200 and 400 hours dual samples are similar. The oxide scales of the as-received 430 control and annealed 430 control samples contain Cr_2O_3 and $(Mn,Cr)_3O_4$ spinel phase. For annealed 430 control samples, the peaks of alloy are not present, which may be due to the large alloy grain size of annealed 430 control samples. For the air side of annealed 430 dual samples, Fe_2O_3 or $(Fe,Cr)_2O_3$ peaks were found next to the peaks of Cr_2O_3 as shown in **Fig. 4.9**. The positions of the Fe_2O_3 or $(Fe,Cr)_2O_3$ (JCPD #: 34-0412) peaks are almost at the same position.

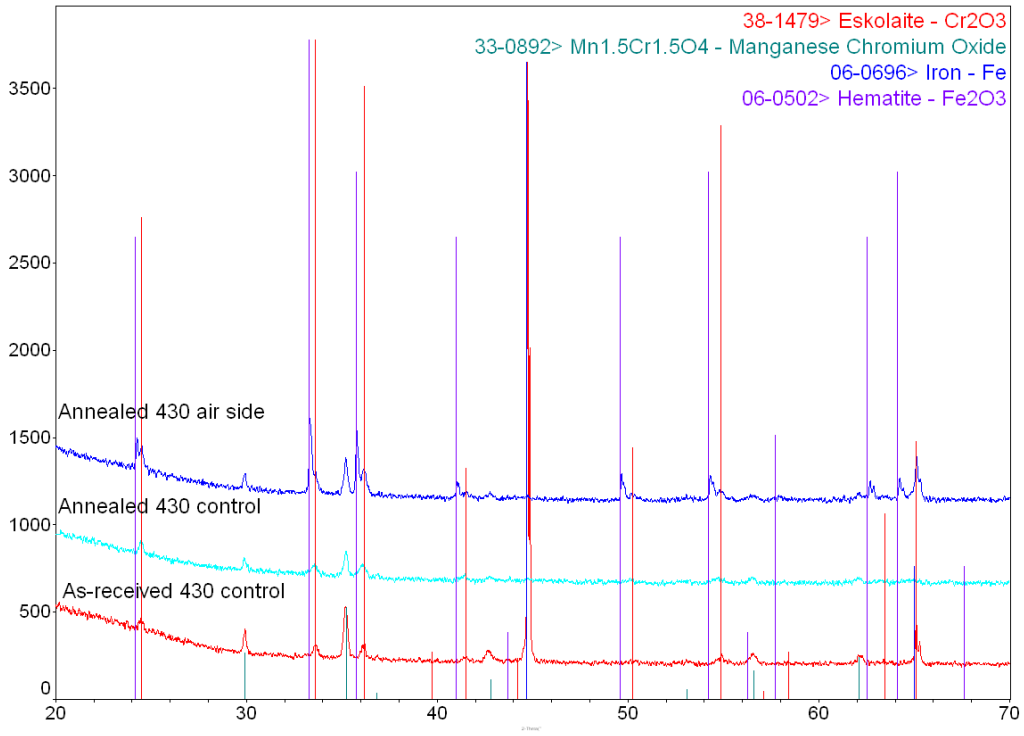

Fig. 4.9 The XRD patterns of annealed 430 after 100 hours dual oxidation.

Fig. 4.10 shows the surface and cross section microstructure of the air side of alloy 430 after 100, 200 and 400 hours dual atmosphere oxidation. After 100 and 200 hours dual atmosphere oxidation, some iron-rich nodules are scattered about the surface of oxide scale. The distribution of Fe-rich nodules shown in **Fig. 4.10b** corresponds to the alloy grain boundaries. After 400 hour dual oxidation (**Fig. 4.10c**), the surface of oxide scale show large nodules of Fe-rich, Cr-rich or spinel phases. Cross section images of the nodules are shown in **Fig. 4.10d-f. Fig. 4.11** shows the EDS scanning results of annealed 430 oxide scale at air side after 100, 200 and 400 hours dual oxidation. Similarly as previous as-received 430 oxidation results, silicon peaks were found at the interface between the oxide scale and the alloy. SiO_2 was formed at this interface, which would increase the electrical resistance dramatically. After 400 hours dual oxidation, annealed 430 air side shows a thinner Cr_2O_3 layer between the Fe-rich nodule and alloy substrate than that after 100 and 200 hours dual oxidation. Comparing the EDS results of annealed and as-received 430 dual oxidation results, the difference is that chromia phase is formed between the Fe-rich nodule and the alloy. In the dual atmosphere oxidation experiment of as-received 430, chromia and spinel phase are formed between the Fe-rich nodule and the alloy. The difference between these two groups of samples is the alloy grain size. The annealed 430 samples have larger alloy grain size and less alloy grain boundaries are available as the fast diffusion path for Mn. The large grain size may have contributed to the absence of spinel phase under the Fe-rich nodules.

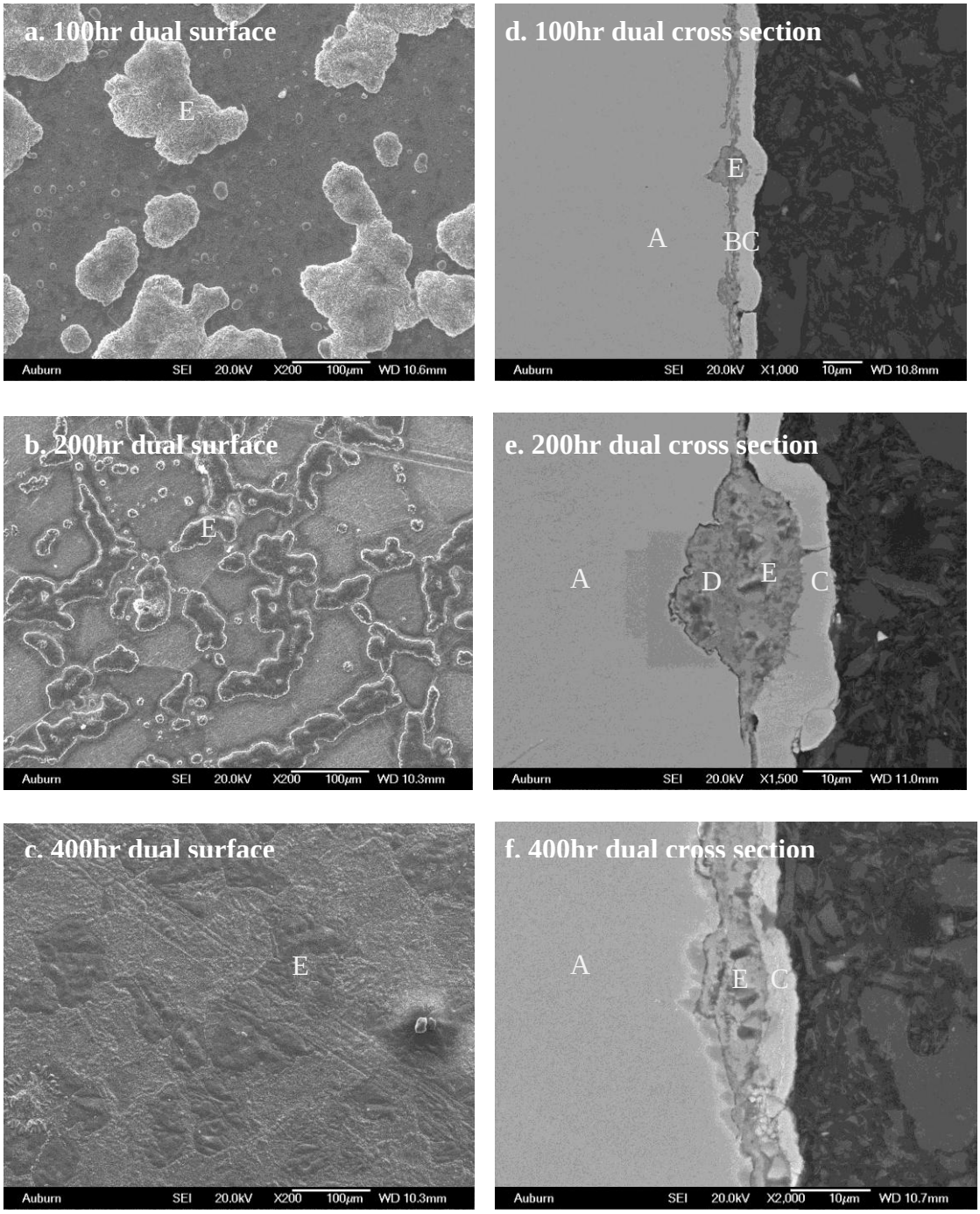

Fig. 4.10 Alloy 430 surface and cross section microstructures after 100, 200 and 400 hr dual oxidation. (A: alloy substrate, B: Oxide scale, C: Ni coating, D: Cr_2O_3, E: Fe-rich nodules.)

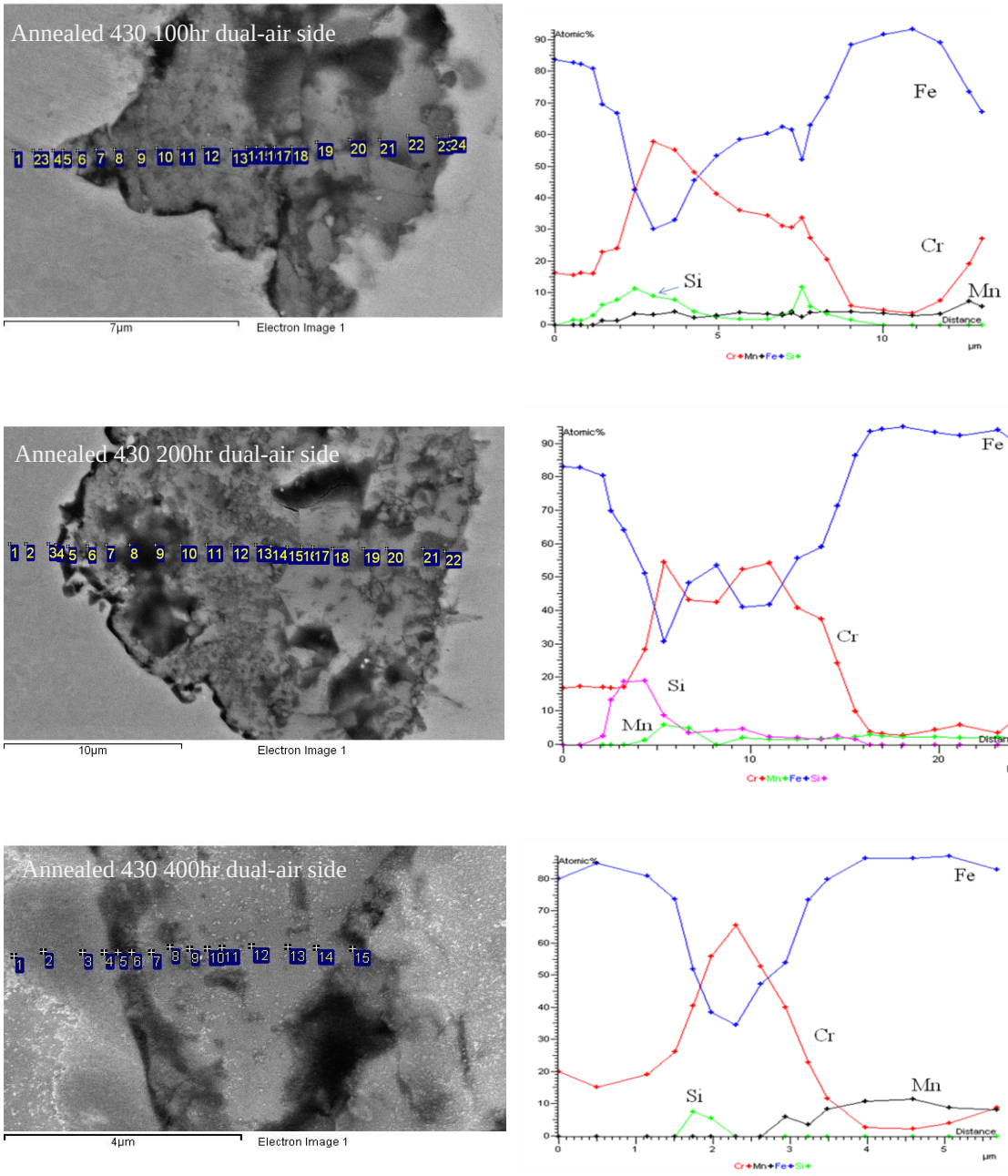

Fig. 4.11 EDS scanning results of annealed 430 air side after 100, 200 and 400 hours dual oxidation.

As shown in **Fig. 4.12**, the oxide scales at air side have a different morphology among 100, 200 and 400 hours dual atmosphere treated samples. After the 100 hours dual atmosphere oxidation, the nodules have needle-shape morphology and contain about 90 at% Fe. After 200 and 400 hours dual oxidations, the Fe concentration in the nodules decreases to 70% and a layer of a spinel phase is formed at the rim of Fe-rich nodules. After 200 hours dual oxidation, some needle-shape residuals (~90% Fe) were found on the top of ball-shape Fe-rich nodules (~70% Fe). On the surface of annealed 430 after 400 hours dual oxidation, no needle-shape Fe-rich nodules were found. **Fig. 4.13** demonstrates more details of annealed 430 air side after 400 hours dual oxidation. After 400 hours dual oxidation, the oxide scale formed three different morphologies, including Fe-rich area, spinel ridges and Cr-rich area. Based on phase diagram of Fe_2O_3 and Cr_2O_3, The Fe-rich area in the 400-hour treated 430 should composed of a $(Fe,Cr)_2O_3$, a mixed solid solution of Fe_2O_3 and Cr_2O_3. It appear that the alloy grain is completely covered by Fe-rich or Cr-rich nodules and a spinel ridge is formed at the alloy grain boundaries area.

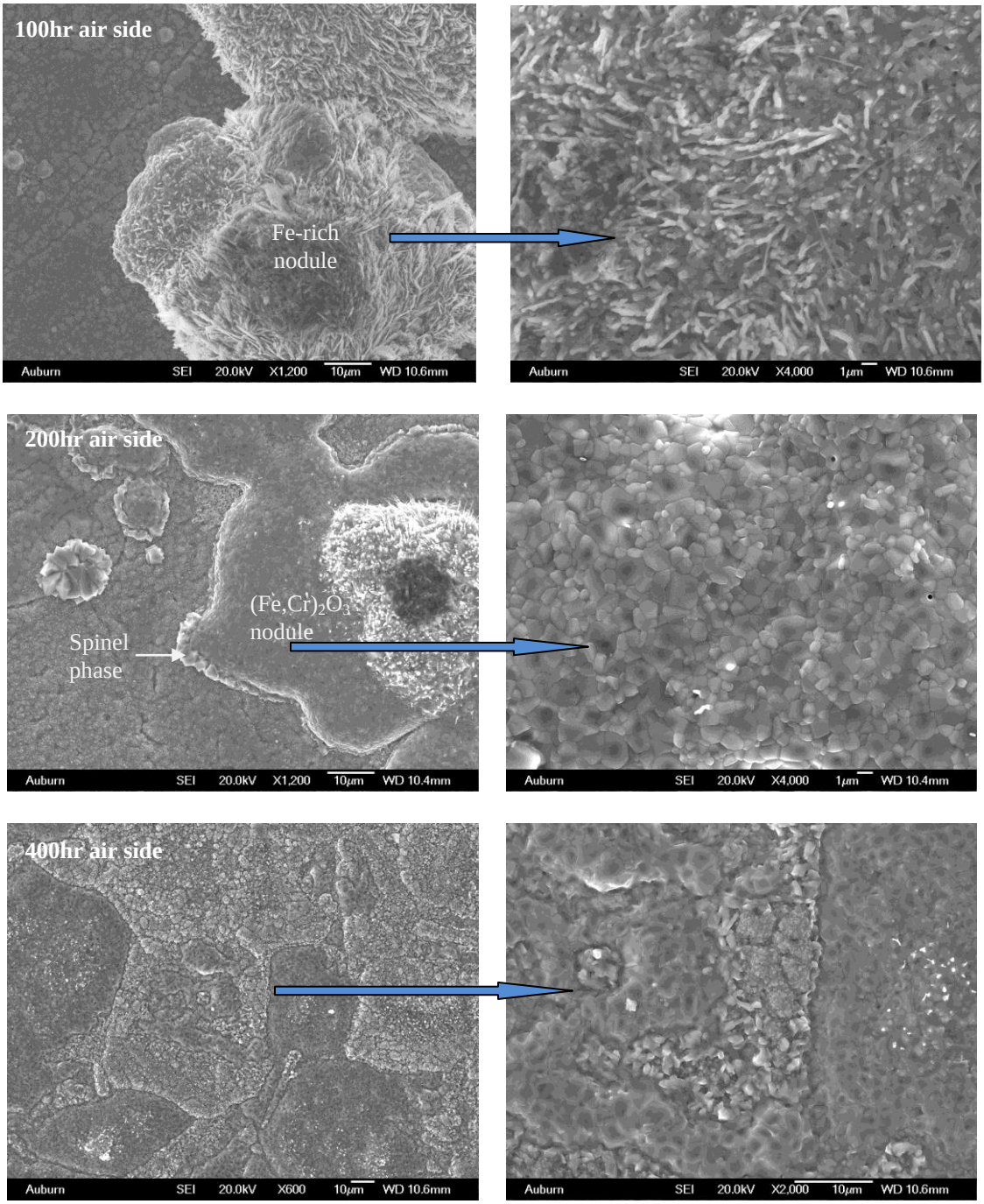

Fig. 4.12 Surface Fe-rich nodules of annealed 430 dual samples after 100, 200 and 400 hours dual oxidation.

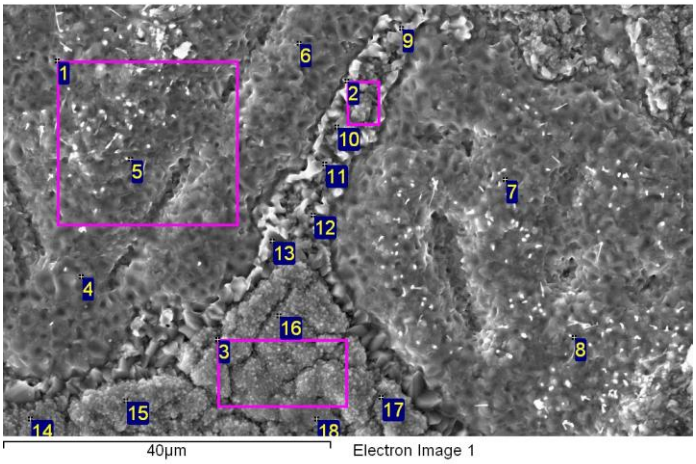

$(Fe,Cr)_2O_3$ area (at%)	Cr	Mn	Fe	Between Fe-rich nodules	Cr	Mn	Fe	Cr-rich area	Cr	Mn	Fe
#1	18.5	6.6	75.0	#2	46.8	31.	21.8	#3	78.3	14.9	6.8
#4	17.1	7.9	75.0	#9	31.6	22.3	46.1	#14	70.8	17.2	12.0
#5	19.2	8.0	72.8	#10	45.3	35.7	19.0	#15	65.2	20.4	14.5
#6	14.0	7.4	78.6	#11	42.7	35.2	22.1	#16	73.0	16.3	10.7
#7	16.8	7.2	76.0	#12	45.6	29.1	21.9	#17	58.7	28.1	13.2
#8	15.7	5.8	78.5	#13	39.1	35.0	26.0	#18	77.4	14.9	7.8

Fig. 4.13 Annealed 430 air side surface images for EDS analysis after 800℃-400hr dual oxidation

Fig. 4.14 shows the microstructure of annealed 430 air side after 100, 200 and 400 hours dual atmosphere oxidation. For samples after 100 and 200 hours dual atmosphere oxidation, the Fe-rich nodules are formed near the alloy grain boundaries area. For 100-hour treated samples, needle–shape particles were found at the top of the oxide scale. For 200-hour treated sample, Si-rich particles were found at the interface between the alloy and oxide scale. The SEM and EDS analysis showed that Fe-rich or Cr-rich nodules covered the whole alloy grains, which is consistent with the surface oxide scale microstructure observation.

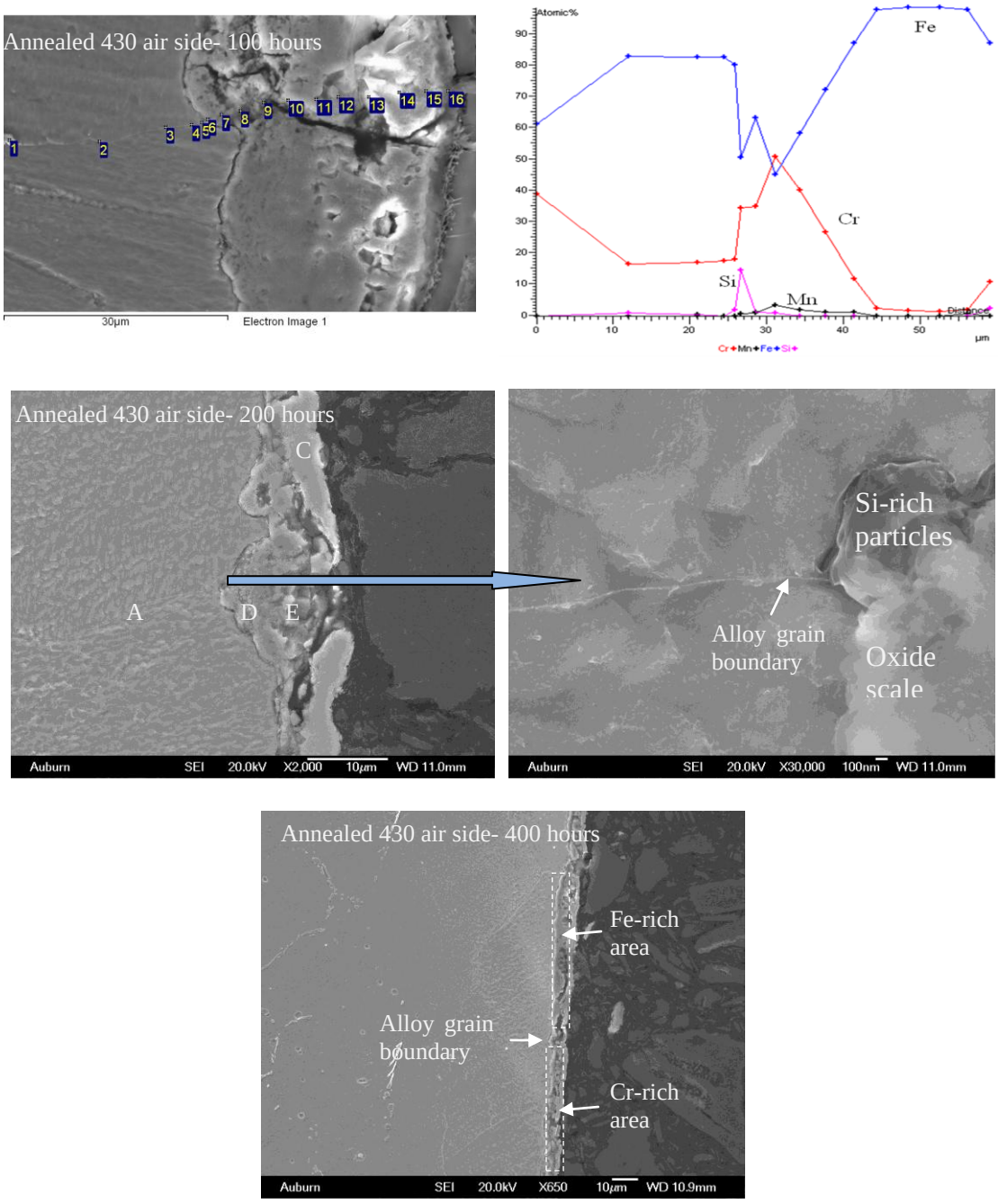

Fig. 4.14 Interface microstructure between Fe-rich nodule and alloy after 200hr dual (etched by aqua regia; A: alloy substrate, C: Ni coating, D: Cr_2O_3, E: Fe-rich nodules.)

Alloy 441

Fig. 4.15 shows the XRD patterns of alloy 441 after 100 hours dual oxidation. The XRD patterns of 200 hours and 400 hours dual samples are similar. The oxide scales are all composed of the surface $(Mn,Cr)_3O_4$ spinel and underlying Cr_2O_3. **Fig. 4.16** shows the surface and cross section microstructure of the air side of 441 after 100, 200 and 400 hours dual oxidation at 800 ℃. On the surface microstructure, ridge-shape areas were found on oxide scales. The area surrounded by the ridge has similar size as the alloy grain, which suggests that the ridges are formed by the fast outward diffusion of alloy element along the alloy grain boundaries. Only after 200 and 400 hours dual oxidations, 441 showed Fe-rich nodules in some areas as shown in **Fig. 4.16b**. As shown in **Fig. 4.16b**, the Fe-rich nodule is very close to the ridge. The formation of Fe-rich nodules is possibly related with the alloy grain boundaries. In **Fig. 4.16f**, the white areas in the alloy contained higher Nb concentration, which is Fe_2Nb Laves phase at the alloy grain boundaries. The oxide scale is a little thicker near this Nb-rich area.

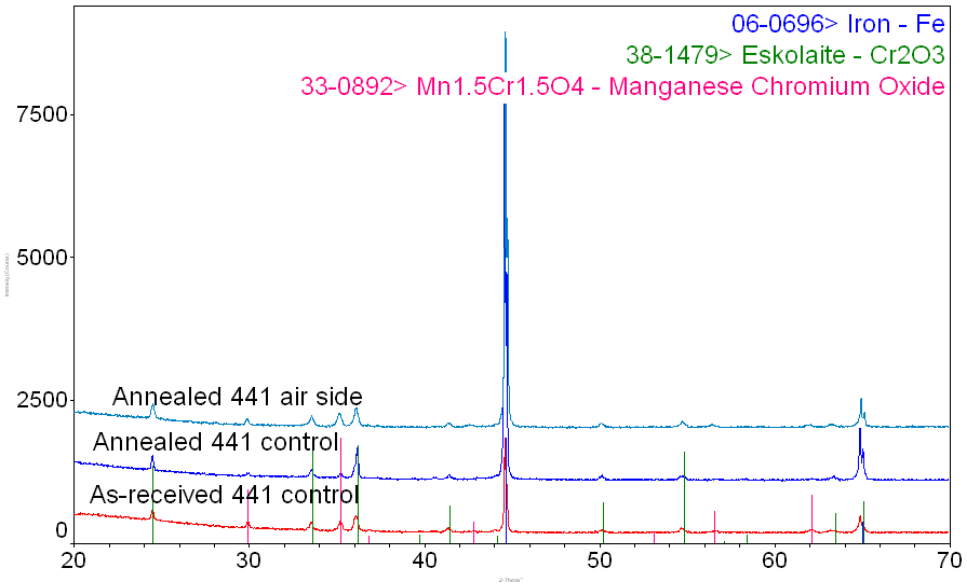

Fig. 4.15 The XRD patterns of annealed 441 after 100 hours dual oxidation.

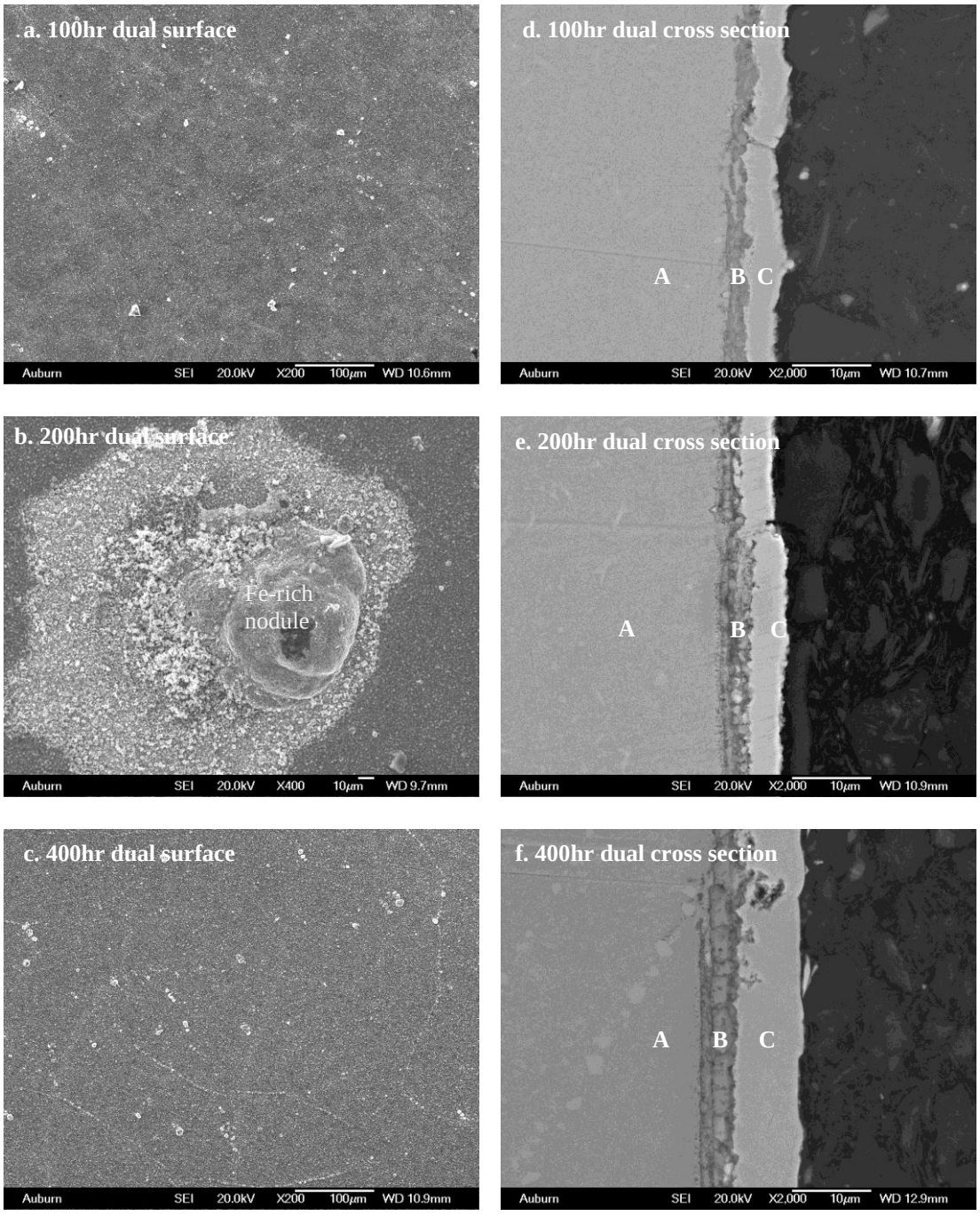

Fig. 4.16 Alloy 441 surface and cross section microstructures after 100, 200 and 400 hours dual oxidation. (A: alloy substrate; B: Oxide scale; C: Ni coating.)

Grain boundaries vs. grain oxidation

As shown in **Fig. 4.16,** ridge-shape areas were found on oxide scales surface. The size surrounded by the ridge is similar as the alloy grain size. The ridges are possibly related with the oxide scale growth along alloy grain boundaries. For annealed 441 samples after 400 hours dual oxidation**,** the compositions of ridge and none-ridge area were compared by measuring the composition at 25 randomly selected locations. **Fig. 4.17** shows the atomic ratio of Mn by (Cr+Mn+Fe). EDS results indicated that Ti-rich particles were discretely distributed at the ridge. To remove the influence of Ti, the ratio between Mn and (Cr+Mn+Fe) was selected to compare the Mn concentration difference. For all three samples, the ridge area has a higher Mn ratio than that of none-ridge area. Comparing the three samples, annealed 441 control samples showed the lowest Mn ratio among the three samples. The Mn ratio of annealed 441 air side is only a little lower than that of the as-received 441 control sample.

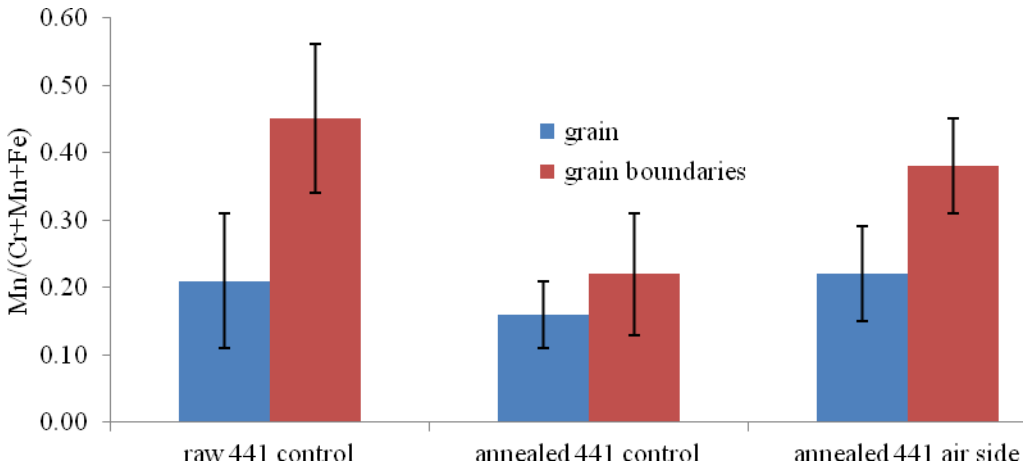

Fig. 4.17 Mn ratio to Cr+Mn+Fe of 441 after 400 hours dual oxidation at alloy grain and grain boundaries

Fig. 4.18 shows the average Mn concentration of 430 and 441 after 400 hours dual oxidation. Similar to results in **Fig. 4.17**, annealed 430 and 441 control samples have the lowest Mn concentration. Annealed 430 and 441 air sides showed a little higher Mn concentration than that of the annealed control samples. As-received control samples have the highest Mn concentrations and the smallest grain size.

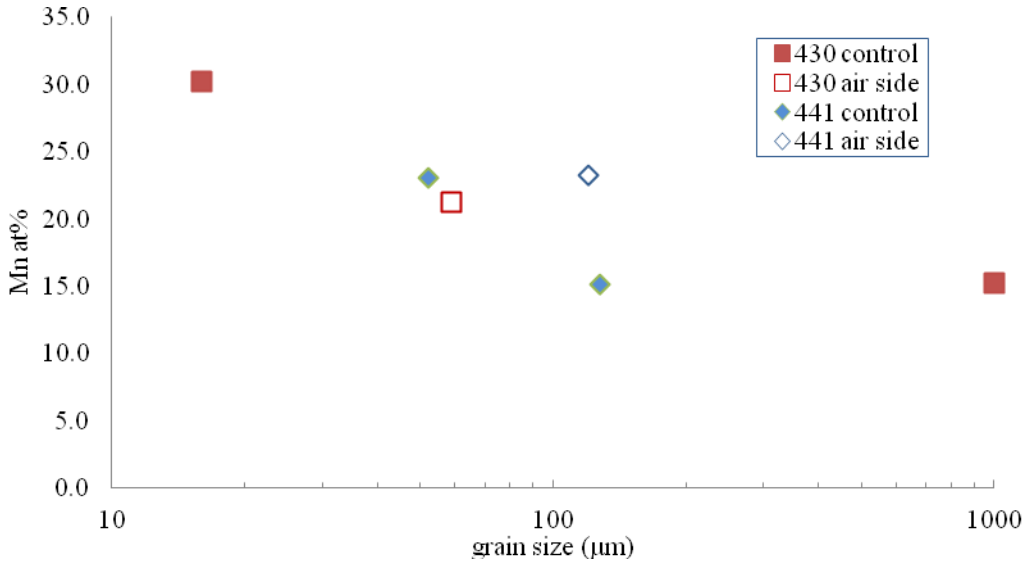

Fig. 4.18 Average Mn concentration of alloy 430 and 441 oxide scale after 400 hours dual oxidation. (Control samples with large grain are annealed control samples.)

The EDS measurements in **Fig. 4.17** show that the Mn concentration was higher at the alloy grain boundaries region. The average Mn concentration of the as-received control samples (**Fig. 4.18**) is higher than those of annealed control samples. The as-received 430 control sample (16 µm) has a higher surface average Mn concentration than the as-received 441 control sample (50 µm). All these results demonstrate that alloy grain boundaries are the fast path for Mn outward diffusion. The lower Mn concentration of annealed control samples is possibly due to the large alloy grain size. The large alloy grain size increases distance for Mn to diffuse from the grain to the grain boundaries and

also reduces the amount of fast grain-boundaries quantities for Mn diffusion to form Mn-rich spinel phase.

In another work, laves phase formed along the grain boundaries of Laves-phase ferritic alloy in an H_2-H_2O atmosphere was considered to limit the outward diffusion of Fe, Cr and Mn along alloy grain boundaries [80]. In current work, a continuous Fe_2Nb Laves phase also formed at the 441 alloy grain boundaries (**Fig. 4.7a**) and a ridge-shape with a high concentration of Mn was formed on the oxide scale (**Fig. 4.16 a-c**). It was not occurred in current test that Fe_2Nb Laves phase limits Mn outward diffusion. This inconsistency may have been caused by the different oxidation atmosphere. Current test atmosphere is air or wet air and cations outward diffusion controls the growth of oxide scale. The oxide scale growth in H_2-H_2O atmosphere is dominated by oxygen inward diffusion. Based on EDS measurement in **Fig. 4.17**, high Mn concentration were found at the ridge-shape oxide scale. Even if there is large amount of Laves phase along 441 alloy grain boundaries, Mn can still diffuse along alloy grain boundaries.

Comparing the EDS results shown in **Fig. 4.17** and **4.18**, the annealed air side has a higher Mn concentration than the annealed control samples for both alloys 430 and 441. SEM observation of 430 dual oxidation experiments also found that the Fe-rich nodules tend to form close to the alloy grain boundary area (**Fig. 4.10** and **4.14**). Annealed 441 dual oxidation experiments shows similar trend (**Fig. 4.16b**). Hydrogen has been found to diffuse preferentially along alloy grain boundaries in ferritic alloys [109]. Hydrogen diffusion along the alloy grain boundaries may increase the concentration of metal vacancies at grain boundaries area and thus facilitate the outward diffusion of alloy elements in the chromia scale [11, 96]. Fe outward diffusion may contribute to the

formation of Fe-rich nodules. Another possible mechanism for Fe-rich nodule formation is that hydrogen may diffuse through the alloy grain boundaries and make the air side more acidic at grain boundaries area, which favors the hematite formation relative to chromia [38]. This would likely occur when the metal is exposed, which could be in the early stages of oxidation or later if portions of the oxide spall off. Although hematite may form due to rapid kinetics, if it is contact with the metal, chromium in the alloy would react with the hematite to form chromia. So, as shown in **Fig. 4.10** and **4.11,** chromia is formed between the Fe-rich nodule and the alloy. For samples with small alloy grain size, Mn may diffuse to the interface between the Fe-rich nodule and alloy substrate. In this case, chromia and spinel phases are formed between the nodule and the alloy (**Fig. 3.5d**).

Based on the SEM observation results of annealed 430 after dual oxidation, a model is created to describe the growth of oxide scale for samples with large alloy grain size. Generally, Cr and Mn form the $(Mn,Cr)_3O_4$ spinel phase, which can reduce the oxidation rate and Cr evaporation [23, 27]. The most notable effect of grain size is that there is less Cr and Mn diffusion along alloy grain boundaries in the large grain alloys. As shown in **Fig. 4.19**, the growth of oxide scale can be divided into three stages. At the initial stage is the formation Fe_2O_3 near the alloy grain boundaries. Hydrogen diffuses through alloy grain boundaries, which may increase the outward diffusion of Fe or create a more acid environment. The hydrogen diffusion along alloy grain boundaries promotes the formation of Fe_2O_3. The second stage includes two parts. One part is that a spinel phase forms near the Fe-rich nodules. After the initial stage, some Mn can still diffuse along alloy grain boundaries and form spinel phase next to the Fe-rich nodules. The

other part is that Cr diffuses to the alloy surface and form a Fe-rich solid solution of Fe_2O_3 and Cr_2O_3. The final stage is that one whole alloy grain is covered by normal oxide scale (Cr-rich area) or Fe-rich area, which is controlled by the local Cr and Mn concentration. Similar as the step II, Spinel phase can still grow by Mn and Cr outward diffusion along the alloy grain boundaries

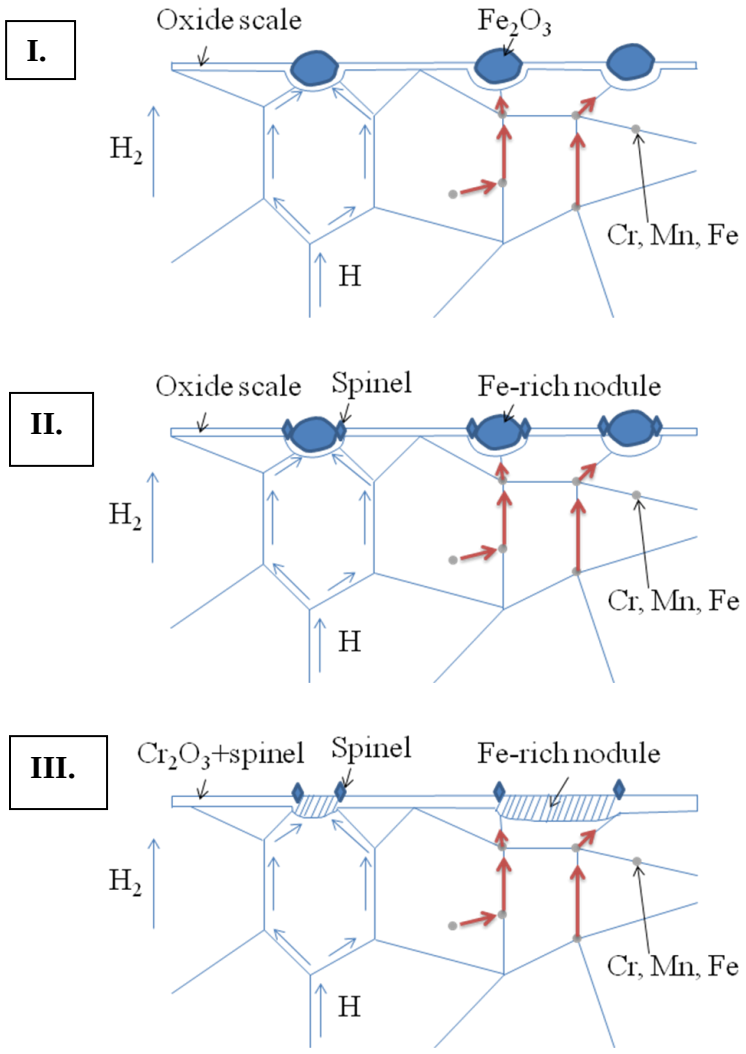

Fig. 4.19 Model for oxide scale growth of samples with large alloy grain size in dual atmosphere oxidation.

Comparing the annealed 430 and 441 dual samples, a large amount of Fe-rich nodules were found close to the 430 alloy grain boundaries areas, where as 441 dual

atmosphere samples contained Fe-rich nodules only in isolated areas. The main difference between 430 and 441 is that alloy 441 contains Nb and Ti elements. An earlier study found that during high temperature corrosion of 441 Nb-containing laves phase precipitates deposited at alloy grain boundary. In the current work, Fe_2Nb precipitates were found at the alloy grain boundaries (**Fig. 4.7b**). The crystal structure of Fe_2Nb is C14 laves phase, which has been extensively studied as a hydrogen storage material [71, 72], so hydrogen could occupy the interstitial sites of Fe_2Nb and thus act as a hydrogen trap for hydrogen diffusion through the alloy. These grain boundary precipitates are not present in 430. The grain boundaries of alloy 430 are reversible site for hydrogen storage, which has a lower binding energy (<80KJ/mol) to hydrogen. Generally, reversible site do not prevent the diffusion of hydrogen through the grain boundaries [51-55]. Therefore, more rapid hydrogen diffusion along grain boundaries is expected.

4.4 Conclusions

The dual atmosphere oxidation of samples with large alloy grain size led to the formation of Fe-rich nodules, which is related with the hydrogen diffusion along the alloy grain boundaries. Hydrogen may facilitate the outward diffusion of Fe or create a more acid environment, which favors the formation of Fe_2O_3. Fe-rich nodules tend to form at the surface area close to the alloy grain boundaries.

Large alloy grain size limits the outward diffusion of Cr and Mn. Due to the large grain size, the alloy substrate may not supply enough Mn to form protective $(Mn,Cr)_3O_4$ spinel layer. After dual atmosphere oxidation, a large amount of Fe-rich nodules near the alloy grain boundaries are formed on the air side of annealed 430 dual samples. For

longer time, $(Fe,Cr)_2O_3$ nodules are formed and the $(Fe,Cr)_2O_3$ nodules are enlarged to cover one whole alloy grain surface. Spinel phase is formed at the alloy grain boundaries area by Mn and Cr outward diffusion along the alloy grain boundaries.

In the case of 441, Fe-rich nodules are present only in isolated areas and the oxide scale consists mostly of spinel phase and underlying Cr_2O_3. The hydrogen trapped by Fe_2Nb at alloy grain boundaries area might contribute to the lower amount of Fe-rich nodules on 441 oxide scale.

CHAPTER 5

LOW-CHROMIUM ALLOYS FOR SOFC INTERCONNECTS

5.1 Introduction

Ferritic stainless steel alloys have a combination of good oxidation resistance and appropriate coefficient of thermal expansion that makes them attractive for use as interconnects in SOFCs [4, 8]. However, chromia can be oxidized to vapor species, which can lead to poisoning of the cathode. For reducing the Cr poisoning, different alloy elements have been added in the ferritic stainless steel, including Mn and Ti. These additions of alloy elements formed an oxide scale with lower Cr activity. Another possible method is to reduce the Cr concentration in the alloy. In this work, the samples with chromium contents from 13-18% and other alloying additions typical of those of alloy 441 (*i.e.* small amounts of niobium and titanium) were evaluated by dual atmosphere oxidation experiments.

For long-term application of ferritic stainless steel as SOFC interconnect, ceramic coating is the most feasible method to reduce the Cr evaporation. Other work has found that spinel coating of cobalt and manganese shows good performance due to its good electrical conductivity and compatibility with other SOFC components [127, 138]. With the ceramic coating, alloys with lower chromium contents could potentially be used. In this work, the oxidation behaviors of a series of $Mn_{1.5}Co_{1.5}O_4$-coated and uncoated

ferritic steel alloys were studied to determine if the reduction of Cr concentration influence the oxidation resistance of $Mn_{1.5}Co_{1.5}O_4$-coated samples in SOFC environment.

5.2 Experimental

5.2.1 Dual atmosphere oxidation of uncoated samples with different Cr concentration

Table 5.1 lists the compositions of the ferritic alloys with different Cr concentration, which were provided by Allegheny Technologies Inc.. The composition of 17%Cr and 18%Cr samples is similar to that of alloy 441. The Circular disks (33 mm dia) were sectioned from plates (thickness: 1.0 mm) by electrical discharge machining (EDM). For each dual-atmosphere test the circular disk was sealed to the end of an AISI304 stainless tubing (OD: 25.4 mm, ID: 19.3 mm) by Ni-based BNi-2 braze. The braze sealing was performed in a vacuum furnace (at least 1×10^{-3} torr) by heating from room temperature to 1050 ℃, holding for 30 min, and then cooling to room temperature. The dual oxidation experiments of uncoated samples were done in the same setup as previous dual oxidation (**Fig. 3.1**). One side of the coupon was exposed to 35ml/min wet Ar-5 vol% H_2 (3vol% H_2O) and the other side was exposed to 5ml/min dry cylinder air (moisture ≤67.0PPM). The wet hydrogen and air were prepared by passing the gas through water bubblers at room temperature. Another plate sample was kept in the quartz tube as the control sample. The quartz tube was kept in a tube furnace. Before heating, the system was flushed with the experimental atmosphere for 24 hours. The samples were then heated and held at 800 ℃ for 200 hours.

Table 5.1 composition of alloys with different Cr concentration

Element (wt%)	Cr	Mn	Si	Ti	Nb	Fe
13%Cr	13.0	0.3	0.4	0.2	0.3	Balance
15%Cr	15.1	0.3	0.4	0.2	0.3	Balance
17%Cr	16.9	0.3	0.4	0.2	0.4	Balance
18%Cr	17.8	0.3	0.4	0.2	0.4	Balance
441	18.0	0.4	0.3	0.2	0.5	Balance

After the dual oxidation test, the tube furnace was turned off and the experimental atmosphere was maintained while cooling to room temperature. After the test, the samples were cleaned with acetone and the weight of control samples was measured. Then, the dual atmosphere exposed coupon was removed by cutting the end of the 304 tubing. The surface of the dual atmosphere and control samples were analyzed by X-ray diffraction (XRD) and a JEOL JSM-7000F scanning electron microscope (SEM). The average composition of surface oxide scale was measured by EDS in five random areas with 200X magnification. The compositions of grain and grain boundaries were compared in 5 random areas with 5 grain and 5 grain boundary point EDS tests. After surface observation, the samples were electroplated with Ni and a cross-section sample was prepared using an Accutom-5® cut-off machine. The control and dual-atmosphere samples were epoxy-mounted, polished and characterized using the SEM. The thicknesses of the oxide scales were estimated by measuring 5 thicknesses in micrographs from 10 random positions (i.e. 50 measurements).

5.2.2 Oxidation of $Mn_{1.5}Co_{1.5}O_4$ coated samples with different Cr level

The spinel $Mn_{1.5}Co_{1.5}O_4$ powder was applied by the Pacific Northwest National laboratory (PNNL) with a slurry-based coating process [97]. $Mn_{1.5}Co_{1.5}O_4$ powder was synthesized by glycine–nitrate process. The precursor ash was achieved by heating solution of $Mn(NO_3)_3$, $Co(NO_3)_3$ and glycine to combustion point. Then calcination of the ash was performed in air at 800 ℃ for 4 hours and attrition milled. After the milling, the powder was mixed with Ferro BV-111-2 binder to form slurry. The slurry was sprayed onto stainless steel plate samples and dried in oven at 80 ℃ for 1-2 hour. To obtain a denser coating, the coated samples were heat treated in an Ar-3%H_2O-2.75%H_2 environment at 800 ℃ for 2 hours. Then, the $Mn_{1.5}Co_{1.5}O_4$ spinel layer was developed in subsequent oxidation experiment.

The isothermal oxidation experiment was performed in Lindberg® 54233 tube furnace at 800 ℃ in lab air for 800 and 1600 hours. Cyclic oxidation experiment was performed in Blue M Stabil-Glow® box type furnace at 800 ℃ for 800 hours. The cyclic oxidation was consisted of 25-hour exposures in laboratory air with furnace heating and cooling between cycles. Between each cycle, the weight was measured. The weight change was used to determine the oxidation rate. After the oxidation experiment, the surface oxide scale was characterized by XRD and SEM with EDS. Then the samples were electroplated with Ni and the cross section microstructure was characterized by SEM. The oxide scale thickness was measured by 5 measurements in 10 randomly selected areas (i.e. 50 measurements). The interface between the oxide scale and $Mn_{1.5}Co_{1.5}O_4$ coating was one of the most critical concerns in current study. The element distribution was studied by EDS at the interface region.

5.3 Results and discussion

5.3.1 Dual atmosphere oxidation of uncoated samples with different Cr level

The weight gains of control samples are shown in **Fig. 5.1**. The 13%Cr sample has the highest weight gain of all four control samples. Normally, samples with higher Cr concentration form more protective Cr_2O_3 oxide scale, which can effectively reduce the growth of oxide scale. 18%Cr control sample has a little higher Cr concentration and should have a lower weight gain than that of 17% Cr control sample. The opposite results may be caused by the spallation of oxide scale during experiment. Previous study has found that the oxide scale of alloy 441 is not stable and fracture occurs at the weak bonding between Fe_2Nb Laves phase and TiO_2 particles at alloy grain boundaries areas **[83]**. Another possible reason is that the Cr concentration is only 1% difference between 17%Cr and 18%Cr samples. The test time is only 200 hours and not long enough to show difference in oxidation behavior.

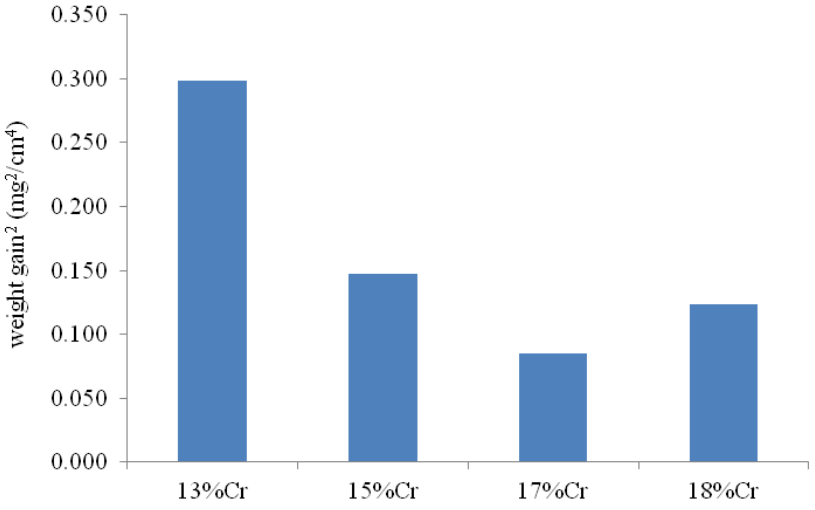

Fig. 5.1 Weight gain of 13%Cr-18%Cr control samples after 200 hours dual oxidation.

Fig. 5.2 shows the scale thickness of control samples and air side of dual samples measured by SEM. The thickness differences are compared by statistic ANOVA analysis with 95% probability. The scale thickness measurement results have a similar trend as the weight change results. Samples with higher Cr concentration have thinner oxide scale. 18%Cr control sample has a statistically thinner oxide scale than that of 17%Cr control samples, which is slightly different with the weight gain results in **Fig. 5.1**. The area selection for thickness measurement by SEM avoided the spallation area. It is reasonable that 17%Cr sample has thicker oxide scale than that of 18%Cr samples. Comparing to control and air side in each group, it looks that, except 13%Cr samples, other samples has a little thicker oxide scale on control sample than that of air side, but ANOVA analysis found that the different is insignificant. In this work, the oxide scale of air sides has a similar thickness with that of air control samples. The standard deviation of 13%Cr air side is very large. This is caused by the thick Fe-rich nodules formed at air side after dual oxidation.

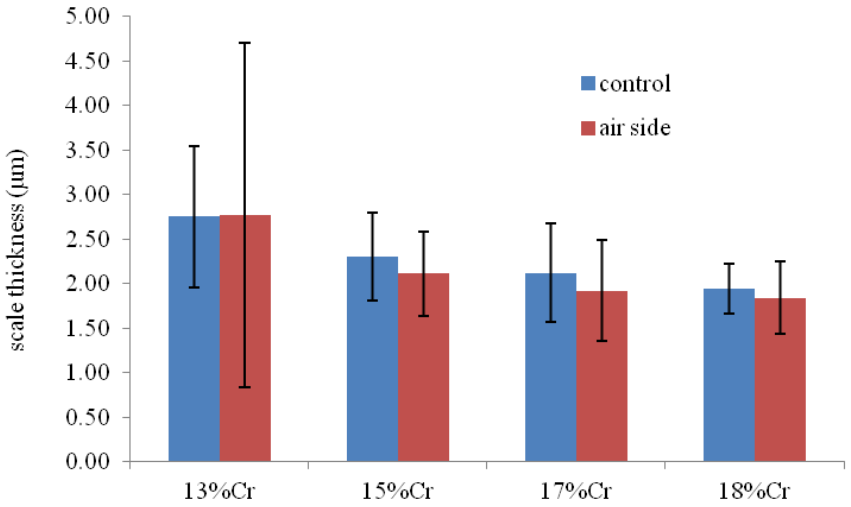

Fig. 5.2 Oxide scale thickness measurement results of control and air side after 200 hours dual oxidation with standard deviation

The XRD patterns of air control and side is shown in **Fig. 5.3.** Except 13%Cr air side, the XRD patterns of all other samples are similar and composed of Cr_2O_3 and $(Mn,Cr)_3O_4$ spinel phase. XRD patterns of all control samples are also composed of Cr_2O_3 and $(Mn,Cr)_3O_4$ spinel phase. The XRD pattern of 13%Cr air side shows Fe_2O_3 peaks next to the peaks of Cr_2O_3. Subsequent SEM observation found large amount of Fe-rich nodules on surface of 13%Cr after 200 hours dual oxidation, which is consistent with the XRD patterns.

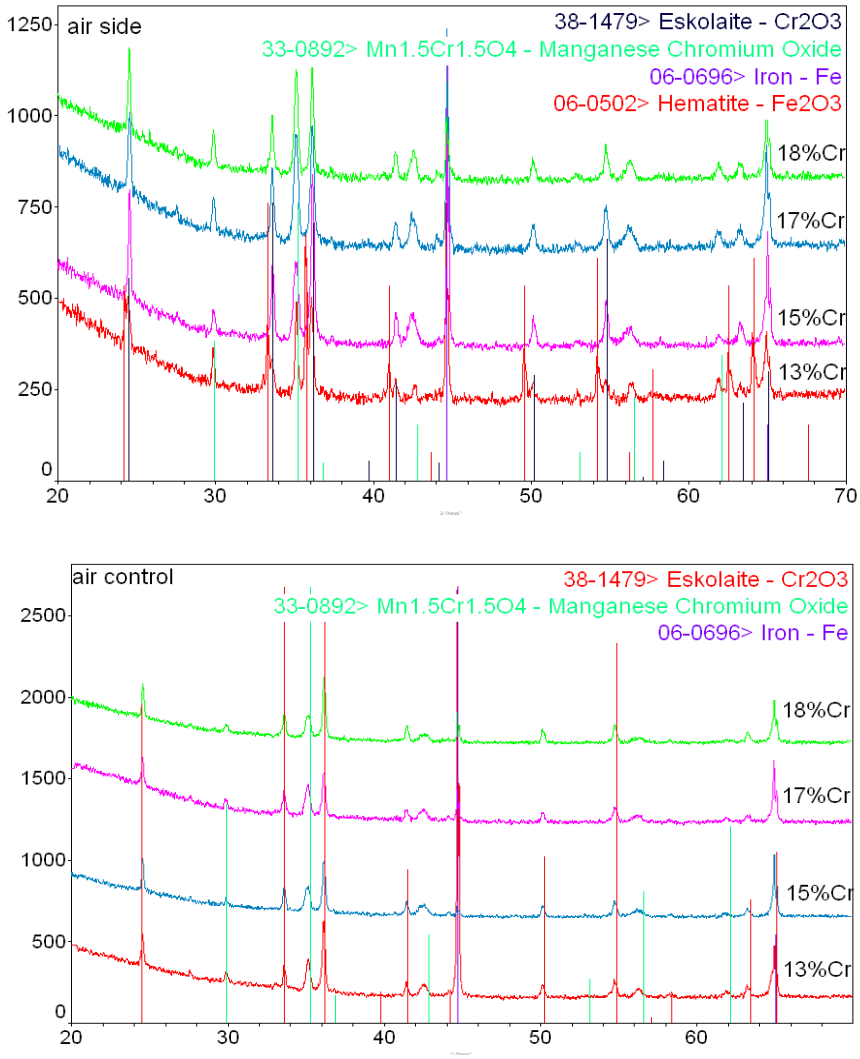

Fig. 5.3 XRD pattern of air side after 200 hours dual oxidation.

The control and air side surface microstructure of 13%Cr-18%Cr samples after 200 hours dual oxidation are shown in **Fig. 5.4**. On the air-side surface of 13%Cr samples, large amounts of Fe-rich nodules were found. Fe concentration in these nodules is close to 90% and they show needle-shape appearance. XRD spectra contained Fe_2O_3 peaks indicating that the Fe-rich nodules are Fe_2O_3. The surface oxide scale of 15%Cr sample air side contained only a small area with Fe-rich nodules. For 17%Cr an 18Cr samples, similar surface microstructure was found on air control and air side. With increase Cr concentration, the samples have a better dual oxidation resistance. High Cr is expected to promote the formation of more protective Cr_2O_3 layer, which limits the outward diffusion of Fe to form Fe-rich nodules. Based on the SEM results of uncoated 13%Cr-18%Cr samples dual atmosphere oxidation, Cr concentration of 13%Cr and 15%Cr samples is too low to avoid abnormal growth of Fe-rich nodules.

In chapter 3, the oxide scale formed on the air side of 441 contains some Fe-rich nodules under the same dual oxidation experiment. Alloy 441 has similar composition as 17%Cr and 18%Cr samples, but there are no Fe-rich nodules observed on the oxide scale of 17%Cr and 18%Cr samples. The difference between these 17%Cr and 18%Cr samples and alloy 441 is the alloy grain size. The alloy grain size of the samples with different Cr concentration is about 38 μm, while the grain size of 441 is 50 μm. Samples with smaller alloy grain size have more alloy grain boundaries as the fast path for Cr and Mn outward diffusion. It has been found that Cr_2O_3 and $(Mn,Cr)_3O_4$ spinel phase effectively reduce the diffusion of hydrogen [31] [94, 95]. Small alloy grain size is beneficial to the fast formation of protective Cr_2O_3 and $(Mn,Cr)_3O_4$ spinel phase,

especially at initial stage. The Cr_2O_3 and $(Mn,Cr)_3O_4$ oxide scale become a barrier for hydrogen to diffuse into the alloy and mitigate the growth of Fe-rich nodules.

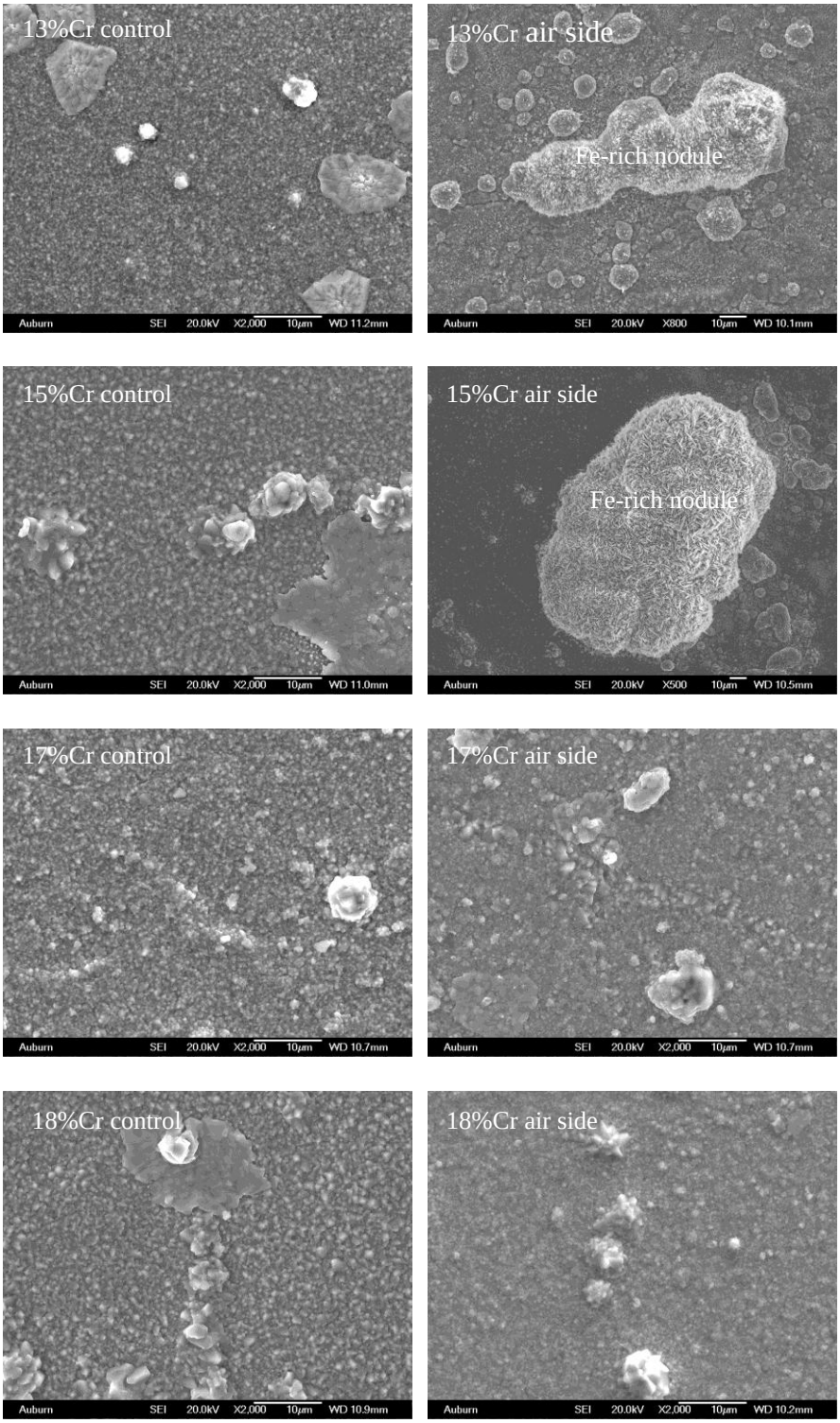

Fig. 5.4 Oxide scale surface microstructure of 13%Cr,15%Cr 17% and 18%Cr samples after 200 hours dual atmosphere oxidation.

Fig. 5.5 shows section microstructure of Fe-rich nodules formed on normal oxide scale after 200 hours dual atmosphere oxidation of 13%Cr samples. In most areas, the oxide scale is composed of Cr_2O_3 and a surface $(Mn,Cr)_3O_4$ spinel layer. In the Fe-rich nodule area, a similar oxide scale formed as the Fe-rich nodules in 441 after dual oxidation. Cr_2O_3 and $(Mn,Cr)_3O_4$ spinel layers formed at the interface between the Fe-rich nodules and alloy. **Fig. 5.6** shows the cross section microstructure of 15%Cr, 17%Cr and 18%Cr air side after 200 hours dual oxidation. They all have same cross section microstructure as the oxide scale formed under normal single atmosphere oxidation. In both **Fig. 5.5** and **5.6**, slightly high concentrations of Ti, Si and/or Nb are found at the interface between the alloy and oxide scale, which is consistent with the 441 oxidation results in previous chapters.

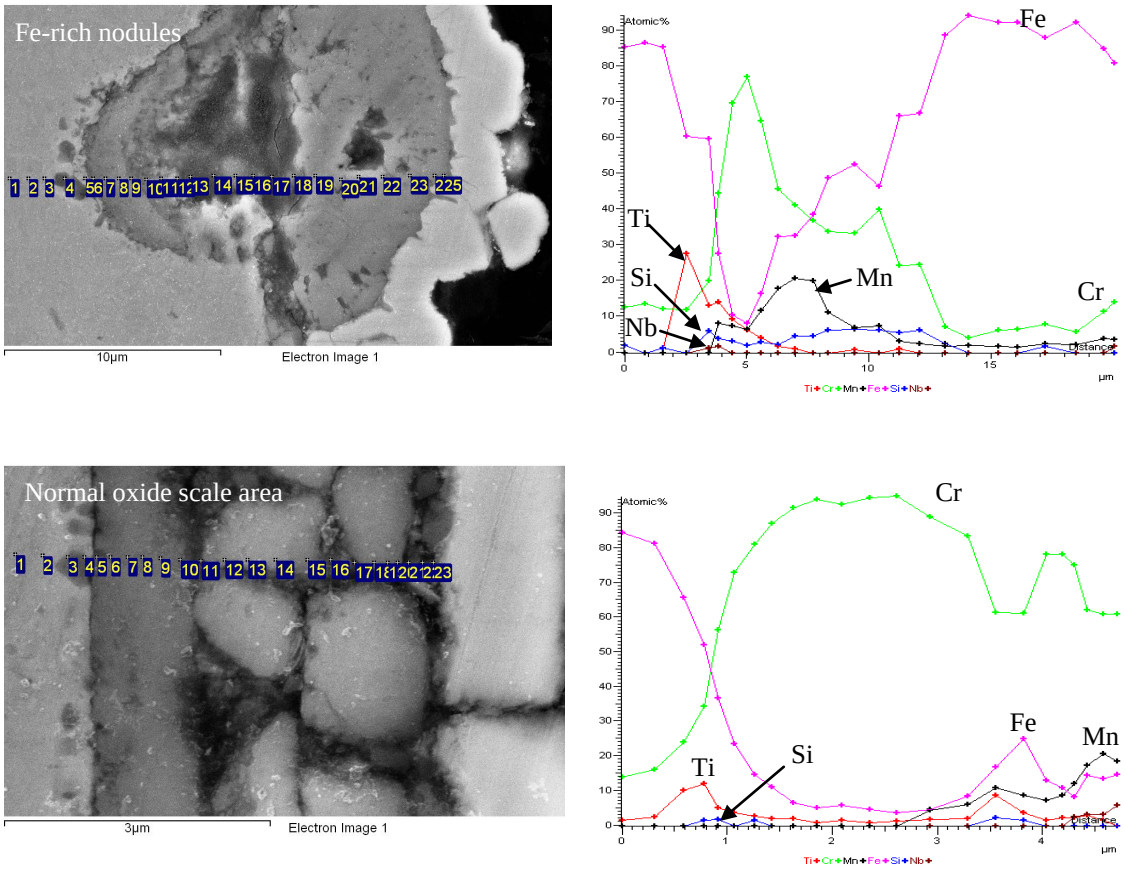

Fig. 5.5 Cross section microstructure of 13%Cr air side after 200 hours dual oxidation

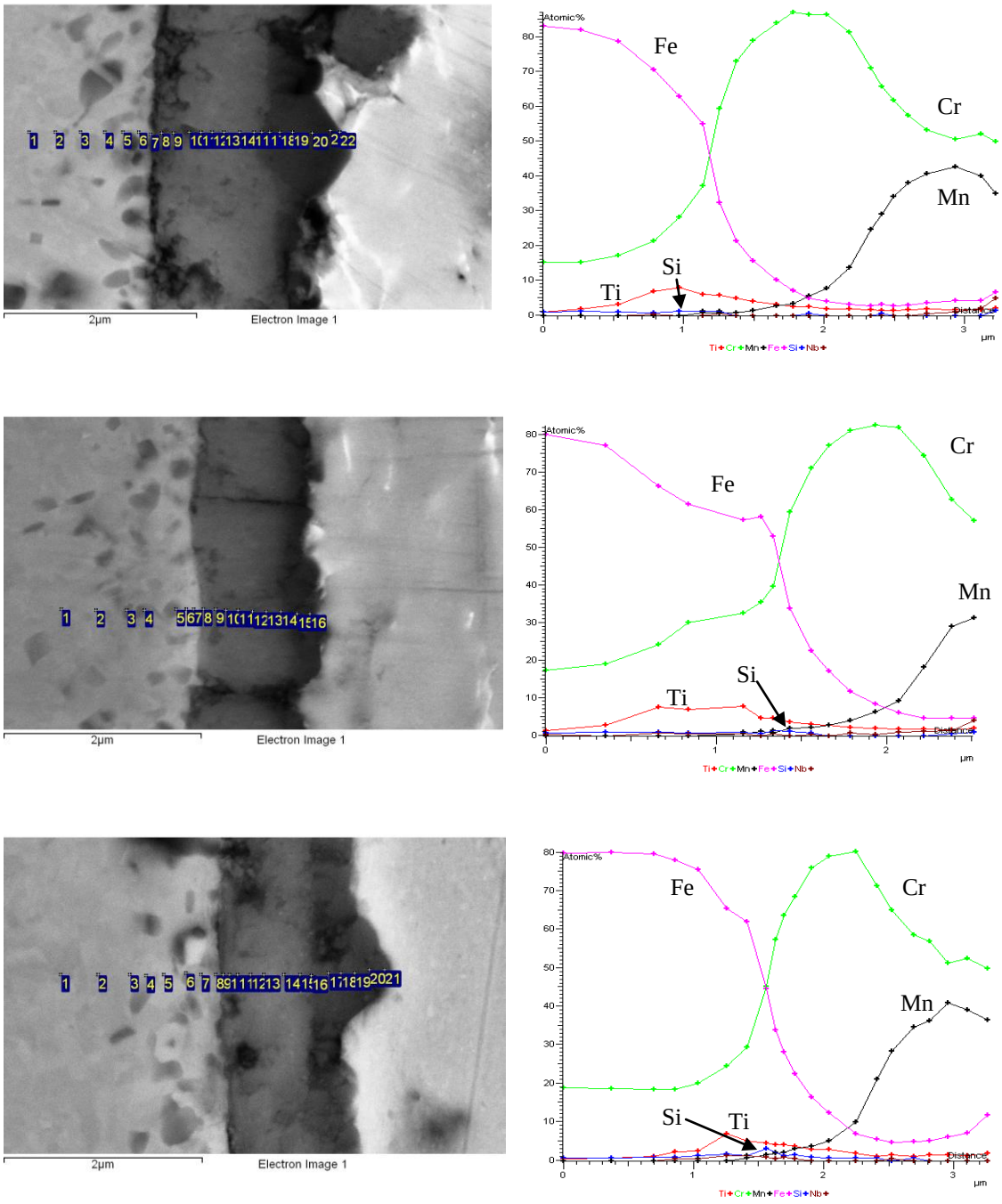

Fig. 5.6 Cross section of uncoated 15%Cr, 17%Cr and 18%Cr air side after 200 hours dual oxidation.

The average composition of surface oxide scale is shown in **Fig. 5.7**. Due to formation of large area of Fe-rich nodules, 13%Cr is not included in **Fig. 5.7.** Comparing 15%Cr, 17%Cr and 18%Cr samples, the Ti and Cr compositions of the surface oxide scale are similar. The oxide scale on the air side showed a little less Mn and little higher Fe concentration than the oxide scale surface formed on the control samples. The higher Fe concentration at air side might have been due to the hydrogen diffusion in dual oxidation. In other studies, hydrogen was found to diffuse into the Cr_2O_3 and create vacancies[96], which increased the outward diffusion of Cr in the chromia scale [11, 96]. In the current work, hydrogen may have diffused through the alloy and form vacancies in the oxide scale of air side. These vacancies may have facilitated the Fe outward diffusion.

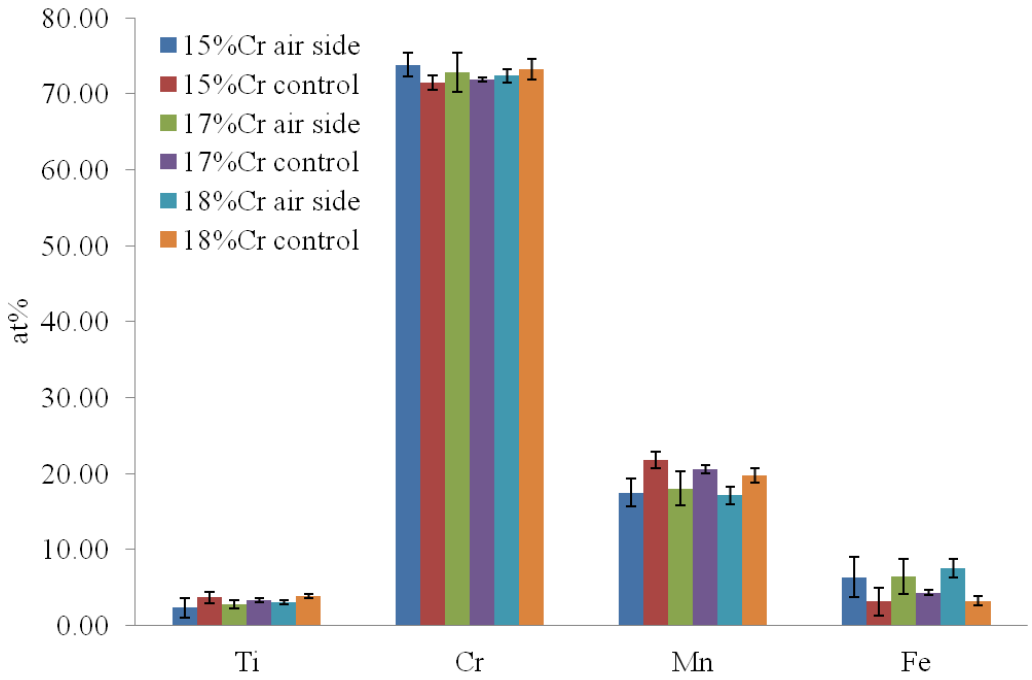

Fig. 5.7 Average surface oxide scale composition of 15%Cr, 17%Cr and 18%Cr samples after 200 hours dual atmosphere oxidation.

Fig. 5.8 shows the ratio of Mn and Fe to Cr+Mn+Fe on the surface after dual atmosphere oxidation. Because of randomly distributed TiO_2 at the ridges on the oxide scale surface, the ratios of Mn or Fe to Cr+Mn+Fe are selected to analyze if Mn and Fe tend to diffuse along the grain boundaries area. Based on **Fig. 5.8**, there is a high Mn concentration at the ridge on the oxide scale surface, which is consistent with results presented in a previous chapter indicating that Mn tends to diffuse along alloy grain boundaries. **Fig. 5.8** shows similar results in **Fig. 5.7** that the oxide scale of air side has a little higher Fe concentration than that of the control samples. The deviation of Fe/(Cr+Mn+Fe) is high and this should be attributed by the scattered distribution of Fe elements. Ridge areas showed similar Fe concentration as that in grain. Comparing to as-received 441, the grain size of 15%Cr, 17%Cr and 18%Cr samples is smaller and more alloy grain boundaries are available for Mn and Cr outward diffusion along alloy grain boundaries. The sample with smaller alloy grain size may form a more protective oxide scale at the alloy grain boundaries area. This may have reduced the diffusion of hydrogen along the oxide scale near the alloy grain boundaries, so Fe did not show a strong tendency to diffuse near alloy grain boundaries in current study.

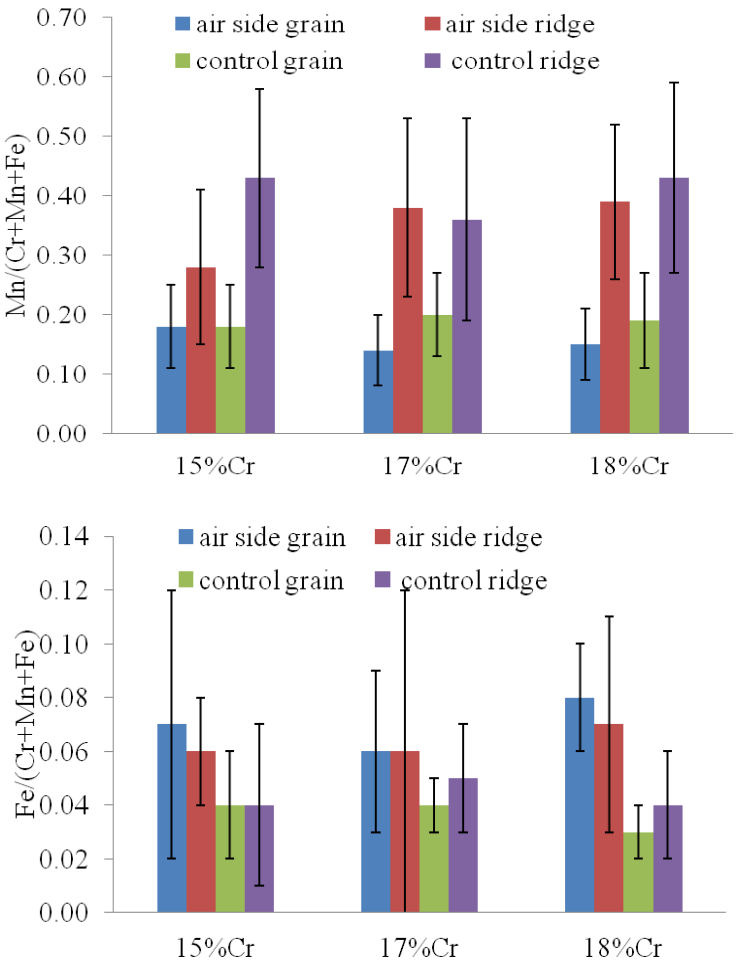

Fig. 5.8 Mn and Fe ratios in surface oxide scale on alloy grain and grain boundaries area.

5.3.2 Oxidation experiment of $Mn_{1.5}Co_{1.5}O_4$ coated samples with different Cr level

The weight gain of samples with fitted line after 800℃-800hour cycle oxidation is shown in **Fig. 5.9**. Due to the reoxidation of cobalt in the coating, the overall weight gain of coated samples are larger than those of the uncoated samples. For the coated samples, the parabolic oxidation rate was fit beginning at 75 hours. **Fig. 5.10** shows the parabolic rate constant as the Cr concentration. After the initial stage with large weight gain, the subsequent growth rate of the coated samples were lower than those of uncoated samples.

This suggest that the MCO spinel coating may have limited the inward diffusion of oxygen and prevented detrimental effects, such as spallation of oxide scale. Except 15%Cr, the weight gains of coated and uncoated samples are similar. 17%Cr and 18%Cr samples have similar composition as 441 and were expected to behavior similarly, but, uncoated 17%Cr and 18%Cr samples shows a much higher oxidation rate than those of 441. The reason is not clear yet, but may have been related with small amount difference in minor alloy elements or process difference with the relatively small batch size.

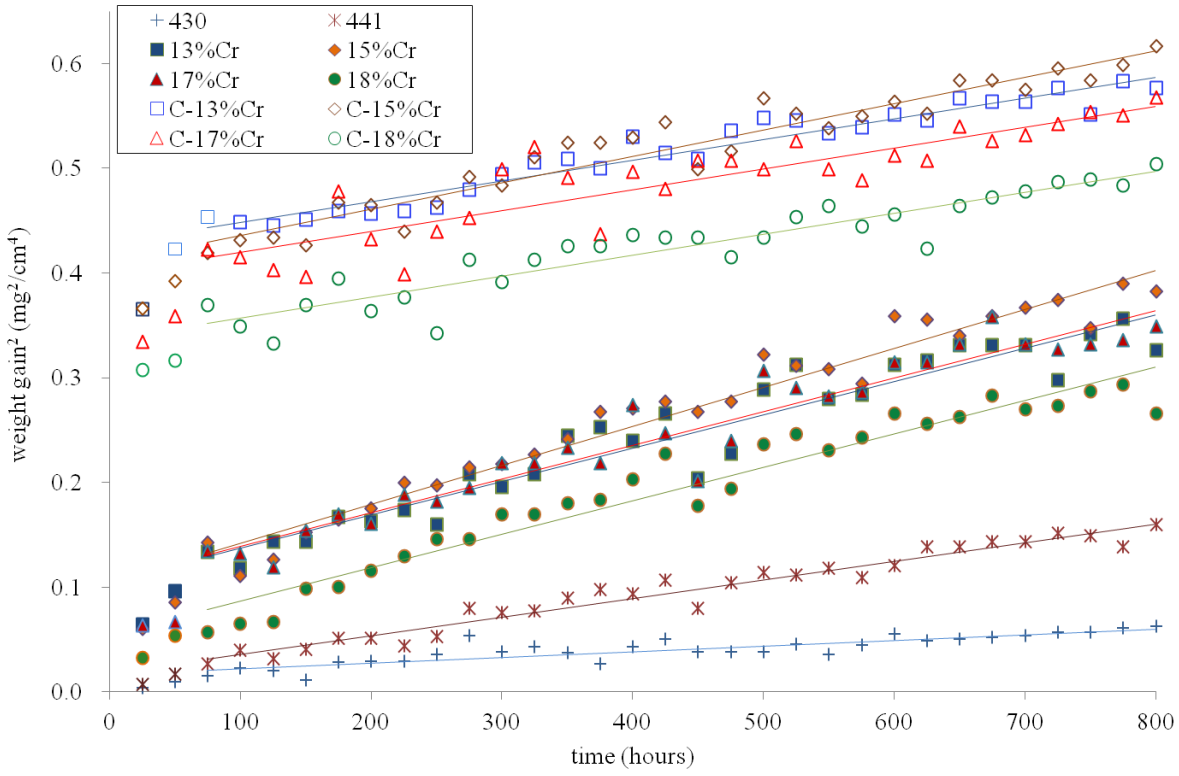

Fig. 5.9 Weight gain of coated and uncoated samples after 800 ℃-800 hours cycle oxidation (25-hour cycles).

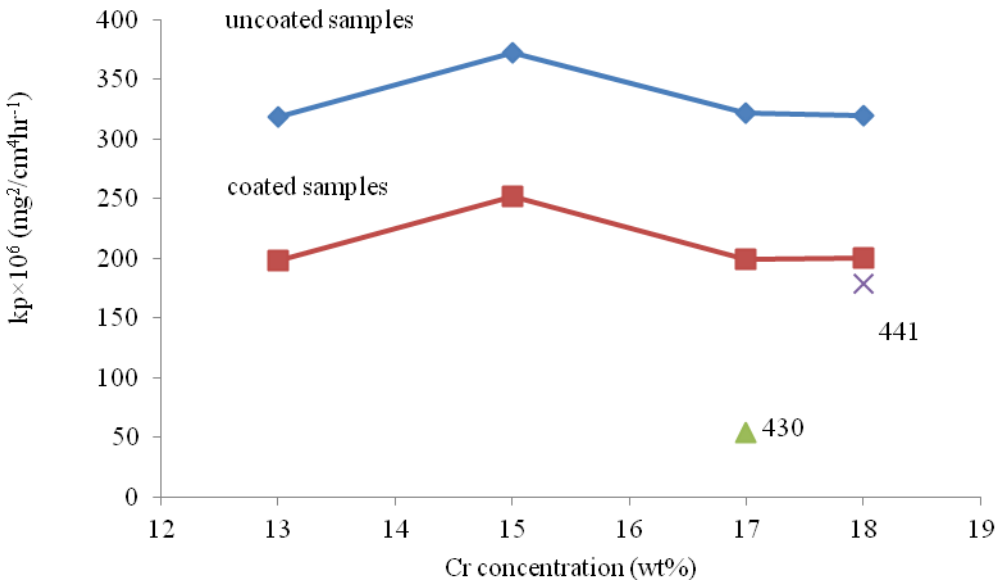

Fig. 5.10 Parabolic rate constant for cycle oxidation of coated and uncoated samples in air at 800 ℃.

The weight gains of several samples after isothermal oxidation in lab air are shown in **Fig. 5.11**. Due to the reoxidation of cobalt in the MCO spinel coating, the weight gains of coated samples are higher than that of uncoated 430 and 441 at the initial stage (such as 200 hours). This is similar as the cycle oxidation result. After 800 hours isothermal oxidation, the weight gain of C-13%Cr is very high and C-18%Cr have the least weight gain in coated samples. C-17%Cr sample had a little lower weight gain than that of C-13%Cr sample. After 1600 hours oxidation, it seems that the weight gain shows an opposite result. This result is related with the spallation of coating, which was observed in subsequent surface SEM observation. **Fig. 5.12** shows the oxide scale thickness by SEM measurement. After 800 hours oxidation, the oxide scale thickness decrease with increase Cr concentration in the coated samples. After 1600 hours oxidation, all the

coated samples have the similar oxide scale thickess. These are consistent with the weight gain result in **Fig. 5.10**.

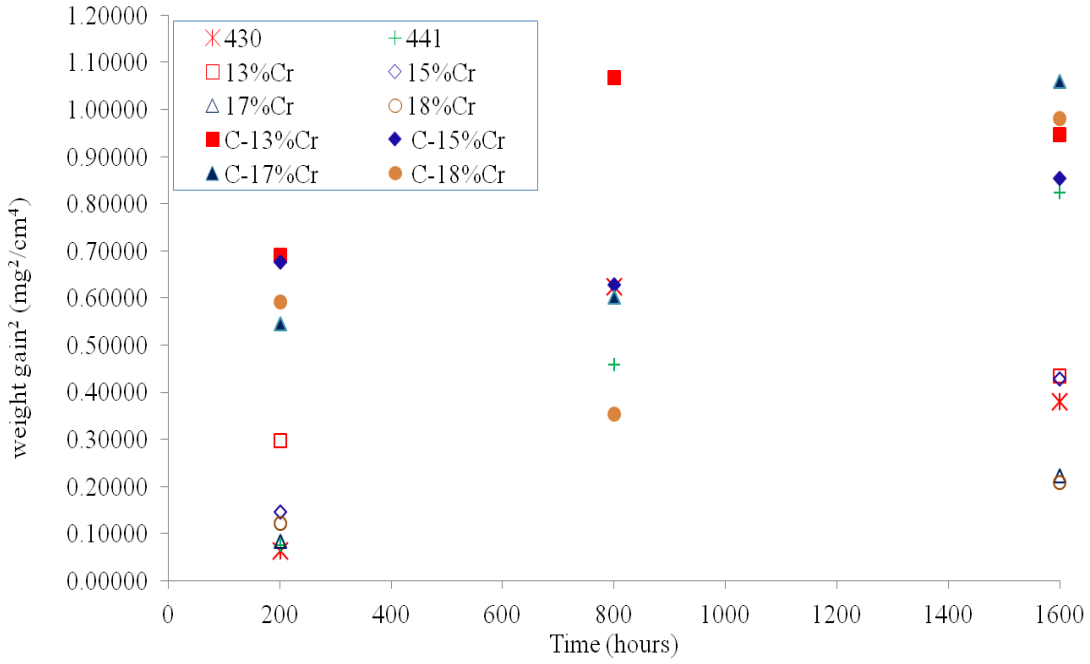

Fig. 5.11 Weight gain of 430, 441 and Coated and uncoated samples after isothermal oxidation experiment.

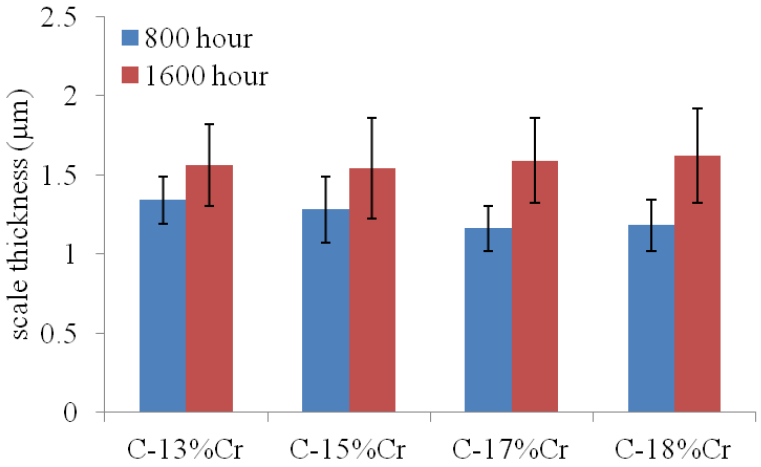

Fig. 5.12 Oxide scale thickness of coated samples after 800 and 1600 hours isothermal oxidation in lab air.

Fig. 5.13 shows the XRD patterns of coated samples after 800 and 1600 hours isothermal oxidation in lab air. After 800 hours oxidation, all the coated samples have similar XRD pattern, which is composed of $(Mn,Co)_3O_4$ spinel phase. The XRD patterns of coated samples after 800-hour cycle oxidation are almost same as those oxidized in the 800-hour isothermal condition. After 1600 hours, the coated samples show a new peak at 65 degrees. This peak could be the Cr_2O_3 or Fe peaks, but no other Cr_2O_3 or Fe peaks are shown. Besides of the peak at 65 degree, some other peaks are shown in coated 13%Cr samples after 1600 hours oxidation, which do not correspond to the chromia or iron. These peaks might be the $CoFe_2O_4$. In SEM observation, a high concentration of Fe was found in the oxide scale of C-13%Cr sample after 1600 hours oxidation. 13%Cr sample has the lowest Cr concentration in all the four coated samples. For coated samples after 1600 hours oxidation, 13% Cr is not enough to form protective oxide scale to prevent the Fe outward diffusion. It is possible that Fe diffused outward and formed $CoFe_2O_4$ spinel phase by reacting with Co.

The cross section microstructure of coated samples after 800 hours isothermal oxidation is shown in **Fig. 5.14**. All the four coated samples show a similar microstructure and the oxide scale is mainly composed of Cr_2O_3. After 800 hours oxidation, a relatively clear interface between the oxide scale and $Mn_{1.5}Co_{1.5}O_4$ coating is formed. In general, the interface has relatively higher Co concentration than Mn. At the interface between the alloy and oxide scale, a slightly high Ti concentration was found. In the coating, Fe concentration is very low, even for C-13%Cr sample.

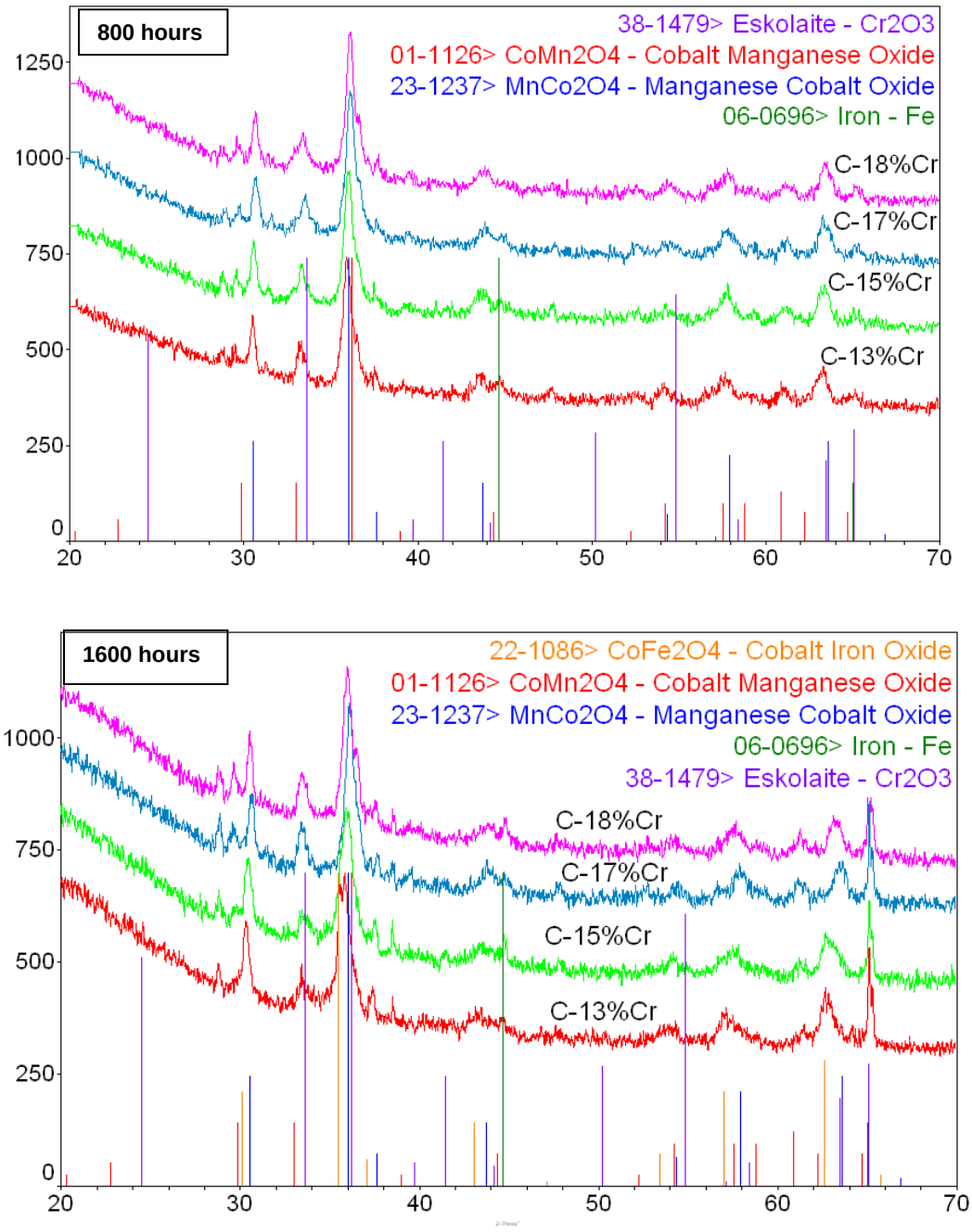

Fig. 5.13 XRD patterns of coated samples after 800 and 1600 hours isothermal oxidation in lab air.

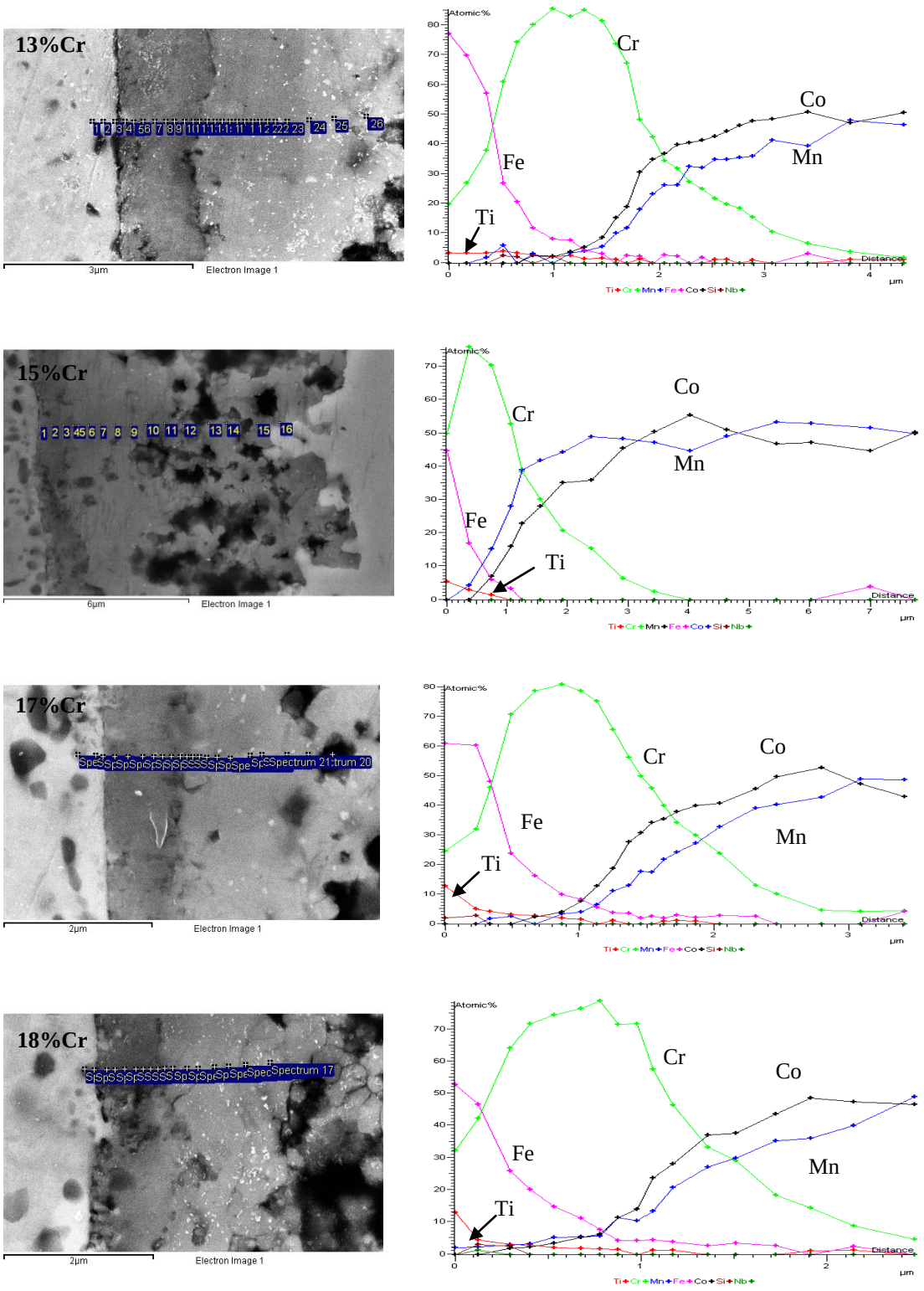

Fig. 5.14 Cross section microstructure of coated samples after 800 hours isothermal oxidation.

The surface microstructure of coated samples after 1600 hours isothermal oxidation is compared in **Fig. 5.15**. For the samples with less Cr, more oxide scale spallations were observed. The spalled area has about 20% Fe, which is much higher than in the unspalled area. **Fig. 5.16** shows the average surface composition of coated samples after 1600 hours isothermal oxidation. With the increase of Cr concentration, Fe concentration on the surface oxide scale reduced. No Fe was found on the surface oxide scale of C-17%Cr and C-18%Cr samples.

The spallation area in C-13%Cr is possibly related with the abnormally thick oxide area as shown in **Fig. 5.17**. The abnormal thick oxide scale is composed of Cr_2O_3, but there are some Fe_2Nb white particles near the abnormally thick oxide area. Generally, Fe_2Nb Laves phases tend to continuously deposit along the alloy grain boundaries. At the interface between the oxide scale and the alloy, slightly high concentration of Ti and Nb were found, which indicates that the abnormally thick area is close to the alloy grain boundary area. The abnormally thick oxide is possibly related with the oxygen inward diffusion, which often occurs at alloy grain boundaries area [7]. It is found that alloy elements in 441 and 430 tend to diffuse along alloy grain boundaries. This outward diffusion along alloy grain boundaries leads to higher stress at oxide scale on alloy grain boundaries than that on lattice. High stress may cause the opening of alloy grain boundaries and facilitate the oxygen inward diffusion [7]. 13%Cr has the lowest Cr concentration and the Cr_2O_3 layer formed on 13%Cr is less protective than the other coated samples, so it as compared to other coated samples with higher chromium content, it should be easier for Fe to diffuse outward. After 1600 hours isothermal oxidation, $CoFe_2O_4$ peaks are present in the XRD spectrum of 13%Cr indicating that Fe may have

reacted with Co and form $CoFe_2O_4$ in the spinel coating. The thermal expansion coefficients of $CoFe_2O_4$ and Cr_2O_3 are 14.9 and $9.6\times10^{-6}/℃$, respectively [139, 140]. The large difference of the thermal expansion coefficient could cause a large stress in the coating lead to coating spallation more often for C-13%Cr samples than for the other samples. Without the protection of the spinel coating, oxygen atoms can easily diffuse through the Cr_2O_3 oxide scale on C-13%Cr sample and form thick oxide scale near the alloy grain boundary area.

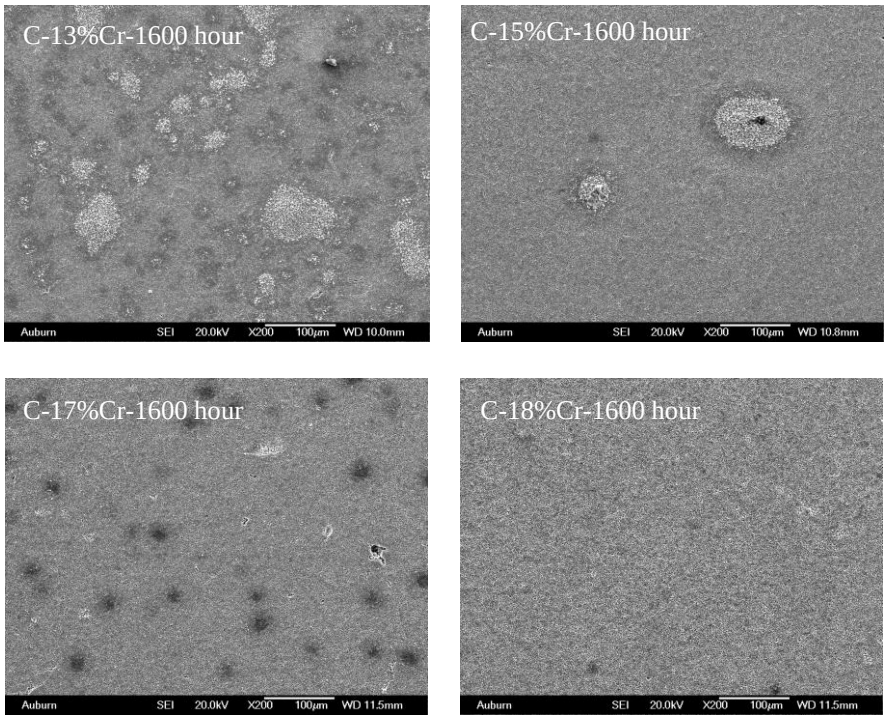

Fig. 5.15 Surface microstructure of coated samples after 1600 hours oxidation.

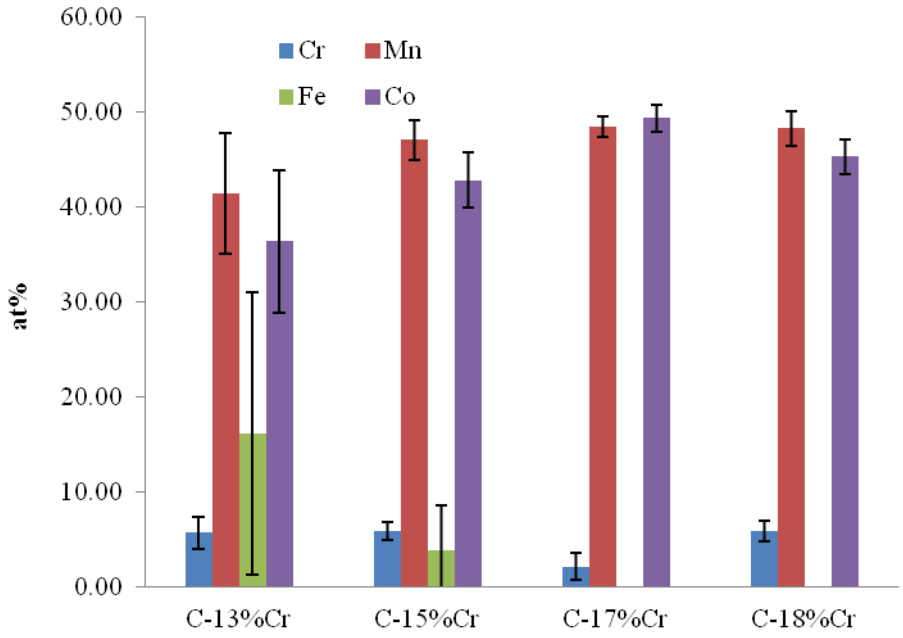

Fig. 5.16 Average surface composition of coated samples after 1600 hours oxidation

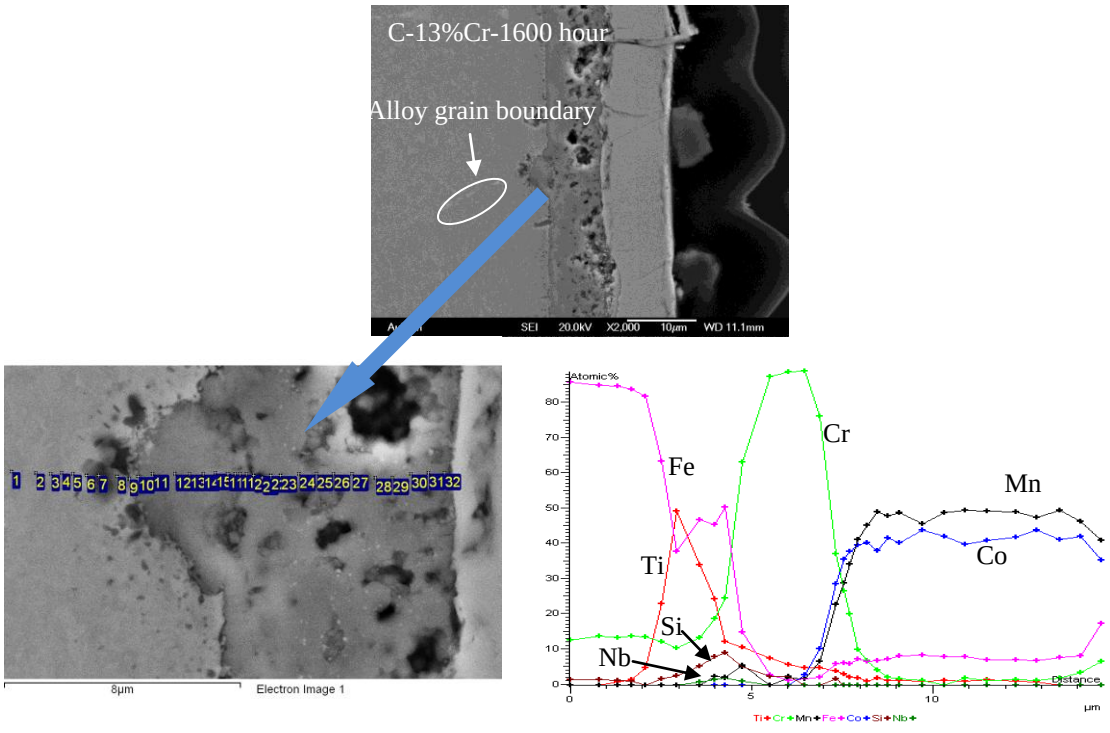

Fig. 5.17 Surface microstructure of C-13%Cr sample after 1600 hours oxidation

The typical cross section microstructure of coated samples after 1600 hours oxidation is shown in **Fig. 5.18**. The coating surfaces of low-Cr samples (C-13%Cr and C-15%Cr) samples contain about 10% Fe, but there is no measurable Fe in coating surfaces on the high-Cr alloys (C-17%Cr and C-18%Cr). The surface and cross section SEM images indicate that the Cr concentration in 13%Cr and 15%Cr samples is too low to form a protective Cr_2O_3 layer for long term SOFC application. Similarly, after 800 hours oxidation (**Fig. 5.14**), the ratio of Co to Mn at interface was always higher than that in the coating. The difference is that the interface became blurred for coated samples after 1600 hours oxidation (**Fig. 5.18**). This should be contributed by the inter-diffusion between these two regions.

Based on other studies, a similar model of reaction layer growth was created and is shown in **Fig. 5.19 [140]**. The reaction layer is composed of two regions. One is Cr^{3+} outward diffusion from the oxide scale into the spinel coating. The other is the Mn^{2+} and Co^{2+} inward diffusion into the Cr_2O_3 oxide scale. Other studies found that Cr have a very strong tendency to occupy the octahedral position of spinel phase [141, 142]. At the region next to the Cr_2O_3 oxide scale, oxide scale can supply enough Cr to occupy the octahedral position of spinel phase. So, only Mn^{2+} and Co^{2+} can diffuse into this region. In another work, a similar model was proposed [140]. This work study the reaction layer by directly heating a diffusion couple of $(Mn,Co)_3O_4$ and Cr_2O_3 plate in lab air. This work found higher ratio of Co to Mn at the reaction layer and the ratio of Co to Mn is about 3. Based on the empirical site preference energy calculation, Co^{2+} has a higher preference to occupy tetrahedral site to that of Mn^{3+} and Cr^{3+} [141]. Another possible reason is that Co has a higher diffusivity in reaction layer or $(Mn,Co)_3O_4$ spinel coating

than that of Mn. In current work, the ratio of Co to Mn is smaller than 3, which means more Mn in reaction layer. During the high temperature oxidation, coated alloy samples supplied Cr to form the reaction layers. At the same time, the coated samples may have supply Mn to the reaction layer, especially at the initials stage. So, the ratio of Co to Mn is smaller than that using Cr_2O_3 plate.

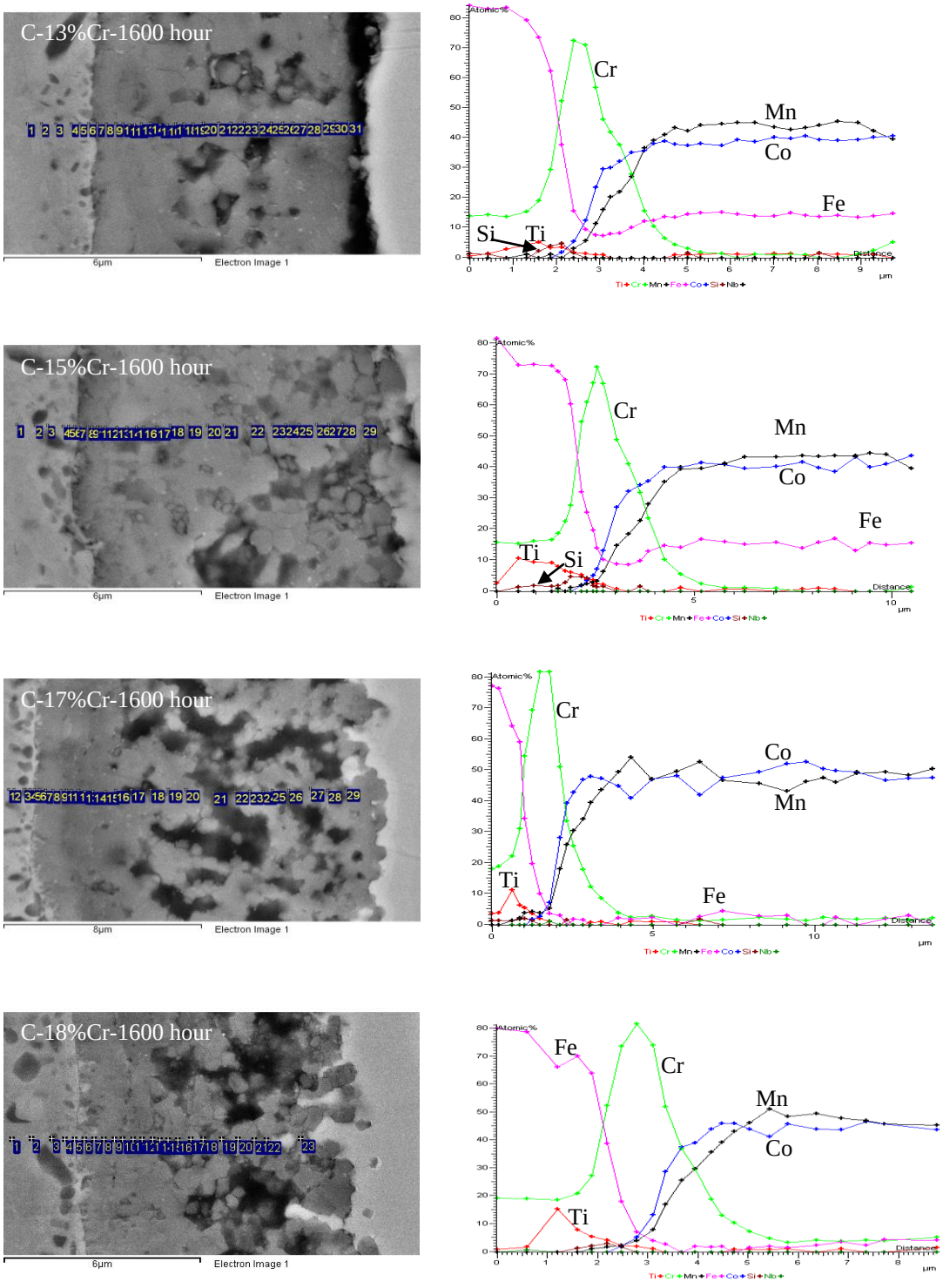

Fig. 5.18 Cross section microstructure of coated samples after 1600 hours isothermal oxidation

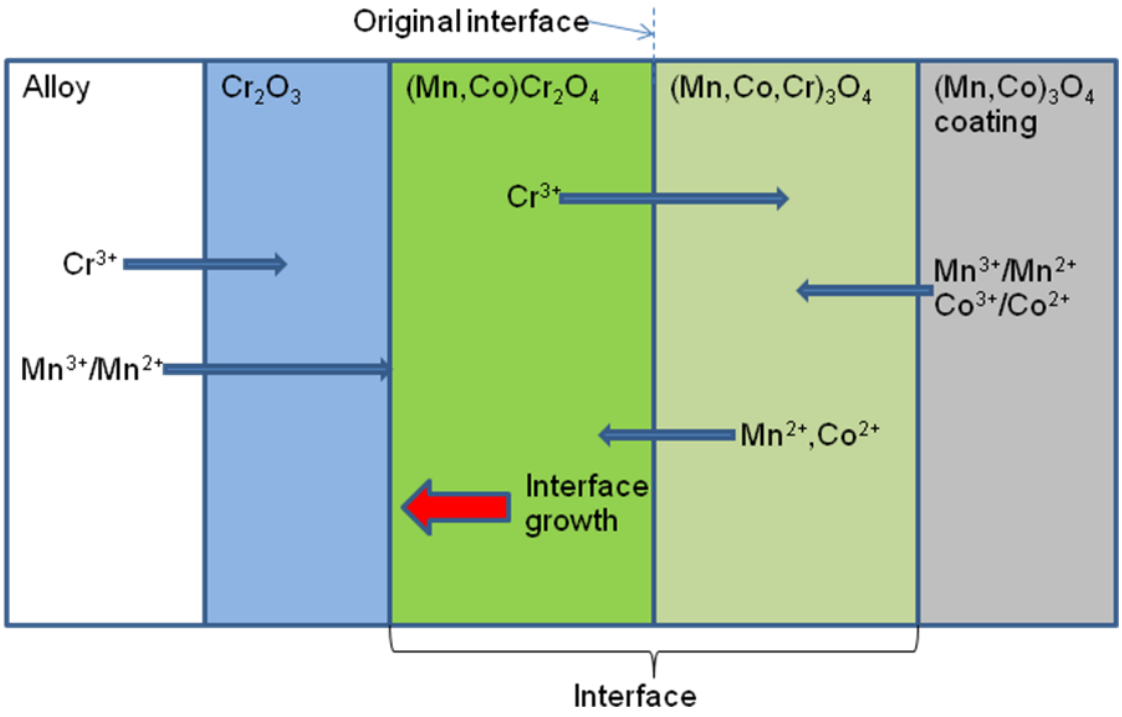

Fig. 5.19 Reaction layer development during oxidation of coated samples at 800 ℃.

5.4 Conclusion

The dual atmosphere oxidation of uncoated 13%Cr results in the formation of a large amount of Fe-rich nodules at the surface of oxide scale. With higher Cr concentration of the uncoated sample, quantities of Fe-rich nodules were reduced. The samples with higher Cr concentration have a better dual oxidation resistance.

Comparing with as-received 441, the smaller alloy grain size of 17%Cr and 18%Cr samples may have facilitated the formation of more protective oxide scale, especially at alloy grain boundary region. Hydrogen diffusion into the alloy may have facilitated the Fe outward diffusion at both alloy grain and grain boundary areas.

After long term oxidation, the coated samples with relatively low Cr concentration have more scale spallation. The scale spallation is possibly related with the formation of $CoFe_2O_4$, which has a large mismatch of the thermal expansion coefficient with Cr_2O_3 and $(Mn,Co)_3O_4$.

During high temperature oxidation, a reaction layer was formed in coated samples at the interface between the oxide scale and the coating. With longer oxidation, the interface between the scale and coating becomes more blur. High ratio of Co to Mn was found at the reaction layer. This is possibly attributed to the higher tetrahedral preference of Co^{2+} relative to Mn^{3+} and Cr^{3+} or higher diffusivity in reaction layer or $(Mn,Co)_3O_4$ spinel coating than that of Mn.

Based on the oxidation results, Cr concentration should be at least 17% to form a protective oxide scale in the SOFC environment for both coated and uncoated samples.

CHAPTER 6

CONCLUSIONS AND PERSPECTIVES

In this research, five aspects have been studied for the application of Cr-containing ferritic steel alloys 430 and 441 as SOFC interconnect materials, including the effects of water vapor in air, comparison of different flow rate in dual atmosphere oxidation, oxidation behavior at alloy grain boundaries in dual atmosphere oxidation, the effects of chromium level to the dual atmosphere oxidation behavior and long term oxidation behavior of $(Mn,Co)_3O_4$ spinel coated ferritic alloys with different chromium levels.

For samples oxidized in air containing water vapor, the presence of water vapor in the air promoted the inward diffusion of oxidant and appears to improve the adherence of the oxide scale to the alloy. In this work, 430 showed a higher growth rate with higher humidity level, but the weight change of 441 did not follow this trend. This difference may be contributed by spallation of oxide scale and chromium depletion. Due to the weak bond between the Fe_2Nb and TiO_2, the oxide scale tends to spall more easily than on 430. After dual atmosphere oxidation, the oxide scale on both 430 and 441 treated with high hydrogen flow rate contain localized Fe-rich nodules, which accelerate growth of oxide scale at the air side. High hydrogen flow rate supplied more hydrogen to diffuse through alloy to the air side and may have formed more interstitial protons in the oxide scale, which facilitate the outward diffusion of Cr, Mn and Fe and lead to more thick

oxide scale. The formation of Fe-rich nodules is possibly contributed by the Fe outward diffusion or the presence of acidic conditions at air side.

In this work, the 100 and 200 hours dual atmosphere oxidation of alloy 430 with large alloy grain size led to the formation of Fe-rich nodules tend along the alloy grain boundaries. After 400 hours dual atmosphere oxidation, $(Fe,Cr)_2O_3$ nodules are enlarged to cover one whole alloy grain surface. Spinel phase is formed at the alloy grain boundaries area by Mn and Cr outward diffusion along the alloy grain boundaries. These results indicate that the hydrogen diffusion along alloy grain boundaries facilitates the formation of Fe-rich nodules. In the current work, Mn concentration was higher at alloy grain boundaries area than that in the grain. With fewer grain boundaries, the larger alloy grain size supplies less grain boundaries as the fast path for the outward diffusion of Cr and Mn, so the alloy substrate may not supply enough Mn to form protective $(Mn,Cr)_3O_4$ spinel layer to cover the entire oxide scale. In the case of 441, Fe-rich nodules are present only in isolated areas and the oxide scale consists mostly of a spinel phase and underlying Cr_2O_3. The difference between 430 and 441 is that the Fe_2Nb phase segregates to the alloy grain boundaries. Fe_2Nb phase have been considered as a hydrogen storage material, so hydrogen trapped by Fe_2Nb at alloy grain boundaries area might inhibit the supply of hydrogen to the surface and the lower amount of Fe-rich nodules on 441 oxide scale.

To reducing the cathode poison by Cr, ferritic samples with different Cr level have been tested, including uncoated and $(Mn,Cr)_3O_4$ coated samples. After the dual atmosphere oxidation, the quantities of Fe-rich nodules on the samples were reduced with increasing Cr concentration. The samples with higher Cr concentration can form a more

protective oxide scale. As-received 441 has similar composition as 17%Cr and 18%Cr samples, but no Fe-rich nodules were formed on these two samples after dual atmosphere oxidation at the same condition. 17%Cr and 18%Cr samples have smaller alloy grain size than as-received 441, which provides further evidence that small alloy grain sizes facilitate the formation of more protective oxide scale, especially at alloy grain boundary region.

For ferritic alloy as the SOFC interconnect material, a ceramic coating is necessary for reducing chromium volatilization during long-term application. In the current work, more scale spallations were observed on the coated samples with relatively low Cr level after long term oxidation. Formation of $CoFe_2O_4$, which has a large mismatch of the thermal expansion coefficient with Cr_2O_3 and $(Mn,Co)_3O_4$, is possibly the reason for the scale spallation. During high temperature oxidation, a reaction layer was formed in coated samples at the interface between the oxide scale and the coating. This reaction layer was formed by the Co and Mn inward diffusion and Cr outward diffusion. There is high ratio of Co to Mn at the reaction layer, which may be due the higher tetrahedral preference of Co^{2+} relative to Mn^{3+} and Cr^{3+} or higher diffusivity in reaction layer or $(Mn,Co)_3O_4$ spinel coating than that of Mn. Based on the oxidation results, current work found that Cr concentration in the alloy should be at least 17% to form a protective oxide scale in the SOFC environment for both coated and uncoated samples.

As the SOFC interconnect, the effects of hydrogen to the high temperature oxidation behavior of uncoated and MCO coated ferritic alloys still need further studies,

including the ferritic alloy with different alloy grain sizes or alloy dopants and hydrogen diffusion measurement.

1) Current work found that alloy grain boundaries play an important role for the dual atmosphere oxidation behavior of ferritic alloys. Generally, the ferritic samples with smaller grain sizes show better dual atmosphere oxidation resistance and mitigate the formation of Fe-rich nodules. In the future, alloy 441 with smaller alloy grain size, even nano-grain size samples, should be developed and tested in dual atmosphere. In the future, a system work should be performed to control the alloy grain size of 441 more preciously by heat treatment and cold work. Test of samples with several different alloy grains should give a more quantitive relationship between the oxide scale growth and alloy grain size.

2) In current work, Fe_2Nb phase appears to mitigate the diffusion of hydrogen through the alloys. Fe_2Nb phase is one of hydrogen storage materials and tends to segregate at the alloy grain boundaries in the ferritic alloys. Adding elements with high hydrogen storage abilities has been considered as an important method to improve the resistance of hydrogen embrittlement. Similar method may applied for the development of ferritic alloys as the interconnect materials. Ta has very similar properties as Nb and has been added into steels applied at high temperature. By ion implantation, Nb and Ta may be doped into 430. The effects of Nb and Ta dopants could be compared by dual atmosphere oxidation of the doped 430, which may guide the development of new alloys as the SOFC interconnect.

3) Current work performed the oxidation experiment of the coated samples in lab air. For practical application in SOFC, the coated samples should also be tested in dual

atmosphere oxidation. In dual atmosphere, the oxidation will be aggravated by the diffusion of hydrogen from hydrogen side to air side.

4) For better understanding the hydrogen diffusion in uncoated and MCO coated ferritic alloys, it is necessary to systemically study the diffusivity of hydrogen in coating materials, Cr_2O_3, $(Mn, Cr)_3O_4$, uncoated and coated candidate alloys by hydrogen isotope diffusion test. The hydrogen diffusivity in uncoated ferritic alloy samples with different alloy grain sizes may also be compared. A quantitive relationship between the grain size and hydrogen diffusivity may be achieved, which will further increase our understanding of the effects of alloy grain boundaries.

Reference:

[1] B. C. H. Steele and A. Heinzel, "Materials for fuel-cell technologies," *Nature*, vol. 414, pp. 345-352, 2001.

[2] S. Fontana, R. Amendola, S. Chevalier, P. Piccardo, G. Caboche, M. Viviani, R. Molins, and M. Sennour, "Metallic interconnects for SOFC: Characterisation of corrosion resistance and conductivity evaluation at operating temperature of differently coated alloys," *Journal of Power Sources*, vol. 171, pp. 652-662, 2007.

[3] W. N. Liu, X. Sun, and M. A. Khaleel, "Effect of Creep of Ferritic Interconnect on Long-Term Performance of Solid Oxide Fuel Cell Stacks," *Fuel Cells*, vol. 10, pp. 703-717, 2010.

[4] J. W. Fergus, "Metallic interconnects for solid oxide fuel cells," *Materials Science and Engineering A*, vol. 397, pp. 271-283, 2005.

[5] W. Z. Zhu and S. C. Deevi, "Development of interconnect materials for solid oxide fuel cells," *Materials Science and Engineering: A*, vol. 348, pp. 227-243, 2003.

[6] S. Kaka, A. Pramuanjaroenkij, and X. Y. Zhou, "A review of numerical modeling of solid oxide fuel cells," *International Journal of Hydrogen Energy*, vol. 32, pp. 761-786, 2007.

[7] P. Kofstad, *High temperature corrosion*. London and New York: Elsevier Applied Science, 1988.

[8] W. J. Quadakkers, J. Piron-Abellan, V. Shemet, and L. Singheiser, "Metallic interconnectors for solid oxide fuel cellsa review," *Materials at High Temperatures*, vol. 20, pp. 115-127, 2003.

[9] J. W. Fergus, "Effect of water vapor and hydrogen on the oxidation of metallic interconnect materials for solid oxide fuel cells," in *Solid Oxide Fuel Cells IX*, 2005, p. 1806.

[10] N. Cabrera and N. F. Mott, "Theory of the oxidation of metals," *Reports on Progress in Physics*, vol. 12, p. 163, 1949.

[11] G. Hultquist, B. Tveten, and E. Hörnlund, "Hydrogen in Chromium: Influence on the High-Temperature Oxidation Kinetics in H2O, Oxide-Growth Mechanisms, and Scale Adherence," *Oxidation of Metals*, vol. 54, pp. 1-10, 2000.

[12] M. Monteiro, S. Saunders, and F. Rizzo, "The Effect of Water Vapour on the Oxidation of High Speed Steel, Kinetics and Scale Adhesion," *Oxidation of Metals*, vol. 75, pp. 57-76, 2011.

[13] B. Tveten, G. Hultquist, and D. Walinder, "Hydrogen and Yttria in Chromium: Influence on the High-Temperature Oxidation Kinetics in O2, Oxide-Growth Mechanisms and Scale Adherence," *Oxidation of Metals*, vol. 55, pp. 279-289, 2001.

[14] D. Wallinder, E. Hornlund, and G. Hultquist, "Influence of Hydrogen in Iron and in Two Stainless Steels on Aqueous and Gaseous Corrosion," *Journal of The Electrochemical Society*, vol. 149, pp. B393-B397, 2002.

[15] G. Bamba, Y. Wouters, A. Galerie, G. Borchardt, S. Shimada, O. Heintz, and S. Chevalier, "Inverse growth transport in thermal chromia scales on Fe-15Cr steels in oxygen and in water vapour and its effect on scale adhesion," *Scripta Materialia*, vol. 57, pp. 671-674, 2007.

[16] S. Henry, A. Galerie, Y. Wouters, and L. Antoni, "Abnormal oxidation of stabilized ferritic stainless steels in water vapor," *Materials science forum,* vol. 369-372, pp. 353-360, 2001.
[17] T. Akermark and G. Hultquist, "Oxygen exchange in oxidation of an Fe-20Cr-10Al alloy in ~10 mbar O_2/H_2O-gas mixtures at 920°C," *Oxidation of Metals,* vol. 47, pp. 117-137, 1997.
[18] S. R. J. Saunders, M. Monteiro, and F. Rizzo, "The oxidation behaviour of metals and alloys at high temperatures in atmospheres containing water vapour: A review," *Progress in Materials Science,* vol. 53, pp. 775-837, 2008.
[19] G. Meier, K. Jung, N. Mu, N. Yanar, F. Pettit, J. Pirón Abellán, T. Olszewski, L. Nieto Hierro, W. Quadakkers, and G. Holcomb, "Effect of Alloy Composition and Exposure Conditions on the Selective Oxidation Behavior of Ferritic Fe–Cr and Fe–Cr–X Alloys," *Oxidation of Metals,* vol. 74, pp. 319-340, 2010.
[20] E. Essuman, G. Meier, J. Zurek, M. Hansel, and W. Quadakkers, "The Effect of Water Vapor on Selective Oxidation of Fe-Cr Alloys," *Oxidation of Metals,* vol. 69, pp. 143-162, 2008.
[21] N. K. Othman, J. Zhang, and D. J. Young, "Temperature and water vapour effects on the cyclic oxidation behaviour of Fe-Cr alloys," *Corrosion Science,* vol. 52, pp. 2827-2836, 2010.
[22] K. Przybylski and T. Brylewski, "Interface Reactions between Conductive Ceramic Layers and Fe-Cr Steel Substrates in SOFC Operating Conditions," *Materials Transactions,* vol. 52, pp. 345-351, 2011.
[23] J. Hammer, S. Laney, R. Jackson, K. Coyne, F. Pettit, and G. Meier, "The Oxidation of Ferritic Stainless Steels in Simulated Solid-Oxide Fuel-Cell Atmospheres," *Oxidation of Metals,* vol. 67, pp. 1-38, 2007.
[24] H. Asteman, J. E. Svensson, L. G. Johansson, and M. Norell, "Indication of Chromium Oxide Hydroxide Evaporation During Oxidation of 304L at 873 K in the Presence of 10% Water Vapor," *Oxidation of Metals,* vol. 52, pp. 95-111, 1999.
[25] D. Chatterjee and S. Biswas, "Development of chromium barrier coatings for solid oxide fuel cells," *International Journal of Hydrogen Energy,* vol. 36, pp. 4530-4539, 2011.
[26] H. Asteman, J. E. Svensson, and L. G. Johansson, "Evidence for Chromium Evaporation Influencing the Oxidation of 304L: The Effect of Temperature and Flow Rate," *Oxidation of Metals,* vol. 57, pp. 193-216, 2002.
[27] I. G. Wright and R. B. Dooley, "A review of the oxidation behaviour of structural alloys in steam," *International Materials Reviews,* vol. 55, pp. 129-167, 2010.
[28] J. Robertson, "The mechanism of high temperature aqueous corrosion of stainless steels," *Corrosion Science,* vol. 32, pp. 443-465, 1991.
[29] S. Fontana, S. Chevalier, and G. Caboche, "Metallic interconnects for solid oxide fuel cell: Effect of water vapour on oxidation resistance of differently coated alloys," *Journal of Power Sources,* vol. 193, pp. 136-145, 2009.
[30] F. J. Perez, M. J. Cristobal, M. P. Hierro, and F. Pedraza, "The influence of implanted silicon on the cyclic oxidation behaviour of two different stainless steels," *Surface and Coatings Technology,* vol. 120-121, pp. 442-447, 1999.

[31] M. P. Brady, M. Fayek, J. R. Keiser, H. M. Meyer Iii, K. L. More, L. M. Anovitz, D. J. Wesolowski, and D. R. Cole, "Wet oxidation of stainless steels: New insights into hydrogen ingress," *Corrosion Science,* vol. 53, pp. 1633-1638, 2011.

[32] B. Hua, Y. Kong, W. Zhang, J. Pu, B. Chi, and L. Jian, "The effect of Mn on the oxidation behavior and electrical conductivity of Fe-17Cr alloys in solid oxide fuel cell cathode atmosphere," *Journal of Power Sources,* vol. 196, pp. 7627-7638, 2011.

[33] Y. Liu, "Performance evaluation of several commercial alloys in a reducing environment," *Journal of Power Sources,* vol. 179, pp. 286-291, 2008.

[34] Z. Yang, G. Xia, P. Singh, and J. W. Stevenson, "Effects of water vapor on oxidation behavior of ferritic stainless steels under solid oxide fuel cell interconnect exposure conditions," *Solid State Ionics,* vol. 176, pp. 1495-1503, 2005.

[35] D. Young and B. Pint, "Chromium volatilization rates from Cr_2O_3 scales into flowing gases containing watervapor," *Oxidation of Metals,* vol. 66, pp. 137-153, 2006.

[36] R. Peraldi and B. A. Pint, "Effect of Cr and Ni Contents on the Oxidation Behavior of Ferritic and Austenitic Model Alloys in Air with Water Vapor," *Oxidation of Metals,* vol. 61, pp. 463-483, 2004.

[37] M. Schutze, M. Schorr, D. P. Renusch, A. Donchev, and J. P. T. Vossen, "The role of alloy composition, environment and stresses for the oxidation resistance of modern 9% Cr steels for fossil power stations," *Materials Research,* vol. 7, pp. 111-123, 2004.

[38] A. Galerie, S. Henry, Y. Wouters, M. Mermoux, J. P. Petit, and L. Antoni, "Mechanisms of chromia scale failure during the course of 15-18Cr ferritic stainless steel oxidation in water vapour," *Materials at High Temperatures,* vol. 22, pp. 105-112, 2005.

[39] A. Galerie, Y. Wouters, and M. Caillet, "The kinetic behaviour of metals in water vapour at high temperatures: Can General rules be proposed?" *Materials Science Forum,* vol. 369-372, pp. 231-238, 2001.

[40] A. Galerie, Y. Wouters, M. Pijolat, F. Valdivieso, M. Soustelle, T. Magnin, D. Delafosse, C. Bosch, and B. Bayle, "Mechanisms of Corosion and Oxidation of Metals and Alloys," *Advanced Engineering Materials,* vol. 3, pp. 555-561, 2001.

[41] Z. G. Yang, M. S. Walker, P. Singh, and J. W. Stevenson, "Anomalous corrosion behavior of stainless steel under SOFC interconnect exposure conditions," *Electrochemical and Solid-state Letters,* vol. 6, pp. B35-B37, 2003.

[42] Z. Yang, G.-G. Xia, M. S. Walker, C.-M. Wang, J. W. Stevenson, and P. Singh, "High temperature oxidation/corrosion behavior of metals and alloys under a hydrogen gradient," *International Journal of Hydrogen Energy,* vol. 32, pp. 3770-3777, 2007.

[43] H. Kurokawa, K. Kawamura, and T. Maruyama, "Oxidation behavior of Fe-16Cr alloy interconnect for SOFC under hydrogen potential gradient," *Solid State Ionics,* vol. 168, pp. 13-21, Mar 2004.

[44] N. Shaigan, D. G. Ivey, and W. Chen, "Metal--Oxide Scale Interfacial Imperfections and Performance of Stainless Steels Utilized as Interconnects in

Solid Oxide Fuel Cells," *Journal of The Electrochemical Society*, vol. 156, pp. B765-B770, 2009.

[45] H. S. Seo, G. Jin, J. H. Jun, D.-H. Kim, and K. Y. Kim, "Effect of reactive elements on oxidation behaviour of Fe-22Cr-0.5Mn ferritic stainless steel for a solid oxide fuel cell interconnect," *Journal of Power Sources*, vol. 178, pp. 1-8, 2008.

[46] X. Yu and Y. Sun, "The oxidation improvement of Fe3Al based alloy with cerium addition at temperature above 1000^{o}C," *Materials Science and Engineering A,* vol. 363, pp. 30-39, 2003.

[47] A. Martinez-Villafane, J. G. Chacon-Nava, C. Gaona-Tiburcio, F. Almeraya-Calderon, G. Dominguez-Patino, and J. G. Gonzalez-Rodriguez, "Oxidation performance of a Fe-13Cr alloy with additions of rare earth elements," *Materials Science and Engineering A*, vol. 363, pp. 15-19, 2003.

[48] B. A. Pint, "Experimental observations in support of the dynamic-segregation theory to explain the reactive-element effect," *Oxidation of Metals*, vol. 45, pp. 1-37, 1996.

[49] H. J. Grabke and E. Riecke, "Absorption and diffusion of hydrogen in steels," *Materiali in Tehnologije*, vol. 34, pp. 331-342, 2000.

[50] E. Riecke, B. Johnen, and H. J. Grabke, "Einflüsse von Legierungselementen auf die Korrosion und Wasserstoffaufnahme von Eisen in Schwefelsäure – Teil I: Permeation, Diffusion und Löslichkeit von Wasserstoff in binären Eisenlegierungen," *Materials and Corrosion*, vol. 36, pp. 435-441, 1985.

[51] K. Ono and M. Meshii, "Hydrogen detrapping from grain boundaries and dislocations in high purity iron," *Acta Metallurgica et Materialia*, vol. 40, pp. 1357-1364, 1992.

[52] J. Hirth, "Effects of hydrogen on the properties of iron and steel," *Metallurgical and Materials Transactions A*, vol. 11, pp. 861-890, 1980.

[53] G. Pressouyre and I. Bernstein, "An example of the effect of hydrogen trapping on hydrogen embrittlement," *Metallurgical and Materials Transactions A*, vol. 12, pp. 835-844, 1981.

[54] R. Valentini, A. Solina, S. Matera, and P. De Gregorio, "Influence of titanium and carbon contents on the hydrogen trapping of microalloyed steels," *Metallurgical and Materials Transactions A*, vol. 27, pp. 3773-3780, 1996.

[55] K. Kiuchi and R. B. McLellan, "The solubility and diffusivity of hydrogen in well-annealed and deformed iron," *Acta Metallurgica*, vol. 31, pp. 961-984, 1983.

[56] F. Wei, T. Hara, and K. Tsuzaki, "Precise determination of the activation energy for desorption of hydrogen in two Ti-added steels by a single thermal-desorption spectrum," *Metallurgical and Materials Transactions B,* vol. 35, pp. 587-597, 2004.

[57] F. Wei, T. Hara, and K. Tsuzaki, "Nano-precipitates design with hydrogen trapping trapping character in high strength steels," in *International hydrogen coference* Y. Weng, H. Dong, and Y. Gan, Eds. Grand Teton national park, Wyo.: Springer, 2009, pp. 448-455.

[58] O. R.A, "The diffusion and trapping of hydrogen in steel," *Acta Metallurgica*, vol. 18, pp. 147-157, 1970.

[59] W. Gale and T. Totemeier, "Smithells Metals Reference Book," Eighth Edition ed: Butterworth-Heinemann, 2004, pp. 12-1 -12-25.
[60] H. J. Kestenbach and L. O. Bueno, "Effect of Fe2Nb precipitation on the creep properties of niobium-bearing austenitic stainless steels," *Materials Science and Engineering,* vol. 66, pp. L19-L23, 1984.
[61] Y. Niu, F. Gesmundo, and F. Viani, "The sulfidation of Fe-Nb alloys at 600-800^{o}C under 10^{-8} atm S_2," *Corrosion Science,* vol. 36, pp. 853-869, 1994.
[62] J. C. Ahn, G. M. Sim, and S. L. Kyung, "Effect of Aging Treatment on High Temperature Strength of Nb Added Ferritic Stainless Steels," *Materials Science Forum* vol. 475-479, pp. 191-194, 2005.
[63] K. M. Fujita N and K. Ohmura, "Expressions for solubility products of Fe_3Nb_3C carbide and Fe_2Nb laves phase in niobium alloyed ferritic stainless steels," *ISIJ Int.,* vol. 43, p. 1999, 2003.
[64] Miyazaki A, Takao K, and Furukimi O, "Effect of Nb on the proof strength of ferritic stainless steels at elevated temperatures," *ISIJ Int.,* vol. 42, pp. 916-920, 2002.
[65] Balasubramaniam R, "Alloy development to minimize room temperature hydrogen embrittlement in iron aluminides," *Journal of Alloys and Compounds,* vol. 253-254, pp. 148-151, 1997.
[66] K. Yamamoto, Y. Kimura, F.-G. Wei, and Y. Mishima, "Design of Laves phase strengthened ferritic heat resisting steels in the Fe-Cr-Nb system," *Materials Science and Engineering: A,* vol. 329-331, pp. 249-254, 2002.
[67] Fujita N, Ohmura K., Kikuchi M. , Suzuki T. , Funaki S., and I. Hiroshige, "Effect of Nb on high-temperature properties for ferritic stainless steel," *Scr. Mater.,* vol. 35, p. 705, 1996.
[68] A. Malfliet, F. Verhaeghe, F. Chassagne, J. D. Mithieux, B. Blanpain, and P. Wollants, "Precipitation in Fe-15Cr-1Nb alloys after oxygenation," *Acta Materialia,* vol. 58, pp. 3832-3841, 2010.
[69] A. Błachowski, K. Ruebenbauer, and J. Żukrowski, "Influence of niobium impurity on spin density in metallic iron," *Physica Status Solidi (b),* vol. 242, pp. 3201-3208, 2005.
[70] A. F. Padilha, I. F. Machado, and R. L. Plaut, "Microstructures and mechanical properties of Fe-15% -15% Ni austenitic stainless steels containing different levels of niobium additions submitted to various processing stages," *Journal of Materials Processing Technology,* vol. 170, pp. 89-96, 2005.
[71] S. B. Gesari, M. E. Pronsato, A. Visintin, and A. Juan, "Hydrogen Storage in AB2 Laves Phase (A = Zr, Ti; B = Ni, Mn, Cr, V): Binding Energy and Electronic Structure," *The Journal of Physical Chemistry C,* vol. 114, pp. 16832-16836, 2011/09/29 2011.
[72] M. Bououdina, D. Grant, and G. Walker, "Review on hydrogen absorbing materials-structure, microstructure, and thermodynamic properties," *International Journal of Hydrogen Energy,* vol. 31, pp. 177-182, 2006.
[73] E. Paul and L. Swartzendruber, "The Fe-Nb (Iron-Niobium) system," *Journal of Phase Equilibria,* vol. 7, pp. 248-254, 1986.
[74] J. H. Zhu, C. T. Liu, L. M. Pike, and P. K. Liaw, "Enthalpies of formation of binary Laves phases," *Intermetallics,* vol. 10, pp. 579-595, 2002.

[75] D. Shaltiel, I. Jacob, and D. Davidov, "Hydrogen absorption and desorption properties of AB2 laves-phase pseudobinary compounds," *Journal of the Less Common Metals,* vol. 53, pp. 117-131, 1977.

[76] G. M. Sim, J. C. Ahn, S. C. Hong, K. J. Lee, and K. S. Lee, "Effect of Nb precipitate coarsening on the high temperature strength in Nb containing ferritic stainless steels," *Materials Science and Engineering: A,* vol. 396, pp. 159-165, 2005.

[77] L. Cooper, S. Benhaddad, A. Wood, and D. G. Ivey, "The effect of surface treatment on the oxidation of ferritic stainless steels used for solid oxide fuel cell interconnects," *Journal of Power Sources,* vol. 184, pp. 220-228, 2008.

[78] J. Froitzheim, G. H. Meier, L. Niewolak, P. J. Ennis, H. Hattendorf, L. Singheiser, and W. J. Quadakkers, "Development of high strength ferritic steel for interconnect application in SOFCs," *Journal of Power Sources,* vol. 178, pp. 163-173, 2008.

[79] T. Horita, H. Kishimoto, K. Yamaji, Y. Xiong, N. Sakai, M. E. Brito, and H. Yokokawa, "Effect of grain boundaries on the formation of oxide scale in Fe-Cr alloy for SOFCs," *Solid State Ionics,* vol. 179, pp. 1320-1324, 2008.

[80] T. Horita, H. Kishimoto, K. Yamaji, Y. Xiong, N. Sakai, M. E. Brito, and H. Yokokawa, "Evaluation of Laves-phase forming Fe-Cr alloy for SOFC interconnects in reducing atmosphere," *Journal of Power Sources,* vol. 176, pp. 54-61, 2008.

[81] P. D. Jablonski, C. J. Cowen, and J. S. Sears, "Exploration of alloy 441 chemistry for solid oxide fuel cell interconnect application," *Journal of Power Sources,* vol. In Press, Corrected Proof.

[82] M. P. Sello and W. E. Stumpf, "Laves phase precipitation and its transformation kinetics in the ferritic stainless steel type AISI 441," *Materials Science and Engineering: A,* vol. 528, pp. 1840-1847, 2011.

[83] J. Mougin, M. Dupeux, L. Antoni, and A. Galerie, "Adhesion of thermal oxide scales grown on ferritic stainless steels measured using the inverted blister test," *Materials Science and Engineering A,* vol. 359, pp. 44-51, 2003.

[84] Z. Yang, G.-G. Xia, C.-M. Wang, Z. Nie, J. Templeton, J. W. Stevenson, and P. Singh, "Investigation of iron-chromium-niobium-titanium ferritic stainless steel for solid oxide fuel cell interconnect applications," *Journal of Power Sources,* vol. 183, pp. 660-667, 2008.

[85] X. Sun, W. N. Liu, E. Stephens, and M. A. Khaleel, "Determination of interfacial adhesion strength between oxide scale and substrate for metallic SOFC interconnects," *Journal of Power Sources,* vol. 176, pp. 167-174, 2008.

[86] W. Liu, X. Sun, E. Stephens, and M. Khaleel, "Interfacial Shear Strength of Oxide Scale and SS 441 Substrate," *Metallurgical and Materials Transactions A,* vol. 42, pp. 1222-1228.

[87] A. Srisrual, S. Coindeau, A. Galerie, J. P. Petit, and Y. Wouters, "Identification by photoelectrochemistry of oxide phases grown during the initial stages of thermal oxidation of AISI 441 ferritic stainless steel in air or in water vapour," *Corrosion Science,* vol. 51, pp. 562-568, 2009.

[88] J. Rufner, P. Gannon, P. White, M. Deibert, S. Teintze, R. Smith, and H. Chen, "Oxidation behavior of stainless steel 430 and 441 at 800 ^{o}C in single (air/air) and

dual atmosphere (air/hydrogen) exposures," *International Journal of Hydrogen Energy*, vol. 33, pp. 1392-1398, 2008.

[89] J. Wu, C. D. Johnson, R. S. Gemmen, and X. Liu, "The performance of solid oxide fuel cells with Mn-Co electroplated interconnect as cathode current collector," *Journal of Power Sources*, vol. 189, pp. 1106-1113, 2009.

[90] J. Wu, R. S. Gemmen, A. Manivannan, and X. Liu, "Investigation of Mn/Co coated T441 alloy as SOFC interconnect by on-cell tests," *International Journal of Hydrogen Energy*, vol. 36, pp. 4525-4529, 2011.

[91] K. Komiya, Y. Shinzato, H. Yukawa, M. Morinaga, and I. Yasuda, "Measurement of hydrogen permeability of pure Nb and its alloys by electrochemical method," *Journal of Alloys and Compounds*, vol. 404-406, pp. 257-260, 2005.

[92] G. Matusiewicz and H. K. Birnbaum, "Hydrogen diffusion in Nb-Ta alloys," *Metallurgical and Materials Transactions A*, vol. 13, pp. 1675-1678, 1982.

[93] K. Hashi, K. Ishikawa, T. Matsuda, and K. Aoki, "Hydrogen permeation characteristics of multi-phase Ni---Ti---Nb alloys," *Journal of Alloys and Compounds*, vol. 368, pp. 215-220, 2004.

[94] M. Tanaka, M. Ueda, K. Kawamura, and T. Maruyama, "Hydrogen Permeability through n-type Cr_2O_3 Scale at 1273 K under the Oxygen Activities of 1.6×10^{-18} - 1.0×10^{-16}," *ISIJ International*, vol. 51, pp. 638-644, 2011.

[95] H. Kurokawa, Y. Oyama, K. Kawamura, and T. Maruyama, "Hydrogen Permeation Through Fe-16Cr Alloy Interconnect in Atmosphere Simulating SOFC at 1073 K," *Journal of The Electrochemical Society*, vol. 151, pp. A1264-A1268, 2004.

[96] B. Tveten, G. Hultquist, and T. Norby, "Hydrogen in Chromium: Influence on the High-Temperature Oxidation Kinetics in O2, Oxide-Growth Mechanisms, and Scale Adherence," *Oxidation of Metals*, vol. 51, pp. 221-233, 1999.

[97] Z. Yang, G.-G. Xia, X.-H. Li, and J. W. Stevenson, "(Mn,Co)3O4 spinel coatings on ferritic stainless steels for SOFC interconnect applications," *International Journal of Hydrogen Energy*, vol. 32, pp. 3648-3654, 2007.

[98] P. D. Jablonski and D. E. Alman, "Oxidation resistance of novel ferritic stainless steels alloyed with titanium for SOFC interconnect applications," *Journal of Power Sources*, vol. 180, pp. 433-439, 2008.

[99] B. Hua, J. Pu, F. Lu, J. Zhang, B. Chi, and L. Jian, "Development of a Fe-Cr alloy for interconnect application in intermediate temperature solid oxide fuel cells," *Journal of Power Sources*, vol. 195, pp. 2782-2788, 2010.

[100] A. P. Sutton and R. W. Balluffi, *Interfaces in Crystalline Materials*. New York: Oxford science, 1995.

[101] R. Singh, J. H. Schneibel, S. Divinski, and G. Wilde, "Grain boundary diffusion of Fe in ultrafine-grained nanocluster-strengthened ferritic steel," *Acta Materialia*, vol. 59, pp. 1346-1353, 2011.

[102] Kaur I., Gust W., and Kozma L., *Handbook of grain and interphase boundary diffusion data*. Stuttgart: Ziegler Press, 1989.

[103] A. Bowen and G. Leak, "Solute diffusion in alpha- and gamma-iron," *Metallurgical and Materials Transactions B*, vol. 1, pp. 1695-1700, 1970.

[104] Z. B. Wang, N. R. Tao, W. P. Tong, J. Lu, and K. Lu, "Diffusion of chromium in nanocrystalline iron produced by means of surface mechanical attrition treatment," *Acta Materialia,* vol. 51, pp. 4319-4329, 2003.
[105] X. Ren, K. Sridharan, and T. R. Allen, "Effect of grain refinement on corrosion of ferritic–martensitic steels in supercritical water environment," *Materials and Corrosion,* vol. 61, pp. 748-755, 2010.
[106] V. B. Trindade, U. Krupp, P. E. G. Wagenhuber, and H. J. Christ, "Oxidation mechanisms of Cr-containing steels and Ni-base alloys at high-temperatures –. Part I: The different role of alloy grain boundaries," *Materials and Corrosion,* vol. 56, pp. 785-790, 2005.
[107] K. Hack and T. Jantzen, "Development of databases and generation of stability diagrams pertaining to the modelling of processes during hot corrosion of heat exchanger components," *Materials and Corrosion,* vol. 57, pp. 252-262, 2006.
[108] Y. Mine, K. Tachibana, and Z. Horita, "Grain-boundary diffusion and precipitate trapping of hydrogen in ultrafine-grained austenitic stainless steels processed by high-pressure torsion," *Materials Science and Engineering: A,* vol. 528, pp. 8100-8105.
[109] M. Aucouturier, "Grain boundary segregations and hydrogen embrittlement," *J. Phys. Colloques,* vol. 43, pp. C6-175-C6-186, 1982.
[110] M. Aucouturier, G. Lapasset, and T. Asaoka, "Direct observation of hydrogen entrapment," *Metallography,* vol. 11, pp. 5-21, 1978.
[111] N. Shaigan, W. Qu, D. G. Ivey, and W. Chen, "A review of recent progress in coatings, surface modifications and alloy developments for solid oxide fuel cell ferritic stainless steel interconnects," *Journal of Power Sources,* vol. 195, pp. 1529-1542, 2010.
[112] S. Chevalier, C. Valot, G. Bonnet, J. C. Colson, and J. P. Larpin, "The reactive element effect on thermally grown chromia scale residual stress," *Materials Science and Engineering A,* vol. 343, pp. 257-264, 2003.
[113] W. Qua, J. Lia, and D. G. Iveyb, "Sol-gel coatings to reduce oxide growth in interconnects used for solid oxide fuel cells," *Journal of Power Sources,* vol. 138, pp. 162-173, 2004.
[114] Z. Yang, G.-G. Xia, G. D. Maupin, and J. W. Stevenson, "Evaluation of Perovskite Overlay Coatings on Ferritic Stainless Steels for SOFC Interconnect Applications," *Journal of The Electrochemical Society,* vol. 153, pp. A1852-A1858, 2006.
[115] I. Belogolovsky, X. D. Zhou, H. Kurokawa, P. Y. Hou, S. Visco, and H. U. Anderson, "Effects of Surface-Deposited Nanocrystalline Chromite Thin Films on the Performance of a Ferritic Interconnect Alloy," *Journal of The Electrochemical Society,* vol. 154, pp. B976-B980, 2007.
[116] R. Lacey, A. Pramanick, J. C. Lee, J.-I. Jung, B. Jiang, D. D. Edwards, R. Naum, and S. T. Misture, "Evaluation of Co and perovskite Cr-blocking thin films on SOFC interconnects," *Solid State Ionics,* vol. 181, pp. 1294-1302, 2010.
[117] N. Shaigan, D. G. Ivey, and W. Chen, "Co/LaCrO3 composite coatings for AISI 430 stainless steel solid oxide fuel cell interconnects," *Journal of Power Sources,* vol. 185, pp. 331-337, 2008.

[118] J. Froitzheim, H. Ravash, E. Larsson, L. G. Johansson, and J. E. Svensson, "Investigation of Chromium Volatilization from FeCr Interconnects by a Denuder Technique," *Journal of The Electrochemical Society,* vol. 157, pp. B1295-B1300, 2010.

[119] G. V. Pattarkine, N. Dasgupta, and A. V. Virkar, "Oxygen Transport Resistant and Electrically Conductive Perovskite Coatings for Solid Oxide Fuel Cell Interconnects," *Journal of The Electrochemical Society,* vol. 155, pp. B1036-B1046, 2008.

[120] W. Zhang, J. Pu, B. Chi, and L. Jian, "$NiMn_2O_4$ spinel as an alternative coating material for metallic interconnects of intermediate temperature solid oxide fuel cells," *Journal of Power Sources,* vol. 196, pp. 5591-5594, 2011.

[121] X. Chen, P. Y. Hou, C. P. Jacobson, S. J. Visco, and L. C. De Jonghe, "Protective coating on stainless steel interconnect for SOFCs: oxidation kinetics and electrical properties," *Solid State Ionics,* vol. 176, pp. 425-433, 2005.

[122] Z. Yang, G. Xia, S. P. Simner, and J. W. Stevenson, "Thermal Growth and Performance of Manganese Cobaltite Spinel Protection Layers on Ferritic Stainless Steel SOFC Interconnects," *Journal of The Electrochemical Society,* vol. 152, pp. A1896-A1901, 2005.

[123] P. E. Gannon, V. I. Gorokhovsky, M. C. Deibert, R. J. Smith, A. Kayani, P. T. White, S. Sofie, Z. Yang, D. McCready, S. Visco, C. Jacobson, and H. Kurokawa, "Enabling inexpensive metallic alloys as SOFC interconnects: An investigation into hybrid coating technologies to deposit nanocomposite functional coatings on ferritic stainless steels," *International Journal of Hydrogen Energy,* vol. 32, pp. 3672-3681, 2007.

[124] E. Alvarez, A. Meier, K. S. Weil, and Z. Yang, "Oxidation Kinetics of Manganese Cobaltite Spinel Protection Layers on Sanergy HT for Solid Oxide Fuel Cell Interconnect Applications," *International Journal of Applied Ceramic Technology,* vol. 8, pp. 33-41, 2011.

[125] W. N. Liu, X. Sun, E. Stephens, and M. A. Khaleel, "Life prediction of coated and uncoated metallic interconnect for solid oxide fuel cell applications," *Journal of Power Sources,* vol. 189, pp. 1044-1050, 2009.

[126] T. Horita, H. Kishimoto, K. Yamaji, Y. Xiong, M. E. Brito, H. Yokokawa, Y. Baba, K. Ogasawara, H. Kameda, Y. Matsuzaki, S. Yamashita, N. Yasuda, and T. Uehara, "Diffusion of oxygen in the scales of Fe-Cr alloy interconnects and oxide coating layer for solid oxide fuel cells," *Solid State Ionics,* vol. 179, pp. 2216-2221, 2008.

[127] H. Kurokawa, C. P. Jacobson, L. C. DeJonghe, and S. J. Visco, "Chromium vaporization of bare and of coated iron-chromium alloys at 1073K," *Solid State Ionics,* vol. 178, pp. 287-296, 2007.

[128] Z. Yang, G.-G. Xia, G. D. Maupin, and J. W. Stevenson, "Conductive protection layers on oxidation resistant alloys for SOFC interconnect applications," *Surface and Coatings Technology,* vol. 201, pp. 4476-4483, 2006.

[129] C. Macauley, P. Gannon, M. Deibert, and P. White, "The influence of pre-treatment on the oxidation behavior of Co coated SOFC interconnects," *International Journal of Hydrogen Energy,* vol. 36, pp. 4540-4548, 2011.

[130] Y. Fang, C. Wu, X. Duan, S. Wang, and Y. Chen, "High-temperature oxidation process analysis of MnCo2O4 coating on Fe-21Cr alloy," *International Journal of Hydrogen Energy,* vol. 36, pp. 5611-5616, 2011.
[131] W. Wei, W. Chen, and D. G. Ivey, "Oxidation resistance and electrical properties of anodically electrodeposited Mn-Co oxide coatings for solid oxide fuel cell interconnect applications," *Journal of Power Sources,* vol. 186, pp. 428-434, 2009.
[132] M. J. Lewis and J. H. Zhu, "A Process to Synthesize $(Mn,Co)_3O_4$ Spinel Coatings for Protecting SOFC Interconnect Alloys," *Electrochemical and Solid-State Letters,* vol. 14, pp. B9-B12, 2011.
[133] M. Nakai, K. Nagai, Y. Murata, M. Morinaga, S. Matsuda, and M. Kanno, "Correlation of High-temperature Steam Oxidation with Hydrogen Dissolution in Pure Iron and Ternary High-chromium Ferritic Steel," *ISIJ International,* vol. 45, pp. 1066-1072, 2005.
[134] H. Asteman, J. E. Svensson, M. Norell, and L. G. Johansson, "Influence of Water Vapor and Flow Rate on the High-Temperature Oxidation of 304L; Effect of Chromium Oxide Hydroxide Evaporation," *Oxidation of Metals,* vol. 54, pp. 11-26, 2000.
[135] X. Peng, J. Yan, Y. Zhou, and F. Wang, "Effect of grain refinement on the resistance of 304 stainless steel to breakaway oxidation in wet air," *Acta Materialia,* vol. 53, pp. 5079-5088, 2005.
[136] P. D. Jablonski, C. J. Cowen, and J. S. Sears, "Exploration of alloy 441 chemistry for solid oxide fuel cell interconnect application," *Journal of Power Sources,* vol. 195, pp. 813-820.
[137] K. Nakagawa, Y. Matsunaga, and T. Yanagisawa, "Corrosion behavior of ferritic steels on the air sides of boiler tubes in a steam/air dual enviroment," *Materials at High Temperatures,* vol. 18, pp. 51-56, 2001.
[138] C. Collins, J. Lucas, T. L. Buchanan, M. Kopczyk, A. Kayani, P. E. Gannon, M. C. Deibert, R. J. Smith, D. S. Choi, and V. I. Gorokhovsky, "Chromium volatility of coated and uncoated steel interconnects for SOFCs," *Surface and Coatings Technology,* vol. 201, pp. 4467-4470, 2006.
[139] A. Petric and H. Ling, "Electrical Conductivity and Thermal Expansion of Spinels at Elevated Temperatures," *Journal of the American Ceramic Society,* vol. 90, pp. 1515-1520, 2007.
[140] K. Wang, Y. Liu, and J. W. Fergus, "Interactions Between SOFC Interconnect Coating Materials and Chromia," *Journal of the American Ceramic Society,* vol. 94, pp. 4490-4495, 2011.
[141] A. Navrotsky and O. J. Kleppa, "The thermodynamics of cation distributions in simple spinels," *Journal of Inorganic and Nuclear Chemistry,* vol. 29, pp. 2701-2714, 1967.
[142] A. Purwanto, A. Fajar, H. Mugirahardjo, J. W. Fergus, and K. Wang, "Cation distribution in spinel $(Mn,Co,Cr)_3O_4$ at room temperature," *Journal of Applied Crystallography,* vol. 43, pp. 394-400, 2010.